
Spin-orbit effects in asymmetrically sandwiched ferromagnetic thin films

DISSERTATION

zur Erlangung des akademischen Grades

Doctor rerum naturalium

(Dr. rer. nat.)

vorgelegt

der Fakultät Mathematik und Naturwissenschaften

der Technischen Universität Dresden

von

Dipl.-Phys. Martin Kopte

geboren am 20.12.1986 in Bautzen

Eingereicht am 30. Juni 2017

Die Dissertation wurde in der Zeit von Mai 2012 bis Juni 2017 am Leibniz-Institut für Festkörper und Werkstoffforschung e.V. Dresden und dem Helmholtz-Zentrum Dresden-Rossendorf e.V. angefertigt.

Betreuer: Prof. Dr. rer. nat. J. Faßbender
Prof. Dr. rer. nat. O. G. Schmidt

1. Gutachter: Prof. Dr. rer. nat. J. Faßbender

2. Gutachter: Prof. Dr. ir. H. J. M. Swagten

Abstract

Spin-orbit effects in asymmetrically sandwiched ferromagnetic thin films

Martin Kopte

Dissertation, Technische Universität Dresden

Asymmetrically sandwiched ferromagnetic thin films display a large number of spin-orbit effects, including the Dzyaloshinskii-Moriya interaction (DMI), spin-orbit torques (SOT) and magnetoresistance (MR) effects. Their concurrence promises the implementation of interesting magnetic structures like skyrmions in future memory and logic devices. The complex interplay of various effects originating from the spin-orbit coupling and their dependencies on the microstructural details of the material system mandates a holistic characterization of its properties. In this PhD thesis, a comprehensive study of the spin-orbit effects in a chromium oxide/cobalt/platinum trilayer sample series is presented. The determination of the complete micromagnetic parameter set is based on a developed measurement routine that utilizes quasi-static methods. The unambiguous quantification of all relevant constants is crucial for the modeling of the details of magnetic structures in the system. In this context the necessity of a strict distinction of magnetic objects, that are stabilized by magnetostatics or the DMI, was revealed. Furthermore, a sample layout was developed to allow for the simultaneous quantification of the magnitudes of SOTs and MR effects from nonlinear magnetotransport measurements. In conjunction with a structural characterization, the dominating dependence of the effect magnitudes on microstructural details of the systems is concluded. Precisely characterized systems establish a solid groundwork for further investigations that are needed for viable skyrmion-based devices.

keywords: Dzyaloshinskii-Moriya interaction, skyrmion, micromagnetic parameters, magnetoresistance, spin-orbit torques, magnetotransport

Contents

Abstract	v
Indices	x
1 Introduction	1
2 Fundamentals	5
2.1 Towards new devices	5
2.2 Spin-orbit effects	7
2.2.1 Spin-current sources	8
2.2.2 Magnetoresistance effects	11
2.2.3 Spin-orbit torques	13
2.2.4 Harmonic analysis	16
2.3 Micromagnetic model	18
2.3.1 Dzyaloshinskii-Moriya interaction (DMI)	20
2.3.2 Consequences of the DMI for magnetic structures	21
2.3.3 Interface-induced DMI in asymmetrically stacked ferromagnets	23
2.3.4 Quantification of the interface-induced DMI	27
2.3.5 Levy-Fert three-site model including roughness	28
3 The CrOx/Co/Pt sample system	31
3.1 Experimental techniques	32
3.2 Structural characterization	35
4 Complete micromagnetic characterization	37
4.1 Magnetometry	37
4.1.1 Static investigation	37
4.1.2 Ferromagnetic resonance	40
4.2 DMI quantification	41
4.2.1 Field-driven domain wall creep motion	42
4.2.2 Asymmetric domain growth	43
4.2.3 Winding pair stability	49

4.3	Determination of the exchange parameter	51
4.3.1	Generation of circular magnetic objects	51
4.3.2	Homochiral magnetic bubble domains	55
4.4	Results	56
5	Magnetotransport measurements	59
5.1	Measurement setup	59
5.2	Magnetoresistance effects	60
5.3	Spin-orbit torque quantification	63
5.4	Results	64
6	Discussion	67
6.1	Structural predomination of the DMI strength	67
6.2	Ultra-thin limit exchange parameter reduction	71
6.3	Magnetotransport properties	71
6.4	Magnetic structures in //CrOx/Co/Pt trilayers	74
7	Conclusion and Outlook	75
A	Appendix	79
A.1	Calculation of the skyrmion diameter	79
A.2	Micromagnetic simulation of the winding pair stability	80
	Bibliography	83
	Acknowledgements	97

List of Figures

2.1	Spin-Hall effect	9
2.2	Sketch of spin-orbit torques	13
2.3	Sketch of the asymmetric exchange	19
2.4	Magnetic structures	21
2.5	Phase diagram of DMI induced magnetic structures	22
2.6	Calculated roughness dependence of the DM vector	28
3.1	Depth profiles of asymmetric trilayers from XRR and AES	35
3.2	X-Ray diffractogram of a //CrOx/Co/Pt trilayer	36
4.1	Magnetic field-dependent properties of //CrOx/Co/Pt trilayers	38
4.2	Temperature-dependent magnetic properties of //CrOx/Co/Pt trilayers	39
4.3	Ferromagnetic resonance in //CrOx/Co/Pt trilayers	41
4.4	Domain wall creep motion in //CrOx/Co/Pt trilayers	43
4.5	Asymmetric domain growth in //CrOx/Co/Pt trilayers	45
4.6	Numerical solution for DMI fields	46
4.7	Impact of A on the determination of H_{DM} and D_S	47
4.8	Winding pairs in //CrOx/Co/Pt trilayers	49
4.9	Winding pair stability	50
4.10	Current-induced DW motion and homochiral magnetic circular objects	52
4.11	Diameter scaling of magnetic objects	53
4.12	Magnetic bubble domain stability	55
4.13	Complete set of micromagnetic parameters	57
5.1	Sample layout for simultaneous quantification of MR effects and SOTs	59
5.2	Longitudinal resistances in //CrOx/Co/Pt trilayers	60
5.3	Shunting of AMR and SMR by the platinum layer	61
5.4	Unidirectional spin-Hall magnetoresistance	62
5.5	Spin-orbit torque quantification	63
5.6	Magnetoresistance and spin-orbit torques in //CrOx/Co/Pt trilayers	64
6.1	Structural impact on DMI constants in Pt/Co/metal-oxide trilayers	68
6.2	Comparison of DMI constants in Pt/Co/metal-oxide trilayers	70

List of Tables

2.1	Spin-Hall angle of platinum	10
2.2	Spin-orbit torques in asymmetrically sandwiched ferromagnets	15
2.3	Interface-induced DMI in asymmetrically sandwiched ferromagnets	24
4.1	Winding pair annihilation fields	50
4.2	Magnetic bubble domains in //CrOx/Co/Pt trilayers	56
4.3	Micromagnetic parameters of//CrOx/Co/Pt trilayers	58
5.1	Magnetoresistance and spin-orbit torques in //CrOx/Co/Pt trilayers	65

List of Abbreviations

AD	anti-damping
ADG	asymmetric domain growth
AES	Auger electron spectroscopy
AHE	anomalous Hall effect
AMR	anisotropic magneto-resistance
BLS	Brillouin-light scattering
DMI	Dzyaloshinskii-Moriya interaction
DW	domain wall
EB	exchange bias
FM	ferromagnet(ic)
FL	field-like
FMR	ferro-magnetic resonance
GMR	giant magneto-resistance
HM	heavy metal
LMR	linear magneto-resistance
MO	metal oxide
MPE	magnetic proximity effect
MPMS	magnetic property measurement system
MR	magneto-resistance
PHE	planar Hall effect
PMA	perpendicular magnetic anisotropy
PPMS	physical property measurement system
SEM	scanning electron microscopy
SH	spin-Hall
SHE	spin-Hall effect
SKM	scanning Kerr microscopy
SMR	spin-Hall magneto-resistance
SOC	spin-orbit coupling
SOT	spin-orbit torque
USMR	unidirectional spin-Hall magneto-resistance
XMCD	X-Ray magnetic circular dichroism

XRD	X-Ray diffraction
XRR	X-Ray reflectometry
YIG	yttrium iron garnet
VSM	vibrating sample magnetometry

List of Symbols

A	exchange parameter	J/m
α_{SH}	spin-Hall angle	%
\mathbf{B}	magnetic flux	T
β	critical exponent	
D_{eff}	effective DMI constant	J/m ²
D_{S}	interface-induced DMI constant	J/m
d	diameter	m
Δ	domain wall width	m
δ	pinning potential	J ² /m ³
\mathbf{E}	electric field	V/m
e	electron charge	-1.602×10^{-19} As
γ	gyro-magnetic ratio	(sT) ⁻¹
f	frequency	Hz
f_0	attempt frequency	Hz
ϕ	azimuthal angle	°
$H_{\text{K,c,DM}}$	anisotropy, coercive, Dzyaloshinskii-Moriya field	A/m
\hbar	reduced Planck constant	1.055×10^{-34} Js
j	current density	A/m ²
$K_{\text{eff,D,0}}$	effective, shape, total anisotropy energy	J/m ³
k_{B}	Boltzmann constant	1.38×10^{-23} J/K
k	wave number	m ⁻¹
\mathbf{L}	angular momentum	Js
L_{D}	chiral modulation length	m
l_{coh}	coherence length	m
l_{ex}	exchange length	m
λ_{sd}	spin-diffusion length	m
λ	spin-orbit coupling parameter	J
M_{S}	saturation magnetization	A/m
μ_0	vacuum permeability	$4\pi \times 10^{-7}$ Vs/(Am)
μ	critical creep law exponent	1/4
N_{x}	domain wall demagnetization factor	

R	resistance	Ω
ρ	resistivity	Ωm
\mathbf{S}	spin momentum	Js
σ	domain wall energy	J/m^2
t	layer thickness	m
t	time	s
T_C	Curie temperature	K
T	magnetic torque per unit moment	T
θ	polar angle	$^\circ$
U_c	pinning barrier	J
v	domain wall velocity	m/s
v_0	creep law amplitude	m/s
W	stripe width	m
ω	angular frequency	rad/s
ξ	disorder correlation length	m
χ	resistance ratio	
Z	atomic number	
ζ	creep law exponent	$\text{T}^{1/4}$

To my family

Chapter 1

Introduction

In the last decade, systems of asymmetrically stacked ferromagnetic thin films advanced to a promising technological material platform for novel spintronic devices. The rich physics in the system spans from the interface-induced asymmetric exchange or so called Dzyaloshinskii-Moriya interaction (DMI) over spin-caloric and spin-pumping effects all the way to the current-induced spin-Hall (SHE) and Rashba effect that are responsible for magnetoresistance (MR) effects and spin-orbit torques (SOT). All of these effects have their common origin in the spin-orbit coupling (SOC).

Chiral magnetic structures supported by the DMI, such as skyrmions [1, 2], homochiral magnetic bubble domains [3] or homochiral domain walls (DW) [4], promise to become new fundamental units for logic and memory devices [5–9]. Employing the SOTs allows for a magnetic field-free manipulation of the objects, in terms of the possibility of their generation, switching or motion, while the MR effects offer possible tools for the object detection [10, 11]. These ingredients are required for all-electrical non-volatile field-free devices. The performance of these devices, i.e. their storage density and the operation speed, is determined by the physical nature of the specific type of the chiral object, which in turn imposes stringent requirements on the functional magnetic layer whose properties should be precisely known. For instance, the desired properties of films with isolated free skyrmions as information carriers require that modulated states, like one-dimensional spiral phases and skyrmion lattice states, are suppressed by strong uniaxial anisotropies [12], while a homochiral unfrustrated DMI is preserved. By increasing the DMI, the desired minimization of skyrmions providing large storage densities in skyrmion racetracks can be achieved in magnetic films with typically large anisotropies. In granular films this has to be compromised by the adjustment of the skyrmion size to the characteristic magnetic length scales of the film to provide large mobilities [13].

The current picture of the physical origin of the spin-orbit effects often evolves from empirical consideration. For example, a comparative study [14] only recently suggested the correlation of the widely spreading results of the spin-Hall angles of Pt acquired by different methods over the last years to the Pt resistivity. This finding revealed a strong impact of the

details of the sample preparation on the structural details of nominally identical systems, that is crucial for the interpretation of the spin-Hall results. At the same time the development of an accepted standard quantification method for each effect is still an ongoing process that is complicated by the often simultaneous appearance of different spin-orbit effects.

As the details of the system composition and its microstructure pose a multi-fold impact on the respective effect strengths, a holistic investigation concept is desirable that considers all aspects in one and the same system. So far, this concept is exercised only in a few examples mostly investigating structurally rather complex systems. For instance, in an extensive study of DMI and SOT in X/CoFeB/MgO (X=Hf, W, Ta, TaN), the interface control of magnetic chirality promoted by different heavy metals [15] is attributed to the electro-negativities of the different metals rather than microstructural details. The study of Pt/[Co/Ni]_n/X (X=Pt, Ta, MgO, Cu) [16] revealed that the DMI and SOT not necessarily originate from the same interface. And recent investigations of the DW resistance in Pt/Co/Pt zigzag wires [17] suggests a chiral impact of the DMI on the MR effects. In most parts of the emerging picture, the convolution of spin-orbit effects remains unclear.

In this light the complete characterization of each system is deemed the crucial step before advancing into the interpretation of the interplay of the spin-orbit effects and their application. Therefore, this work aims for a comprehensive characterization of spin-orbit effects for a typical system of a perpendicular magnetized cobalt/platinum bilayer in the hitherto unexplored conjunction to chromium oxide. This metal oxide is introduced to increase the system variety and to gain further insight to its specific role of an insulating metal oxide layer on the spin-orbit effects. The unambiguous quantification of current-driven spin-orbit effects and the statical SOC effect of the DMI are to some extent complementary. While for DMI both interfaces are expected to contribute, the non-conductive interfaces can be neglected for the MR effects and current-induced SOT. On the other hand, there is an enhanced complexity in the investigations of the latter effects due to spin-caloric and Oersted field effects.

In order to properly describe the details of chiral magnetic structures in the system by micromagnetic modeling, the determination of the full micromagnetic parameter set is required, including the saturation magnetization, anisotropy energy constant, exchange parameter and the interface-induced DMI constant. In the thin film limit also the micromagnetic parameters are expected to be predominated by the structural details of the system. By the variation of the thickness of the ferromagnetic cobalt layer, the scaling behavior of all parameters can be assessed. It is stressed that the observed circular magnetic objects have to be classified as they can be identified either as homochiral magnetic bubbles domains or as chiral skyrmions. The bubbles are classical micromagnetic circular domain configurations, where the DMI only selects the sense of rotation in their walls. The skyrmions are proper two-dimensional solitons stabilized by the DMI. They can be distinguished in practice by a different ferromagnetic

layer thickness scaling of their characteristic sizes.

Well-defined chiral magnetic structures are often used as probes for spin-orbit effects. For example, asymmetry features revealed in the field-driven DW motion can be employed for the DMI quantification. Furthermore, the susceptibility of DWs to certain SOT types in different current injection geometries [18] could help to clarify the physical origin of the torque mechanism. Complementarily, the magnetotransport properties are evaluated by employing the harmonic analysis of non-linear resistances induced by the spin-orbit effects.

The thesis is organized as follows. Chapter 2 gives a broad, but brief overview on the fundamentals of spin-orbit effects and their potential for novel spintronic devices. The complexity of the field arises from a large variety of spin-current sources that result in MR effects and SOT when interacting with ferromagnetic layers. For the correct description of chiral magnetic structures in the systems, the DMI term has to be considered in the micromagnetic model. It is attempted to at least give a representative review of the literature results of DMI and SOT magnitudes, which has to be selective though, given the overwhelming amount of publications. The details of the investigated samples system are outlined in Chapter 3 in succession with the results of its structural characterization. Technical experimental details are given along with the presentation of the experimental plan, that was conducted in this work. Chapter 4 describes the developed approach for the full micromagnetic characterization based on elementary magnetometry techniques and Kerr microscopy investigations and presents the results. In Chapter 5 the developed sample layout for the simultaneous quantification of the magnetotransport properties including MR effects and SOTs is introduced and then the results are presented. All results are coherently discussed in Chapter 6 and conclude a dominating dependence of the investigated spin-orbit effect strengths on the micro-structural sample properties. An outlook on further investigations using well-characterized systems is given in conclusion.

Chapter 2

Fundamentals

The chapter is organized as follows. After a review of the ongoing development of logic and memory concepts based on domain walls (DW) and skyrmions in section 2.1. In section 2.2 spin-orbit effects are introduced that are induced by the spin-orbit coupling (SOC) involving charge currents. This incorporates different sources (sec. 2.2.1) for the generation of spin-polarized electrons that are responsible for magnetoresistance (MR) effects (sec. 2.2.2) and spin-orbit torques (SOT) (sec. 2.2.3) upon interaction with localized magnetic moments. As shown in sec. 2.2.4 the harmonic analysis of magnetotransport signals provides an important tool to assess the strength of these effects.

The asymmetric exchange or Dzyaloshinskii-Moriya interaction (DMI) as a static consequence of the SOC is separately presented in sec. 2.3.1 after briefly introducing the classical continuum approach of micromagnetic modeling (sec. 2.3). The impact of this exchange term on chiral magnetic structures is subsequently discussed (sec. 2.3.2). The interface-induced DMI in asymmetrically sandwiched ferromagnetic thin films and its quantification are reviewed in sec. 2.3.3 and 2.3.4 respectively. An attempt to account for the microstructural impact on the DMI by the introduction of roughness in the three-site Levy-Fert model is outlined in sec. 2.3.5.

2.1 Towards new devices

The utilization of the electron spin as the key aspect of the field of spintronics [19] provides additional tools for manipulation of magnetic structures via spin-orbit torques (SOT) [20, 21] and their electrical tracing via magnetoresistance (MR) effects [11]. Potentially omitting external magnetic fields, promising concepts for novel non-volatile logic and memory devices are developed, that rely on these spin-orbit effects [8]. After the field of spintronics was kick-started by the discovery of the giant MR effect [22, 23] in 1988, it was again greatly propelled by proposals of DW logic [24] and DW racetrack memory [6] devices. Along the line of the development from a DW shift register [25] to a commercially available racetrack memory chip in 2011 [26] the exploration of the underlying fundamental topics evolved.

Recently, with the proposal of new concepts such as the skyrmion racetrack device [7, 11, 27] the spintronic field undergoes further advances.

An important feature of the DW racetrack concept is the coherent motion of two DWs enclosing a magnetic domain without impacting their spatial distance. In a field-driven processes this distance would either shrink/grow dependent on un-/favorable field configuration for the enclosed domain resulting in an incoherent motion with zero net-velocity of both DWs. The transfer of spin momentum of spin polarized electron currents in the direction of the electron motion, also known as spin-transfer torque [28], provides sufficient means for such a coherent motion, but requires impractically large current densities. With the discovery of significantly faster DW motion against the electron flow [29–32] the hopes to reach application relevant current densities rose again. At the same time, the complexity of the underlying driving forces for this current-driven DW motion was revealed. Since the last few years the SOTs and their physical origin of is heavily discussed to be either the spin-Hall [33] or the inverse Rashba-Edelstein effect [34, 35]. Both effects generate a spin polarization of identical symmetry that can exert torques on ferromagnetically coupled moments [20]. Phenomenologically, the consensus view consists in describing two types of torques according to their field-like and anti-damping nature. However, the subject is still actively debated as regards the origin or microscopic mechanisms for the torques effects. Despite the unsettled discussion, it was shown that the current-induced effective magnetic fields not only induce DW motion [36, 37] but also support domain nucleation [29] and allow to switch small magnetic elements [38, 39]. In case of the DW motion a strong correlation between the torque efficiency and the details of the DW structure was pointed out. This requires a proper understanding of the details of magnetic structures in general, that are determined by the magnetic materials parameters. In typical magnetic films with high anisotropies, the DWs have widths of the order of few nanometers, which poses severe challenges for microscopic observation techniques that are needed to resolve small modifications of the detailed DW structure, e.g. by the DMIs. A number of successful attempts are reported, pushing the respective experimental techniques to their limits., e.g. by spin-polarized low energy electron microscopy [40], Lorentz transmission electron microscopy [41], nitrogen vacancy microscopy [42] or anisotropic magnetoresistance measurements [43]. The precise knowledge of the magnetic structure of DWs could help to clarify the torque origin via the study of the spin-torque efficiency on different DW types in different current injection geometries [18]. According to Ref. [18] the most efficient case is the spin-Hall effect torque acting on a Néel-wall type. In perpendicularly magnetized thin films the Bloch type DW is expected and the preferable Néel DW has to be induced by additional terms like an external magnetic field [44] or the interface-induced Dzyaloshinskii-Moriya interaction (DMI). The uncovering [40, 45] of the essential aspect of the DMI to cause homochiral DWs, which also enables a coherent DW motion [36, 37], prompted the consolidation of the two fields of spin-Hall effects and the DMI, that were almost separately

developing so far. At that time the DMI was well known to be the underlying cause for the appearance of chiral magnetic textures [2] like helical states and skyrmions in typical chiral magnets [46] or at surfaces [47] leading to their experimental observation [48, 49] at low temperatures. The remarkable innovation therefore was the discovery of a sizable effect of the interface-induced DMI on DWs in familiar ferromagnetic multi-layers at room temperature. The usage of skyrmions as information carriers [7] promises to be superior in many ways to e.g. DW or bubble based devices. The minimum dimensions and topological protection suggest a significant performance enhancement in terms of mobility and stability [21, 50]. Additional possibilities of the individual [51] and collective [52] manipulation of skyrmions are already under investigation. Suitable materials that can host skyrmions are known in bulk form and as ultra thin films. Most of them display magnetic order at low temperatures only, which blocks the straight-forward implementation into applicable devices. This field experiences a new progress with the recently observed *skyrmion bubbles* [3] and objects that are claimed to be skyrmions [53, 54] in comparatively unpretentious systems with sizeable interface-induced DMI at room temperature.

It is stressed that an important aspect for further advances is a clear discrimination between magnetic bubble domains and skyrmions. Already in the 1970s logic and memory devices [55] based on magnetic bubble domains, that share indisputable similarities to the recently discovered objects, were extensively studied and commercialized. The break-through of the bubble memory concept for mass applications is prevented by the low mobility of the magnetic bubble domains, which provides insufficient operation speeds of the devices.

The prospect of viable skyrmion devices relies, besides the careful characterization of skyrmions, on the fundamental understanding of all possible spin-orbit effects in order to properly apply and tune them for dedicated functions. To date the synthesis of the suitable materials with large spin-orbit effects is the central task in this research area. An unambiguous quantification of the magnitude of the chiral magnetic DMI exchange and the impact of SOTs on transport properties remains the crucial step for their characterization.

2.2 Spin-orbit effects

As introduced in the previous section the utilization of the spin degree of freedom in electronic devices has triggered the vastly growing field of spintronics [19]. Novel effects in magnetic structures including non-collinear states, chirality selection or coupling between charge currents and spin textures all are caused by the spin-orbit coupling (SOC). The SOC enables a multitude of physical effects which currently are investigated by a wide range of experimental techniques in magnetism, optics, transport etc. and resulted in countless publications in less than two decades. The overwhelming amount can only be summarized in focused reviews [56–59] usually highlighting a selection of reports. In many areas of this young research

field only recently the results begin to converge to a concise picture. Here, only a brief non-exhaustive overview will be given that is based on a semi-classical understanding tailored to describe phenomena arising in asymmetrically stacked ferromagnetic layers.

The key aspect of spintronics is an interaction of the spin \mathbf{S} and angular \mathbf{L} momentum of electrons described by the SOC with the energy term $\mathcal{H}_{\text{SO}} = \lambda \mathbf{S} \cdot \mathbf{L}$. The SOC parameter λ depends on the electric field \mathbf{E} environment passed by the moving electrons, which therefore is relativistically transformed into a magnetic field

$$\mathbf{B} \propto \mathbf{v} \times \mathbf{E}. \quad (2.1)$$

As the spin polarization direction is a non-conserved quantity, the SOC has consequences for both polarization and depolarization effects of the electron spins. Whereas a low SOC leaves the spin direction almost unaffected, strong SOC leads to a strong spin-dependent scattering, that can result in an efficient separation of spin-polarized electrons. The characteristic length scale, over which the spin-information is kept, also called spin diffusion length λ_{sd} , is otherwise inversely proportional to the SOC. In the chemical elements the SOC parameter is found to roughly follow the Landau-Lifshitz scaling $\lambda(Z) \propto Z^2$ [60]. Light metals like aluminum or copper exhibit a large spin diffusion length of several hundred nanometers, while only a negligibly small spin-Hall effect (SHE) is observed. Contrarily, heavy metals like platinum or tantalum show large SHE with λ_{sd} of only a few nanometers [59]. The motion of charge carriers with spin in the presence of SOC can lead to the accumulation of e.g. spin-polarized electrons.

The sources of electric fields in materials are multifaceted. Spin currents can therefore be driven by electric currents, thermal gradients and magnetization dynamics. At an interface the resulting spin accumulation however will be determined by universal features of the material, independent on the specific driving. As an example it was observed in thin films, that the spin accumulation follows a universal scaling that relies only on the spin-mixing conductance of its surface [61]. The total observed spin accumulation might therefore stem from indistinguishable sources in the first instance.

The interaction of these generated spin-polarized electrons with localized magnetic moments gives then rise to MR effects and SOTs. These effects will be described in the following sections 2.2.2 and 2.2.3 after a short overview of spin current sources (section 2.2.1) is given.

2.2.1 Spin-current sources

The most prominent example of a spin current source is the spin-Hall effect (SHE) [33] describing the direct conversion of charge currents into transverse spin currents. The generation

of spin-polarized electrons is attributed to both extrinsic and intrinsic mechanisms [59]. Already predicted in 1971 [63], the extrinsic version is understood in the Mott or skew scattering picture [62]. Fig. 2.1 illustrates how electrons are scattered into the direction of the preferable field direction dependent on their spin polarization. For isotropically spin-polarized electron currents the scattering results in a separation of opposite spin polarizations in the direction transverse to the current flow. The generation of a *pure* spin current is observed, since during this process no net charge current is induced. Therefore, in finite conductors a homogeneous spin accumulation can be detected at the conductor edges [64] with spins pointing in azimuthal direction around the circumference, as indicated by the colored ring in Fig. 2.1. This heuristic picture holds only in cases of defected materials such as e.g. copper doped with heavy impurities [65]. The rigorous explanation of the complete SHE mechanism beyond the semi-classical picture is based on multi-band microscopic theories [66, 67]. This approach also covers the intrinsic SHE [68] that led to the prediction and observation of the quantum SHE [69]. For many heavy metals the dominating intrinsic contribution accounts for the large spin-Hall conductivities even in homogeneous materials and correctly predicts a sign change between the elements of tantalum and platinum [70].

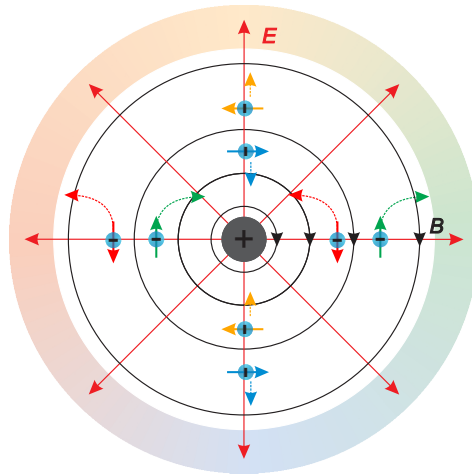


FIGURE 2.1: The separation of spin-polarized electrons by impurity and defect scattering in the extrinsic spin-Hall effect can be understood in the semi-classical concept of Mott scattering [62]. In the reference frame of moving electrons the radial electric field (red) of lattice ions is relativistically transformed into a circular magnetic field (black) of radially decaying strength according to Eq. (2.1). Depending on the relative orientation of the electron's spin polarization with respect to the magnetic field an attraction/deflection towards/from the lattice ion takes place. The resulting separation of electrons with up/down (left/right) spin polarization direction in the horizontal (vertical) axis is sketched and leads to accumulation of spin-polarized electrons at the conductor edges.

TABLE 2.1: Spin-Hall angle α_{SH} and spin diffusion length λ_{sd} of the element platinum measured by different experimental methods at room temperature. The methods utilize approaches of non-local transport (NL), spin-pumping (SP), spin-transfer torque (STT) and spin-Hall magnetoresistance (SMR).

λ_{sd} (nm)	α_{SH} (%)	method	reference
7	0.9	NL	Vila et al. (2011) [71]
7.7 ± 0.7	1.3 ± 0.1	SP	Nakajama et al. (2012) [72]
3.4 ± 0.4	5.6 ± 0.1	SP	Rojas-Sánchez et al. (2014) [73]
1.2 ± 0.1	2.2 ± 0.4	STT+SHE	Kondou (2012) [74]
2.1 ± 0.2	8.5 ± 0.9	STT+SHE	Ganguly (2014) [75]
1.5 ± 0.5	11 ± 8	SMR	Althammer et al. (2013) [76]

The SHE is quantified by the spin-Hall angle α_{SH} determined by the ratio of the spin j_s to charge j_e current density

$$\alpha_{\text{SH}} = \frac{\hbar}{2e} \frac{j_e}{j_s}, \quad (2.2)$$

with the scaling factor containing the reduced Planck constant \hbar and the electron charge e . The desire for an efficient spin-current source has almost triggered an extensive search for spin-Hall materials involving the development of reliable quantification methods for α_{SH} . The details of each approach are beyond the scope of this introduction and can be found in the review of Sinova et al. [59]. An extract of some results for the closely related quantities of the α_{SH} and the spin-diffusion length λ_{sd} for the intensely studied element platinum is given in Tab. 2.1. The wide spread of results exemplifies the current state-of-the-art in the developing field of spin-orbit effects lacking unambiguous quantification methods. Nevertheless, it is safe to state that in platinum the α_{SH} is of the order of a few percent while the λ_{sd} is of the order of a few nanometers. It is important to note, that in the analysis of most methods, α_{SH} and λ_{sd} are physically related quantities. In thin films for layer thicknesses t of the order of λ_{sd} the α_{SH} has been found to have the following dependence [77]

$$\alpha_{\text{SH}}(t) = \alpha_{\text{SH}}^{\infty} [1 - \text{sech}(t/\lambda_{\text{sf}})]. \quad (2.3)$$

The increase towards a constant bulk spin-Hall angle $\alpha_{\text{SH}}^{\infty}$ is attributed to an interference effect of oppositely spin-polarized electrons with in λ_{sd} .

The discrepancies of the results might not necessarily stem from the conceptual differences of the various methods. In a recent study [14] a significant correlation between the resistivity and α_{SH} in Pt films was found, which demands the consideration of strong microstructural influences in the SHE, of which the resistivity is an indirect indicator. Whereas in clean systems with low resistances small spin-Hall angles values are obtained, α_{SH} increases towards moderately dirty systems with larger resistivity. Two regimes are identified, in which the

extrinsic and intrinsic mechanisms of the SHE dominate respectively [14].

A closely related phenomenon accompanying the SHE is the inverse spin-galvanic [78] or Rashba-Edelstein [79] effect, where a spin imbalance occurs in systems with broken inversion symmetry either intrinsically or at the interface of normal metal/ferromagnet bilayers. Both effects have a common microscopic origin [59], which informs an active debate about the origin of e.g. SOTs that has not yet found a clarifying consensus (see section 2.2.3).

The inverse SHE [80] transforming spin currents into charge currents often serves as a detector tool for spin currents, e.g. generated by thermal gradients. Hence, it is of fundamental importance for the field of spin caloritronics [81], in which a quantitative access to thermally induced spin accumulations is required. Since every thermoelectric effect, such as Seebeck-, Peltier- and Nernst effect, has an analogous version for spin-currents the consideration of thermal manipulation has opened an additional extensive research field bearing even broader manipulation possibilities. On the other hand, at the usually applied large current densities in the studies of spin-orbit effects, the generation of thermal gradients in the device structure is inevitable. This demands the careful consideration of the additional spin-caloric contributions in an already complex interplay of effects.

Dynamically excited magnetization precession, i.e. ferromagnetic resonance (FMR), causing spin-pumping in a normal-metal/ferromagnet bilayer represents another spin-current source [82, 83]. This mechanism is at the basis of a further self-contained spintronics field utilizing the magnetization dynamics of magnons and nano-oscillators [84–86].

2.2.2 Magnetoresistance effects

In the following a collection of magnetoresistance effects will be introduced that are predicated to the SOC and expected in sample systems containing normal-metal/ferromagnetic bilayers. The effects are discussed with the unit vector of the magnetization direction defined by spherical coordinates $\hat{\mathbf{m}} = (\sin \theta \cos \phi, \sin \theta \sin \phi, \cos \theta)$ with the polar angle θ measured with respect to the film normal $\hat{\mathbf{z}}$ and the azimuthal angle ϕ with respect to the current direction \mathbf{j} .

In systems containing two ferromagnetic layers with independently orientable magnetization directions the giant magnetoresistance (GMR) [22, 23] is observed. The consequences of the spin-dependent transport are explained by a two current model of electrons with majority and minority spin polarization [19]. It entails distinct resistive device states for the parallel and anti-parallel alignment of the magnetizations in the two ferromagnetic layers that find many technological implementations in digital signal processing. This effect is obtained in perpendicular current injection geometries, whereas the following effects are measured

with in-plane currents. Those are described by a resistivity tensor with longitudinal and transversal components. The individual MR ratios can be disentangled by choosing the proper geometry and are in principle accessible in dc-measurements. Here, lock-in techniques with frequency ω modulated signals are employed that allow for the evaluation of higher harmonics (sec. 2.2.4).

The first harmonic signal of the longitudinal resistance R_ω consists of the sum of the following MR contributions

$$R_\omega^L = R_0^L + \Delta R_\omega^{\text{LMR}} / 1 T B_{\text{ext}} + 1/2 (\Delta R_\omega^{\text{AMR}} + \Delta R_\omega^{\text{SMR}}) \sin^2 \theta + 1/2 (\Delta R_\omega^{\text{AMR}} - \Delta R_\omega^{\text{SMR}}) \sin^2 \theta \cos 2 \phi. \quad (2.4)$$

The anisotropic magnetoresistance (AMR) is the first discovered MR effect displaying the spin dependent transport due to SOC [87]. This effect originates from the sd-scattering of mobile charge carriers at stationary spin-polarized d-shells of magnetic ions with polarization along the magnetization of a ferromagnetic material. It reduces the resistance by the order of a few percent [88] when the current and magnetization direction are perpendicularly aligned. A negative field-dependent linear magnetoresistance (LMR) is ascribed to an elastic scattering process involving thermally excited magnons as revealed by temperature dependent studies [89]. At the interface of normal metal/ferromagnet a phenomenon referred to as spin-Hall magnetoresistance (SMR) [90, 91] occurs. It arises from the interaction of the spin currents generated in the normal metal with the magnetic moments of the adjacent ferromagnetic layer. A resistance change is caused that is dependent on the relative orientation of the localized moments and the polarization of the spin accumulation similar to the GMR effect. Therefore a lower resistance is expected for the collinear alignment of the magnetization and the spin polarization direction generated by the SHE.

The transversal component of R_ω is dominated by the anomalous Hall effect (AHE) that shares a common microscopic origin with the spin-Hall effect introduced in the previous section 2.2.1. Great efforts are attempted to calculate the anomalous Hall resistance from first principles [67]. The symmetry of the AHE is identical to that of the ordinary Hall effect, where moving charges are deflected due to the Lorentz force transversal to both the current direction and the magnetic field. In thin films a transversal charge accumulation proportional to the vector component of the net magnetization pointing perpendicular to both the film plane and the current direction is observed. Since in ferromagnets the currents are spin-polarized, the SOC effect results only in a transversal scattering from the polar magnetic moment components.

The relation of the transversal resistance to the magnetization direction reads

$$R_\omega^T = R_0^T + \Delta R_0^H \cos \theta + 1/2 (\Delta R_\omega^{\text{AMR}} + \Delta R_\omega^{\text{SMR}}) \sin^2 \theta \sin 2 \phi. \quad (2.5)$$

The AHE is therefore widely used as common non-quantitative probe for perpendicular magnetization components in thin films. The developed theoretical framework is not yet at a stage to provide a reliable quantitative relation between magnetization and charge accumulation that would elevate the AHE magnetometry to an outstanding experimental technique.

The third term of Eq. (2.5) is often referred to as planar Hall effect (PHE). Despite the nomenclature this is not an additional effect creating a transversal Hall resistance, but rather originates from the tensor nature of the resistivity [92], hence the AMR and SMR components. Earlier, a combined theoretical and experimental study of CoFeB thin films by Seemann et al. [93] already concluded, that the PHE is entirely driven by the AMR. It became evident with the discovery of large SMR [15] accompanying a large PHE, that the finding of Ref. [93] has to be adopted to systems additionally exhibiting the SMR effect. The recently discovered simultaneous occurrence of AMR and SMR [40, 76, 90] in normal metal/ferromagnetic bilayers has contributed to the clarification of the PHE origin. Nevertheless, the PHE is easily accessible in experiments due to its low offset compared to the AMR and SMR effects.

2.2.3 Spin-orbit torques

Spin-orbit torques (SOT) give rise to the motion of domain walls [36, 37] or the switching of magnetic elements [38, 39] and are therefore a powerful manipulation tool for magnetic states. The relation between the explanations of its physical origin and the quantitative understanding of SOTs has not been achieved to date.

Any spin accumulation created in the vicinity of a ferromagnetic layer, that is allowed to diffuse into it, can exert a torque on the localized magnetic moments of the ferromagnetic layer. In-plane current injections induce two spin accumulation components $\delta\mathbf{m}^\perp \propto \hat{\mathbf{z}} \times \mathbf{j}$ and $\delta\mathbf{m}^\parallel \propto (\hat{\mathbf{z}} \times \mathbf{j}) \times \mathbf{m}$ that are proportional to respective effective magnetic fields \mathbf{B}^\perp and \mathbf{B}^\parallel with the corresponding field-like (FL, \perp) and anti-damping (AD, \parallel) torques $\mathbf{T}^{\perp,\parallel} \propto \mathbf{m} \times \mathbf{B}^{\perp,\parallel}$ [20]. Figure 2.2 illustrates the direction of the effective fields and respective torques for the

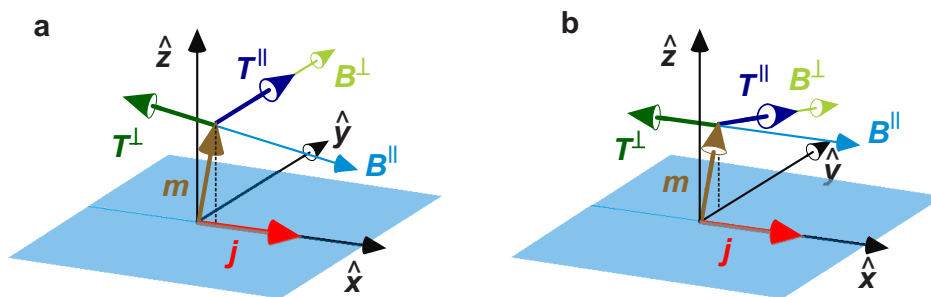


FIGURE 2.2: The sketches represent the direction of field-like (FL) \mathbf{T}^\perp and anti-damping (AD) \mathbf{T}^\parallel spin-orbit torques and the respective effective fields for the magnetization vector slightly deflected from the easy axis of magnetization $\hat{\mathbf{z}}$ towards the direction of (a) $\hat{\mathbf{x}}$ and (b) $\hat{\mathbf{y}}$ by a (not sketched) external magnetic field.

magnetization vector slightly deflected towards the direction of $\hat{\mathbf{x}}$ and $\hat{\mathbf{y}}$. The SOTs are currently classified according to their FL and AD nature, as known from magnetization dynamics described by the Landau-Lifshitz equation [94]. These two components can be quantitatively assessed by a measurement scheme utilizing the harmonic analysis of the anomalous Hall signal [95, 96], which is described in the next section 2.2.4. Currently it is adopted as the most common quantification approach since earlier switching experiments [29] tend to overestimate the magnitude of the torque effect due to possible heat assistance [20, 97].

Typically, systems comprised of //Ta/CoFeB/MgO [15, 20, 39, 95, 98] or //Pt/Co/AlOx [20, 99, 100] complemented by systems with substituted heavy metal layer [15, 101, 102] or symmetrically stacked systems [97, 103, 104] are investigated. Table 2.2 contains a selection of so far reported results. Only a few aspects of the recent findings will be highlighted here, as a more detailed discussion follows together with the results of this work in section 6.

At the moment the inconsistency of state-of-the-art torque quantification methods together with an ambiguous data situation prevents the optimization of the SOT efficiency or achievement of a consensus on their physical origin as already stated by Garello et al. [20] in 2013. The retracing of the determined FL and AD SOT-components to their physical origin remains an unsettled task. The obstacle despite the co-action of spin-current sources [108] proves to be the qualitative equivalence of the torque expressions originating for the different sources of the spin accumulation, e.g. the SHE or Rashba effect [56]. According to semi-classical modeling [109] the relative magnitude of the SOT components hints to either a spin-Hall or Rashba effect origin for a dominating anti-damping ($\mathbf{T}^{\parallel} \gg \mathbf{T}^{\perp}$) or field-like ($\mathbf{T}^{\perp} \gg \mathbf{T}^{\parallel}$) SOT component respectively.

Thickness dependence studies [95, 105] independently altering the NM or FM layer thickness are aimed to discriminate between Rashba and Spin-Hall origin. The AD-SOT component should bear the signature from NM layer thickness scaling of the spin Hall angle [110] according to the Eq. (2.3), while a significant FL component is expected to evolve with the increase of the FM layer thickness. It is evident, that the opposite sign of the spin-Hall angle in the materials Pt and Ta also roughly translates to a sign change of the SOT [39, 99]. In case the anti-damping component of the SOT arises solely from the SHE the following relation allows for the determination of the SH angle [18] from the effective magnetic field B_{AD} of the AD-SOT

$$B_{AD} = \frac{\hbar \alpha_{SH} j_e}{2 |e| M_S t_{FM}}, \quad (2.6)$$

with the saturation magnetization M_S and the thickness t_{FM} of the ferromagnetic layer. Many studies [20, 106] point out a large sensitivity of the SOT components to the interface properties, that are usually altered by annealing processes. For example, two possible mechanisms of Co/Pt inter-diffusion and oxidation at the AlOx enabled by the annealing process are

TABLE 2.2: Collection of spin-orbit torque data reported for asymmetrically sandwiched ferromagnetic thin films in literature so far. The current-normalized field-like T_{FL} and anti-damping T_{AD} torque components of the spin-orbit torques per unit moment are given. The SOTs are quantified via the second harmonic method. The spin-Hall angle α_{SH} is calculated from T_{AD} using eq. 2.6. If stated in the references the saturation magnetization M_S and the anisotropy field H_K are listed, too.

stack	M_S (MA/m)	H_K (MA/m)	T_{FL} $\left(\frac{\text{mT cm}^2}{10^7 \text{A}}\right)$	T_{AD} $\left(\frac{\text{mT cm}^2}{10^7 \text{A}}\right)$	α_{SH} (%)	method	annealing temp. ($^{\circ}\text{C}$), time (h)	ref.
//Pt(3)/Co(0.9)/AlOx(2)	-	-	2	3.5	-	2nd harm.	-	[105]
//Pt(3)/Co(0.6)/AlOx(1.6)	0.80	0.80	-4.0	6.9	16	2nd harm.	as grown 300, 0.5, vac.	[20]
//Ta(3)/CoFeB(0.9)/MgO(2)	-	-	4.5	-2.4	-	2nd harm.	300, vac.	[20]
//Ta(1.5)/CoFeB(1)/MgO(2)	-	-	1.6	4.1	-	2nd harm.	300, 2	[95]
Ta(3)/CoFeB(1)/MgO(2)	0.75	0.06	2.0	4.0	-	2nd harm.	-	[15]
//Ta(3)/CoFeB(0.9)/MgO(2.5)	-	0.06	-2.1	-3.2	-8	2nd harm.	as grown	[106]
	-	0.18	-9.5	-2.0	-6	2nd harm.	288	
Ta(4)/Pt(3)/Co(0.9)/Ta(0.5)	0.78	-	3.5	5.0	9	2nd harm.	-	[103]
Ta(4)/Pt(3)/Co(0.9)/Ta(4)	0.53	-	14.0	20.0	34	2nd harm.	-	
[Pt(2)/Ta(0.15)/Co(0.9)] ₈	-	-	2.0	8.5	-	2nd harm.	-	[104]
[Pt(2)/Co(0.9)] ₈	-	-	2.5	6.0	-	2nd harm.	-	[104]
//GGG/Pt(2.5)/Co(1.1)/Pt(5)	0.5	-	0.6	2.5	-	2nd harm.	-	[107]
Pt(3)/CoNiCo(0.8)/Pt(2)	0.63	0.20	-	2.5	3	2nd harm.	-	[97]
				6.0		switching	-	
W(5.5)/Co ₂ FeAl(0.8)/MgO(1)	0.83	0.24	5	12	30	2nd harm.	-	[101]
Hf(3)/CoFeB(1)/MgO(2)	0.60	0.05	0.8	2.0	-	2nd harm.	-	[15]
TaN(3)/CoFeB(1)/MgO(2)	1.20	0.40	2.4	5.8	-	2nd harm.	-	

discussed to lead to a reduction of the SOTs in Pt/Co/AlO_x. The spread of reported SOT amplitudes in the structurally more complex Ta/CoFeB/MgO systems also is attributed to influences on the SOT arising from variations in the structurally more complex system due to composition, Boron migration to the interface, etc.

Furthermore, angular dependence studies [20, 106] revealed a complex SOT vector dependence on the magnetization direction, that is not covered by standard SOT models based on the Rashba effect and SHE. E.g. in Ta/CoFeB/MgO both SOT components are strongly anisotropic and yield maximum amplitudes for in-plane magnetized ferromagnetic layers. This discovery requires the extension of the theoretical framework by a calculation based on a realistic description of the electronic structure [20].

2.2.4 Harmonic analysis

As a tool to assess current-induced effective magnetic fields an originally developed method by Pi et al. [111] evaluating second harmonic signals has been established [20, 95, 96] a few years ago and is now widely used. A modulated current $I = I_0 \sin(\omega t)$ at a moderate frequency ω induces small oscillations of the magnetization around its equilibrium direction determined by micromagnetic and experimental details and causes resistance contributions that vary quadratically with the applied voltage. Ohm's law for a weakly current-dependent resistance reads

$$V(I, t) = I_0 R(0) \sin(\omega t) + \frac{I_0^2}{2} \frac{dR}{dI} \sin(2\omega t) \quad (2.7)$$

with the second harmonic signal $R_{2\omega} = I_0/2 dR/dI$. In general, the longitudinal and transversal second harmonic signals contain several contributions [112] from the respective spin current sources (section 2.2.1) and MR effects

$$R_{2\omega}^L \propto I_0 \left(R_{2\omega}^{\text{SOT}} + R_{2\omega}^{\nabla T} + R_{2\omega}^{\text{USMR}} \right) \quad (2.8a)$$

$$R_{2\omega}^T \propto I_0 \left(R_{2\omega}^{\text{T,SOT}} + R_{2\omega}^{\text{T},\nabla T} + R_{2\omega}^{\text{T,USMR}} \right). \quad (2.8b)$$

In general, the resistance changes due to the SOTs or thermal gradients (∇T) and the unidirectional SMR (described below) contribute to both the longitudinal and the transversal second harmonic signals.

Effective magnetic fields generated according to their symmetry alter the nonlinear resistance. Measurements of $R_{2\omega}^T$ in different orientations of the external magnetic field with respect to the current (here applied in along the \hat{x} axis) allows to access the parallel and transversal component of the effective field ($B_{\text{eff}}^{\parallel,\perp}$) from the ratio of the derivatives of the first and second

harmonic of the transversal resistance

$$\Delta B_{x(y)} = \left(\frac{\partial R_{2\omega}^H}{\partial B} \right) \bigg/ \left(\frac{\partial^2 R_{\omega}^H}{\partial B^2} \right) \bigg|_{B_{\text{ext}}=B_{x(y)}} \quad (2.9a)$$

$$B_{\text{eff}}^{\parallel(\perp)} = -2 \frac{\Delta B_{X(Y)} \pm 2 \chi \Delta B_{Y(X)}}{1 - 4 \chi^2}, \quad (2.9b)$$

with $\chi = \Delta R^{\text{PHE}}/\Delta R^{\text{AHE}}$ giving the ratio of the PHE contribution, i.e. $\Delta R^{\text{PHE}} = 1/2 (\Delta R_{\omega}^{\text{AMR}} + \Delta R_{\omega}^{\text{SMR}})$ in the transversal resistances signal. The \pm sign corresponds to the magnetization direction along $\pm \hat{z}$. In cases, where the PHE contribution is negligible (e.g. in suitable measurement configuration with $\phi = 0$ or 90°) the field-like (FL) $B_{\text{eff}}^{\parallel}$ and anti-damping (AD) B_{eff}^{\perp} effective SOT fields are equivalent to $-2 \Delta B_{x(y)}$. This expression holds for small deviations of magnetization direction from the easy axis (i.e. $\Delta \theta \ll 1$). The full derivation by Kim et al. can be found in Ref. [95] and was extended by Hayashi et al. [96] to include the PHE.

It is stressed, that the USMR contributes to the transversal second harmonic signal via the PHE as well. So far, this aspect has not been accounted for in the deductions. In this work, the various effect superpositions arising from the PHE are therefore avoided by the choice of the measurement geometry.

The evaluation of both effective fields in terms of their origin still has to consider additional contributions, Eq. (2.8). The Oersted-field contributes to B_{eff}^{\perp} while the anomalous Nernst effect (ANE) is known to contribute to the $B_{\text{eff}}^{\parallel}$ [106]. The Oersted field can be estimated by $B_{\text{Oe}} = \mu_0 I/(2W)$ including the stripe width W [20]. Dependent on the details of the thermal properties of the layer stacking the Joule heating may generate a thermal gradient along the film normal that is responsible for the ANE. A discrimination scheme of the second harmonic thermal and SOT contributions is proposed by Avci et al. [106] via their field dependencies ($R_{2\omega}^{\text{FL}} \propto B_{\text{ext}}^{-1}$, $R_{2\omega}^{\text{AD}} \propto (B_{\text{ext}} + B_{\text{dem}} - B_{\text{ani}})^{-1}$ and $R_{2\omega}^{\text{VT}} \propto \text{constant}$). The ANE contribution was found to be in-/significant in Pt/Co and Ta/Co and layers respectively. It should be noted that any difference in the layer properties or stacking requires a reevaluation of this aspect, since the thermodynamics of the system is changed.

The disentanglement of contributions to the longitudinal second harmonic resistance $R_{2\omega}^{\text{L}}$, Eq. (2.8a) firstly requires the careful evaluation of the transversal second harmonic resistance. A unidirectional spin-Hall magnetoresistance (USMR) was thereby revealed in a recent study [112]. In their interpretation, this effect is explained similar to the GMR effect with currents perpendicular to a layer stack. A spin polarized layer is generated by the SHE at the interface of a ferromagnet/normal metal bilayer and acts like a fixed layer in the classical GMR setup. The localized moments of the ferromagnet represent the free layer that is controlled by the external magnetic field. The electrons traveling through this configuration experience a resistance that depends on the relative orientation of these layers. This results in a high/low

resistance for their anti-/parallel alignment, similar to the GMR.

The current and layer thickness dependent features of the SHE are expected to transfer to the USMR as the spin polarization is generated by the SHE. The increase of either the charge current density or the normal metal layer thickness will increase the amount of spin polarized electrons accumulating at the interface.

2.3 Micromagnetic model

The state of a magnetic material is determined by the minimization of the phenomenological micromagnetic energy

$$\mathcal{E} = \mathcal{E}_A + \mathcal{E}_K + \mathcal{E}_{MS} + \mathcal{E}_Z + \mathcal{E}_{DM} \quad (2.10)$$

with the exchange, anisotropy, magneto-static, Zeemann- and Dzyaloshinskii-Moriya term respectively. In the here discussed perpendicular magnetized systems with the energy takes the following form

$$\mathcal{E} = A (\nabla \hat{\mathbf{m}})^2 + K_{\text{eff}} (\hat{m}_z)^2 + M_S \hat{\mathbf{m}} \cdot \mathbf{B} - D [m_z \text{div} \hat{\mathbf{m}} - (\hat{\mathbf{m}} \nabla) m_z] \quad (2.11)$$

with the parameter set including the exchange stiffness parameter A , the effective uniaxial anisotropy energy K_{eff} , the saturation magnetization M_S and the DMI constant D describing the intrinsic magnetic material properties. The saturation magnetization M_S accounts for the susceptibility of the system to external fields and the strength of the magneto-static stray fields. The exchange parameter scales the strengths of the ferromagnetic exchange by favoring the parallel alignment of localized magnetic moments and is proportional to the Curie temperature ($A \propto T_C$) [113]. The magnetic anisotropies arising from high crystalline symmetry are disregarded in ultra-thin polycrystalline films. The interface-induced uniaxial anisotropy K_0 favors the alignment of moments parallel to the film normal. Due to the principle of stray-field minimization, a magnetization dependent shape anisotropy K_D suppressing K_0 leads to an effective anisotropy K_{eff} of the system, Eq. (2.12).

$$K_{\text{eff}} = \mu_0 M_S H_K / 2 \quad (\text{effective}) \quad (2.12a)$$

$$K_D = \mu_0 M_S^2 / 2 \quad (\text{shape}) \quad (2.12b)$$

$$K_0 = \mu_0 M_S (M_S + H_K) / 2 \quad (\text{total}) \quad (2.12c)$$

Disregarding the DMI term, many aspects of magnetic configurations regarding e.g. domains and domains walls are described in the classical continuum approach of micromagnetic modeling. As the effects of the DMI are usually suppressed by large anisotropies it was often considered to be negligible and only recently became apparent in ultra-thin films with large SOC [40, 48, 49]. Excluding the DMI term DW specific quantities are deduced as can be found

in the relevant literature [114]. Domain walls (DW) separating oppositely magnetized areas are mainly classified into Bloch and Neél type walls (Fig. 2.4) in perpendicular magnetized systems. The moments defining the wall are pointing either perpendicular (B) or parallel (N) to the normal of the DW plane. The DW energy of each DW type is proportional to the product of the exchange parameter to the respective anisotropy energy

$$\sigma_B = 4\sqrt{AK_{\text{eff}}}, \quad \sigma_N = 4\sqrt{AK_D}. \quad (2.13)$$

Depending on the generation of either surface or volume magnetic charges by the given magnetic inhomogeneity of the DW the effective or the shape anisotropy energy, Eq. (2.12), are taken into account. Furthermore, the characteristic width of the Bloch wall can be calculated

$$\Delta = \pi\sqrt{\frac{A}{K_{\text{eff}}}}. \quad (2.14)$$

The exact profile of Neél walls remains difficult to determine. They exhibit a core with a width of the order of the exchange length $l_{\text{ex}} = \sqrt{A/K_D}$ and usually the long tails. Those tails can cause strong interaction between individual walls, that for example can lead to the formation of winding pairs [114].

Isolated magnetic bubble domains are described in the framework of bubble domain theory [115] deducing the stability criteria from the ratio of the DW and magneto-static energy of the bubble (see sec. 4.3.2).

It is emphasized that in the presence of DMI the DW energy is reduced [4], which was not considered in the original works. The consequences of the chiral exchange for magnetic structures are discussed in sec. 2.3.2 after a general introduction of the Dzyaloshinskii-Moriya interaction (DMI) in sec. 2.3.1.

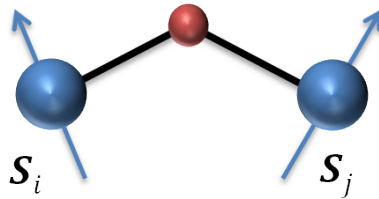


FIGURE 2.3: Sketch of the asymmetric exchange between two neighboring spins S_i and S_j asymmetrically linked by a exchange-mediating atom.

2.3.1 Dzyaloshinskii-Moriya interaction (DMI)

The Dzyaloshinskii-Moriya interaction (DMI) was originally proposed to explain weak ferromagnetic behavior observed in anti-ferromagnets like ferric oxide. In materials with broken inversion symmetry on the level of the unit cell, an asymmetric exchange term between neighboring spins $\mathbf{S}_i, \mathbf{S}_j$ additionally arises, that adds to the (anti-)parallel exchange or Heisenberg term of (anti-)ferromagnets [116]. This so-called DMI favors spin canting with a certain symmetry according to the energy term

$$\mathcal{H}_{\text{DM}} = \mathbf{D}_{i,j} \cdot (\mathbf{S}_i \times \mathbf{S}_j), \quad |\mathbf{D}| \propto \lambda \quad (2.15)$$

with the Dzyaloshinskii-vector $\mathbf{D}_{i,j}$ proportional to the SOC parameter λ [117–119]. The DMI can be understood as a perpetuated super-exchange between two spins via the intermediate atom as sketched in Fig. 2.3. Due to the asymmetric position of the ligand the exchange-mediating electrons experience an effective magnetic field, Eq. (2.1), from the crystal electric field. The spin of the hopping electron has to adjust accordingly because of the SOC [120] (see section 2.2).

A similar effect is observed at interfaces [47], where the inversion symmetry of the system is locally broken by lattice mismatch-induced strain or chemical gradients etc. Similarly strong local symmetry breaking inherent in step edges locally induces DMI-like terms [121–124]. In simple terms any symmetry breaking can be translated to a pseudo-electric field for the SOC.

The asymmetric exchange in systems exhibiting a broken symmetry at the $\hat{\mathbf{z}}$ -interface and that are isotropic in the plane are described [4] by a Dzyaloshinskii-vector $D \hat{\mathbf{z}} \times \mathbf{u}$ for any in-plane direction \mathbf{u} with the corresponding energy term in the micromagnetic continuum formulation

$$\mathcal{E}_{\text{DM}} = D [m_z \text{div } \hat{\mathbf{m}} - (\hat{\mathbf{m}} \nabla) m_z]. \quad (2.16)$$

It can be shown [4] that the consequences of this energy term for e.g. domain walls are equivalent to an effective in-plane magnetic field

$$\mu_0 H_{\text{DM}} = D / (M_S \Delta) \quad (2.17)$$

with the DW parameter $\Delta = \sqrt{A/K_{\text{eff}}}$. In the nature of an interface effect, D is expected to inversely scale with the ferromagnetic layer thickness t_{FM} . Hence only an effective DMI strength of $D_{\text{eff}} = D/t_{\text{FM}}$ can be experimentally observed [125, 126].

2.3.2 Consequences of the DMI for magnetic structures

In perpendicularly magnetized extended films the DWs are expected to be of Bloch-type because of a lower wall energy. The DMI reduces the DW energy by πD [4] until eventually the Néel wall becomes energetically favorable. Furthermore, the DMI lifts the degeneracy for different DW chiralities (Fig. 2.4), i.e. the DW chirality is set by the sign of D -vector. Dependent on the direction of the DM vector one DW chirality is favored over the other. This was experimentally verified by Chen et al. [40, 45], who measured the magnetization components of DWs in Cu/Ni/Fe systems by spin-polarized low-energy electron microscopy (SPLEEM). For large Ni thicknesses Bloch walls were observed which turn into homochiral Néel walls in case the Ni layer became sufficiently thin, i.e. the effective DMI became large enough. Upon stack order inversion the chirality of DW inverted as expected. In an other work either Bloch or left-chiral Neel walls were observed by nitrogen vacancy microscopy in Ta/CoFeB(1nm)/MgO and Pt/Co(0.6nm)/AlO_x respectively [42]. The DW type difference is caused by the far larger effective DMI of the latter system.

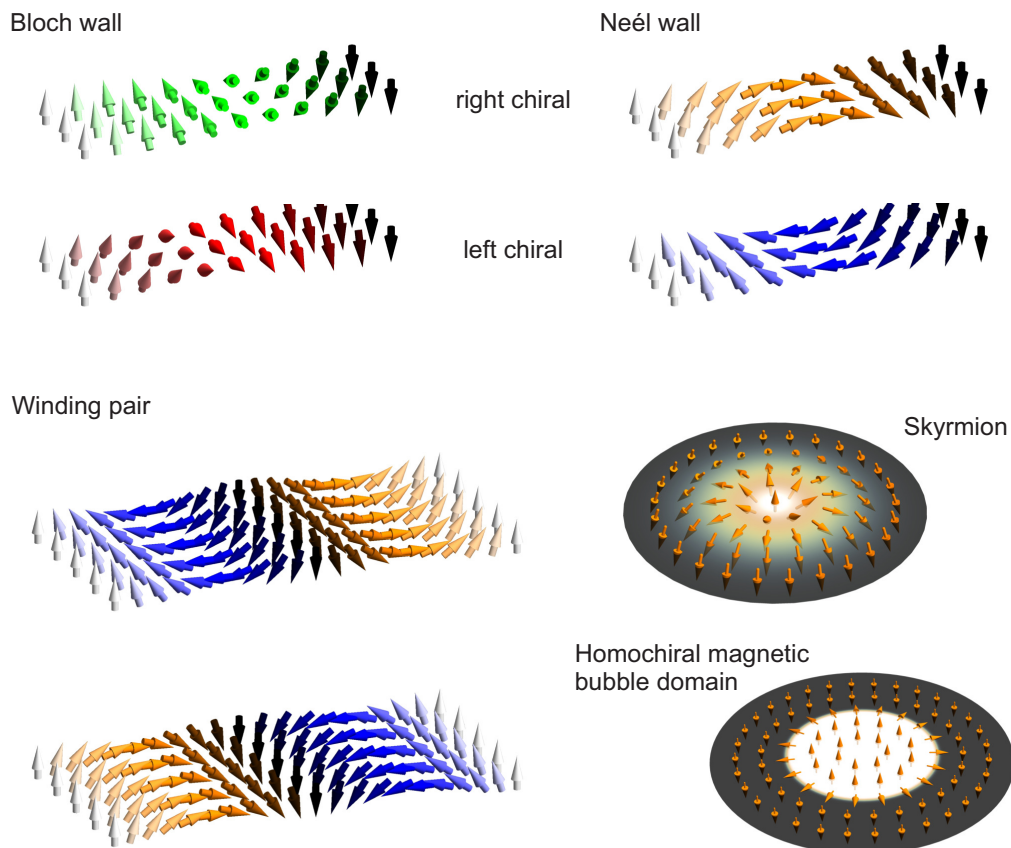


FIGURE 2.4: Sketches of different magnetic structures including DWs of different type and chirality, winding pairs, skyrmions and homochiral magnetic bubble domains.

In chiral bulk systems with B20-structure etc. [46] or at interfaces [47], the DMI is responsible for chiral magnetic states, such as the experimentally observed helical [48] and skyrmion [49] lattices. The characteristic scale of these lattices is of the order the chiral modulation length

$$L_D \propto A/|D_{\text{eff}}| \quad (2.18)$$

determined by the ratio of the ferromagnetic and chiral exchange parameter [46]. Fig. 2.5 shows a phase diagram adopted from Ref. [127] that reveals the stable regions for the respective lattice states depending on the reduced anisotropy $k = K/(D^2/4A)$ and the reduced field $h = H/(D^2/4AM)$ obtained from thermodynamical considerations [12, 46, 127]. Accordingly, skyrmion lattices are formed only for systems with a DMI constant exceeding the critical DMI value [46] of

$$D_c = 4\sqrt{AK_{\text{eff}}}/\pi. \quad (2.19)$$

However, isolated skyrmions (Fig. 2.4) can exist in the saturated state of ferromagnets. Some characteristic properties of skyrmions were investigated e.g. in Ref. [128, 129] and their successful writing and deleting has been demonstrated [51].

A magnetic skyrmion is defined as radial symmetric object with a rigid cross-sectional profile obtaining a continuous rotation of the magnetic moments. Skyrmions are two-dimensional solitons acting as localized elastic particles [2, 130]. In contrast, magnetic bubble domains are characterized by a homogeneously magnetized core that is confined by a DW, which can

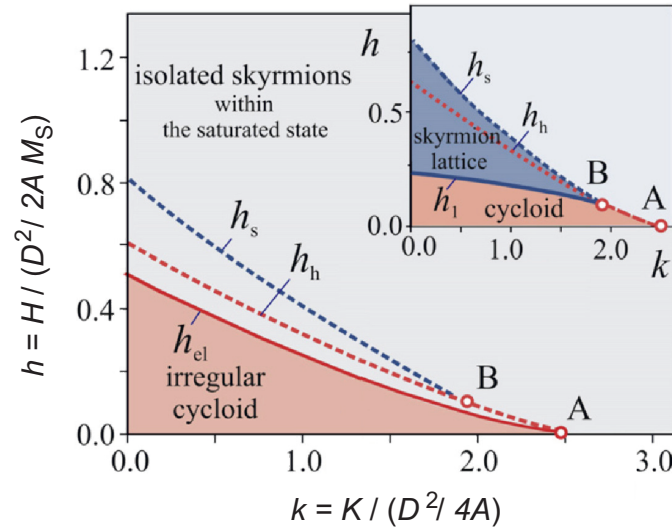


FIGURE 2.5: Phase diagram of DMI induced magnetic structures adopted from Ref. [127]. While isolated skyrmions can exist also in the saturated state the stable phases of helical and skyrmion lattices are given by the reduced field h and anisotropy k of the system that are determined by all intrinsic magnetic parameters.

be assumed to be homochiral in systems with DMI. The state of a magnetic bubble is well defined by the competition of the magneto-static, DW and Zeemann energy terms allowing for a deterministic prediction of the bubble size [114].

Homochiral magnetic bubble domains (Fig. 2.4) are in many ways similar to skyrmions e.g. obtaining the same topological charge number. Both objects are still fundamentally different with distinct properties in terms of dynamics, stability and susceptibility to pinning [7]. Magnetic bubble domain obtain a rather fragile radial symmetry. In case of part of the confining DW is pinned, elongated domains can be formed [3]. These bubble domains have been subject of an intense study in the 1970s driven by idea for a novel non-volatile memory concept devoid of physically moving parts [131]. Due to the low mobility of the bubbles, the devices [55] could not be established as mass products.

With essentially homochiral DWs in systems with DMI, the formation of so-called winding pairs [114] (Fig. 2.4) is likely to be observed by the close coupling of two DWs [41, 132]. A similar distinction as for skyrmions and bubble domains is required for the so called DMI kinks that form the base unit of the helical lattices. As in the case of skyrmions, their profile exhibits a continuous 360° rotation with a width of the chiral modulation length. An isolated homochiral Néel wall pair might not be strictly equal to a DMI kink since it might be separated by a homogeneously magnetized area.

The stabilization mechanism of the objects by either the DMI or magneto-statics is not yet fully clarified which entails the principle question of a possible transmutation between homochiral bubbles and skyrmions or winding pairs and DMI kinks.

2.3.3 Interface-induced DMI in asymmetrically stacked ferromagnets

Large bulk or interface-induced DMIs are found in e.g. $\text{Fe}_{0.5}\text{Co}_{0.5}\text{Si}$ [49] and Fe monolayers on Ir [133] respectively. The study of magnetic textures in these materials by spin-polarized scanning tunneling microscopy or Lorentz transmission electron microscopy involves demanding experimental conditions of ultra-high vacuum and low temperatures. A more feasible material class comprised of asymmetrically sandwiched ferromagnetic thin films was uncovered by the observation of film growth-dependent DW types and chiralities in Fe/Ni multilayers measured by SPLEEM [40]. The study concluded the interface-induced DMI [47] as underlying mechanism for the chirality selection. A large interest in these type of systems [125, 126, 134–139] was triggered, which just recently culminated in reports of the observation of room-temperature skyrmions [3, 53, 54].

In the following, previous results obtained in asymmetrically sandwiched ferromagnets will be outlined. Taking for example the intensely studied platinum/cobalt interface, the

TABLE 2.3: Interface-induced DMI constants D_s of ferromagnetic thin films either sandwiched in between two heavy metals (HM) or a metal oxide (MO) and a HM quantified by the methods evaluation the asymmetric magnon dispersion (BLS), the asymmetric domain growth (ADG) or the winding pair stability (WPA) (see text). The other micromagnetic parameters including the saturation magnetization M_s , anisotropy field H_K and exchange parameter A are given if specified in the references.

stack	M_s (MA/m)	H_K (MA/m)	D_s (pJ/m)	A (pJ/m)	method	annealing	ref.
HM/FM/MO							
//Ta(4)/Pt(4)/Co(t)/AlOx(2)	1.42	-	2.18 ± 0	-	BLS		[138]
//Ta(3)/Pt(3)/Co(t)/MgO	1.40	-	2.17 ± 0.14	27.5	BLS	1.5h, 250°C, vac.	[53]
//Ta(3)/Pt(3)/Co(0.6)/AlOx(2)	1.36	0.79	1.88 ± 0.21	-	BLS		[125]
//Ta(3)/Pt(3)/Co(0.8)/AlOx(2)	1.18	0.67	1.75 ± 0.20	-	BLS		[125]
//Ta(3)/Pt(3)/Co(0.9)/AlOx(2)	1.20	0.57	1.69 ± 0.07	-	BLS		[125]
//Ta(3)/Pt(3)/Co(0.95)/AlOx(2)	1.34	0.35	1.67 ± 0.23	-	BLS		[125]
//Ta(3)/Pt(3)/Co(1.2)/AlOx(2)	1.10	0.08	1.63 ± 0.10	-	BLS		[125]
//Pt(5)/Co(1)/GdOx(t)	1.20	0.56	1.60 ± 0.20	16	BLS + ADG	35s O ₂ -plasma	[139]
//Pt(4)/Co(t)/AlOx(2)	1.10	-	1.37 ± 0	-	BLS		[126]
//Ta(3.2)/Pt(3)/Co(0.8)/AlOx(3)	1.10	0.13	0.26 ± 0.04	16	WPA		[41]
//Pt(2)/CoFeB(0.8)/MgO(2)	1.60	0.19	0.80 ± 0.08	-	BLS	1h, 240°C, vac.	[140]
//Pt(4)/CoFeB(t)/AlOx(2)	0.95	-	0.70 ± 0	-	BLS		[126]
//TaN(1)/CoFeB(1)/MgO(2)	1.24	-	0.31 ± 0.06	-	BLS	1h, 300°C, vac.	[141]
//W(3)/CoFeB(1)/MgO(2)	0.79	-	0.27 ± 0.04	-	BLS	1h, 300°C, vac.	[141]
//Hf(1)/CoFeB(1)/MgO(2)	0.97	-	0.15 ± 0.04	-	BLS	1h, 300°C, vac.	[141]
HM/FM/HM							
//Pt5/Co0.9/Ir6.9/Pt3	1.33	-	1.18 ± 0.09	-	ADG		[135]
//[Pt/Co/Ta] ₁₅	0.60	-	1.17 ± 0.18	-			[54]
//Pt4/Co1.6/Ni1.6	1.16	-	0.70 ± 0.01	-	BLS		[137]
//Pt5/Co0.9/Ir4.6/Pt3	0.94	-	0.45 ± 0	-	ADG		[135]
//Pt5/Co0.9/Ir2.3/Pt3	0.81	-	-0.05 ± 0	-	ADG		[135]
//Ta(2)/Pt(2nm)/Co(0.4)/Py(5)/MgO(5)	1.03	0.48	0.89 ± 0.16	-	SKM		[142]

DM-vector of a certain magnitude points into the direction of the interface normal \hat{z} . By capping this bilayer with another Pt layer an identical interface with inverted axis of the symmetry breaking is created. Therefore, two equally large, but opposite DM vectors result in the full compensation of the effective interface-induced DMI in the system. This general aspect was experimentally verified on an epitaxially grown Pt/Co/Pt trilayer [135]. The same study showed that the full compensation can be compromised by adding iridium to one of the interface regions. The effective DMI scales with the amount of Ir and even reverses its sign. For the qualitative explanation of this behavior it is important to know that the element Ir also obtains an opposite sign of the SOC with respect to Pt causing a opposite DM vector direction. Furthermore, the dependence of the DMI strength on the thickness of Pt grown in identical conditions was shown [143]. A steep increase starting at zero is found below a Pt thickness of 2 nm reaching an almost constant level at larger thickness. The increase before the percolation threshold of the Pt film has to be interpreted as a coverage effect reducing the DMI strength by a geometrical ratio of Pt-covered area vs. the total film area. Therefore, in Pt/Co/Ir/Pt systems the total DM vector of the top interface is a sum of a component of Ir covered areas pointing parallel to the DM vector of the bottom interface and a compensating anti-parallel component originating from Pt covered areas. Hence, the maximum of the effective DMI in Pt/Co/Ir trilayers is expected for fully Ir covered interfaces. Thereby, a system can be conditioned, in which the critical DMI value, Eq. (2.19), also determined by its usually large anisotropy, can potentially be exceeded due to a sufficiently large DMI to allow for the formation of skyrmion lattices [13, 128].

It seems to be evident, that the interface-induced DMI can further be tuned by the direct engineering of the interface quality through the modification of the growth conditions of the layers. Differences in the effective DMI were obtained when changing the sputter pressure [136] and deposition temperature [144]. The growth mode is additionally susceptible to the details of the seed layer for the respective interfaces. The wetting properties, roughness, crystalline order etc. of the seed layer modify the growth condition for the on-top deposited layer. Therefore, even in nominally symmetric systems, differences between the bottom Pt top layer are anticipated [134], since they are seeded either on metal oxide substrates (occasionally with a Ta buffer layer) or on the thin ferromagnetic interlayer. This results in differently large DMI vectors at top and bottom Pt/Co interfaces even in symmetric Pt/Co/Pt trilayers leading to a partial compensation of the uneven top and bottom contribution. Similarities to reported roughness-induced exchange bias differences at top and bottom interfaces in Co/CoO/Co [145] emerge. The impact of the growth mode on the effective DMI of Pt/Co bilayers has been apparent by the enhancing effect of the introduction of a Ta buffer layer [138]. Consequently, the stack order inversion alters growth conditions as well, which results in a noticeable reduction of the DMI when growing the Co/Pt bilayer on the comparably rough metal oxide substrate, as e.g. by a factor of up to 0.63 shown in Pt/Co/MgO systems

[102].

Many Pt/Co bilayer systems were studied using different metal oxide layers as a capping layer. A recent comparison of experiments and ab initio calculations [53] suggests a DMI contribution arising from a Co/MgO interface parallel to that of the Pt/Co interface and comparable in strength. Additional possibilities to control both the magnitude and sign of the Dzyaloshinskii-vector are seen in the oxidation level of the adjacent MO layer [146]. Experimental indications of a oxidation level-controlled DMI were found in a study of Pt/Co bilayers capped with an oxidized Gd wedge [139]. Therefore, the ability to precisely engineer the FM/MO interfaces may offer an exciting option to tune the DMI strength. However, the role of the FM/MO interface for the total DMI strength is not yet fully understood.

Analogous to the search for materials with a large spin-Hall angle (sec. 2.2.1), the desire for materials with a large interface-induced DMI led to a screening of different systems. The study of a number of heavy metals (HMs) such as Ta, TaN, W and Hf [15, 141, 147] has so far not provided a superior replacement for Co/Pt based systems. In these studies the usage of usually annealed CoFeB ferromagnetic layer implies an additional complexity for the interpretation of the results, because the migration of the light element boron induces undefined changes of the interface properties [148].

It has to be stated that the theoretical understanding of the interface-induced DMI is only at the beginning. The qualitative explanation of experiential results gained from complex real systems by DFT calculations [53, 146, 149] presuming idealized conditions is deemed a sophisticated task. As a close relation of the interface-induced DMI to the Rashba effect [150] is pointed out.

Symmetry breaking of any kind and of any surface/interface essentially causes DMI contributions. This highlights the importance of the microstructural details. At the current stage, the attempt to understand the experimentally determined DMI value of a hypothetical TaN/CoFeB/GdOx system bears too many unknowns, e.g the contribution of each individual element for the DMI. Furthermore, the positioning of elements in the real system is not well defined due to element migration, different oxidation levels, interface roughness etc. Therefore a great importance lies in empirical studies starting with systems containing a manageable amount of elements. This requires the development of a defined and unambiguous quantification method. In the following different approaches will be presented that were introduced only a few years ago and are still under revision. Due to a so far missing standard all above mentioned findings include a certain methodological uncertainty. The table 2.3 contains a selection of so far reported results on chiral surface/interface-induced DMIs in asymmetrically sandwiched ferromagnetic films that also show a wide spread for Pt/Co bilayers and will be further discussed together with the results of this work in sec. 6.1.

2.3.4 Quantification of the interface-induced DMI

Two major approaches rapidly evolved with the demand of the quantification of the interface-induced DMI constants. The most commonly used method is based on an expected DMI induced asymmetric magnon dispersion (AMD). The frequency shift obtained in the asymmetrically sandwiched ferromagnets for antipodal magnons is attributed to the magnitude of the DMI vector D [151]

$$\Delta f = \frac{2\gamma D}{\pi M_S} k_x \quad (2.20)$$

involving the magnon wave-vector k_x , the saturation magnetization M_S and the gyro-magnetic ratio γ of the material. The frequency shift is usually measured by Brillouin light scattering (BLS) [125, 126, 137–139, 152, 153]. It has also been shown that time resolved scanning Kerr microscopy (SKM) [142] or all-electrical propagating-spin-wave spectroscopy [102] can be employed to that end.

The second quasi-static route evaluates asymmetric features in field-driven domain growth when overlaying the DMI field with an external field [134–136, 139] usually observed by wide-field Kerr microscopy. This approach provides access to the DMI field, Eq. (2.17), that requires all micromagnetic parameters to be properly scaled to the DMI constant. The approach of the asymmetric domain growth (ADG) has not prevailed yet despite its straightforward experimental feasibility that also allows the investigation of materials with large damping. This work elaborates the analysis of this approach and clarifies recently discussed ambiguities [139, 154], which is described in sec. 4.2 in detailed.

Further proposals for the determination of the DMI constant involve the analysis of characteristic length scales of magnetic structures. Provided that all other micromagnetic parameters are explicitly known, which is rarely the case, the DMI can be deduced from the typical dimensions of magnetic structures such as the skyrmion diameter, domains spacing, chiral modulations. Several versions of this approach can be found in the recent literature. Often the exchange parameter is either assumed to be equal to the bulk value or used as a free fit parameter as in the reports evaluating the domain spacing [54] or the skyrmion diameters [155] respectively.

Furthermore, a tilted equilibrium position of a DW in a magnetic stripe that is caused by the DMI in combination with a transverse field is predicted [155]. From the linear dependence of the tilt angle on the transversal field, the DMI constant can be calculated. A experimental evidence of this effect was recently found in current-induced DW motion experiments [16]. It was further proposed that the study of the field stability of 360° DWs or so-called winding pairs, that are stabilized by the DMI, can be used for the DMI quantification [41]. The annihilation field of the winding pairs is obtained in a sequence of hysteresis loops with increasing maximum field amplitude and can be related to the DMI constant by micromagnetic simulation (sec. 4.2.3). These mostly unverified approaches are additionally heavily

compromised by pinning that is an inherent property of all studied systems. The ongoing search for alternative quantification methods exemplifies the inchoate state of the field.

2.3.5 Levy-Fert three-site model including roughness

Sputtered finely polycrystalline thin magnetic films will have various contributions to the chiral DMI, which may compete and eventually average to a vanishing twisting effect, in particular if different surfaces of rotated grains or surface defects like steps cause alternating twisting effects on the magnetization.

A random distribution of local DMI terms along the surface with alternating signs and directions of Dzyaloshinskii-vectors \mathbf{D} in the microscopic local DMI, Eq. (2.17), between local spins may average to a very weak effective chiral coupling.

To provide a cartoon picture of the possible averaging mechanism, the roughness influence on the DMI strength is evaluated by a modified Levy-Fert three-site model [156]. To calculate the dependence of the DMI strength on the degree of disorder, the disorder/roughness has been introduced as a Gaussian distribution of the interatomic distances around an ideal lattice constant a with standard deviation σ [157]

$$\mathbf{D}_{ij}(\mathbf{R}_{li}, \mathbf{R}_{lj}) \propto \frac{(\mathbf{R}_{li} \cdot \mathbf{R}_{lj}) (\mathbf{R}_{li} \times \mathbf{R}_{lj})}{|\mathbf{R}_{li}|^3 |\mathbf{R}_{lj}|^3 R_{ij}}. \quad (2.21)$$

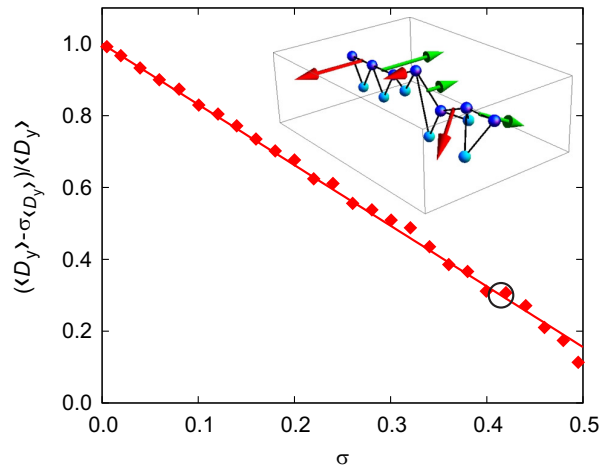


FIGURE 2.6: DM vector calculated on the basis of 3-sites-model for a linear chain of magnetic atoms (blue/dark gray spheres) on the heavy metal substrate (light gray spheres) as a function of the degree of disorder. The disorder is modeled using Gaussian distribution of interatomic distances with standard deviation σ . The larger σ , the stronger disorder. The normalized expression $D_{\text{eff}} \sim \langle D_y \rangle - \sigma_{\langle D_y \rangle}$ as function of the roughness *sigma* shows a significant reduction with increasing σ . Note that this can serve as a qualitative picture, even though the estimated roughness of $\sigma = 0.42$ at 60% reduced DMI strength in our samples is reasonable. The inset exemplifies a distribution of the DM vectors.

\mathbf{R}_{li} , \mathbf{R}_{lj} are the distance vectors from the impurity l to corresponding FM sites, R_{ij} the distance vector between FM sites, while \mathbf{D}_{ij} is corresponding DMI vector.

Based on the calculation results obtained by E. Vedmedenko, the average of the y -component of D is found to be constant for all σ while the standard deviation of this component linearly increases. It is concluded, that the effective DMI constant D_{eff} , which is relevant e.g. for the altered DW motion in the experiments, is related to the reduced average of the D_y -component by its standard deviation $D_{\text{eff}} \sim \langle D_y \rangle - \sigma_{\langle D_y \rangle}$. This results in an almost complete destruction of the DMI at larger disorder as one can see qualitatively from Fig. 2.6. Even though a constant average D_y should result in the maintenance of chiral order, the large local deviations diminish the effective DMI. The inset in Fig. 2.6 shows the distribution of DM vectors in a linear chain of atoms with disorder. Only nearest neighboring magnetic atoms (blue/dark gray spheres) have been considered in the calculations. Each pair has been coupled via a nearest neighboring heavy metal atom (cyan/light gray spheres). For the sake of comparison three left atomic bonds are completely ordered in a hcp-like manner.

Chapter 3

The CrO_x/Co/Pt sample system

Here, the aim is to investigate the intensely studied Co/Pt bilayer in the so far unexplored conjunction with CrO_x as a metal oxide (MO). The system joins the family of so far investigated //Pt/Co/MO systems based on aluminum, magnesium and gadolinium oxide materials [53, 125, 126, 138–140]. The introduction of CrO_x as MO increases the system variety in order to contribute to the clarification of an enhanced DMI strength of MO interfaces [53, 146]. Alike the other MOs, CrO_x induces perpendicular magnetic anisotropy (PMA) in the ferromagnetic layer [79].

With the here employed stack inversion, i.e. CrO_x placed as seed layer for the Co/Pt bilayer, important technology-relevant criteria like electric accessibility and easy film preparation are assured. It implicates reduced optimization efforts of the MO layer preparation and the avoidance of interactions at the Co/MO interface during deposition. With the noble metal Pt as the stack termination a straight-forward contacting possibility including multi-step photolithography and deposition processes is provided.

The Pt top layer thickness is chosen as thin as possible. A Pt layer thickness of 2 nm is just sufficient to serve as an impermeable oxidation barrier for the buried Co layer. The thin metal layer with a comparably large optical transmittance is beneficial for Kerr microscopy investigations. Furthermore, a low magneto-resistive shunting in the magnetotransport investigations is achieved.

The cobalt layer thickness is varied to assess the scaling of micromagnetic and magnetotransport properties.

The technical details of the experimental procedure applied to the samples are described in sec. 3.1. The results of the structural investigations are shown in sec. 3.2. The detailed characterization of the complete micromagnetic and magnetotransport properties is presented in the chapters 4 and 5 respectively.

3.1 Experimental techniques

A sample series of //CrOx(5 nm)/Co(t_{Co})/Pt(2 nm) was magnetron-sputtered at room temperature on oxidized silicon substrates with an argon pressure of 10^{-3} mbar in a DCA sputter system. Samples with the cobalt layer thickness t_{Co} in the range 0.6 and 1.0 nm are perpendicularly magnetized and obtain full remanence. The MO layer was RF sputtered at a deposition rate of 0.011 nm/s, while the Co and Pt metal layers were DC sputtered at 0.050 nm/s and 0.080 nm/s respectively.

Two samples with //Pt(2 nm)/Co(1.2 nm)/Al(2 nm) were prepared with a DC-sputtered Al top layer at 0.033 nm/s and subsequent plasma-oxidation for 35 s. One of the reference samples was annealed in vacuum at 250 °C for 15 minutes. These samples are similar to the typically non-inverted systems stacks reported in the literature and are prepared to assist the comparison of the results for the //CrOx/Co/Pt samples to the reported data.

Further samples altering the growth conditions of the CrOx seed layer were prepared to judge magnetic contributions of the CrOx layer due to its possible anti-ferromagnetic properties. In case of the first reference sample, only the CrOx thickness is increased to 100 nm, while the second reference sample is intended to obtain crystalline properties. By reactive evaporation on a sapphire substrate at 850 K with an oxygen background pressure of 10^{-5} mbar an epitaxial growth of crystalline chromium oxide is achieved.

Depth profiles revealing the details of the stack architecture (sec. 3.2) were obtained by both X-ray reflectometry (XRR) and Auger-electron spectroscopy (AES). The AES profiles were acquired by S. Facsko in a MicroLab 350 system by Thermo Scientific by removing the material with a 3 keV Ar⁺ ion beam sputter gun scanned over an area of $1 \times 1 \text{ mm}^2$ in steps of 10 s and measuring the corresponding Auger electron yields of the recorded elements with a 10 keV e-beam scanned over an area of $10 \times 10 \text{ }\mu\text{m}^2$.

The X-ray reflectometry measurements performed by A. Scholz in the the specular angle range between -0.1 and 11.9° in steps of 0.06° integrating for 3 s per step. The obtained density profiles of the samples from simulations with the PANalytical software X'pert reflectivity were subsequently rescaled to electron density profiles.

The crystalline order was investigated by standard X-ray diffraction techniques in a PANalytical powder Co-X-ray diffractometer in collaboration with T. Kosub. The 2θ -scans were rescaled to the wave number k according to Bragg's law.

Elementary magnetometry (sec. 4.1) is carried out to determine the saturation magnetization M_S and the anisotropy energy constant K_{eff} . The remanent magnetization and its temperature dependence for the extrapolation of the Curie temperature were measured by VSM (Quantum design PPMS and MPMS). The obtained magnetization value in units of

emu is normalized to the volume of the sample piece, by taking the nominal deposited cobalt layer thickness and the area evaluated utilizing an image measurement tool from optical microscopy. Since the low signals of ultra-thin films are dominated by paramagnetic contaminations, that typically occur in VSM devices, the easy and hard axis hysteresis loops were measured by anomalous Hall magnetometry. The anomalous Hall resistance obtained at remanence is scaled to the remanent magnetization value obtained in the VSM measurement. Angular-dependent ferromagnetic resonance (FMR) measurements performed by S. Stienen in a cavity FMR system (Bruker ELEXSYS) at the resonance of 9.4 GHz in magnetic fields up to 1.5 T are used to confirm the determined anisotropy field and evaluate the dynamic properties. The low magnitude of the signals are hardly measurable in a vector network analyzer-FMR setup using a coplanar waveguide for the excitation of the magnetization precession. In contrast to the cavity FMR, the excitation frequency can be tuned in this setup over a large range, which is required to assess the FMR damping properties of the sample.

Wide-field magneto-optical Kerr microscopy (evico magnetics) adjusted to the polar Kerr-contrast [114] is used to obtain the field- and/or current-driven evolution of magnetic domains in the samples.

Field-driven DW creep motion (sec. 4.2.1) is induced by an external easy-axis magnetic field parallel to film normal \hat{z} with a maximum magnitude of $H_z = 20$ mT provided by a home-made air-coil electromagnet driven by a Keysight Sourcemeter providing defined rectangular current pulses of widths down to $\Delta t = 2$ ms.

The DW velocities v are determined from the traveled distance s measured from differential Kerr-images taken from the initial and final states before and after the application of an H_z -pulse with the width of Δt . A python code developed by H. Fuchs was used for the evaluation of the DW velocities of circularly expanding domains, which averages the propagation distance in a certain time interval over eight angles around the circumference of the domains. The respective Kerr-images were taken and analyzed by D. Stein during his internship at the IFW Dresden.

The asymmetric domain wall growth is induced by the simultaneous application of external magnetic fields perpendicular to the film normal with a maximum magnitude of $H_x = 250$ mT. Great caution was given to avoid a misalignment of the sample with respect to the hard axis field, that causes an additional H_z component. To cancel any remaining effect of a possible misalignment the respective velocities values for $\uparrow\downarrow$ and $\downarrow\uparrow$ DWs from both up and down domains were averaged. With the proper analysis, the asymmetry ratio of the DW velocities reveals the effective DMI constant D_{eff} (sec. 4.2).

The extend films were structured into micro-stripe layouts by optical photolithography for

the purposes of magnetotransport measurements and bubble domain generation. The photoresist (MicroChemicals, AZ-5214E) was exposed using a direct LASER writer (Heidelberg, DWL66). The exposed resist was removed by the metal-ion -free developer AZ-MIF and subsequent DI water rinsing to avoid contaminations.

The unprotected film areas were subsequently Ar-Ion-beam etched (Roth&Rau, IONSYS500) at 200 eV. The complete removal of the conducting layers was assured by the end-point detector (HidenAnalytical, IMP-EPD) monitoring the sputter products with an in-situ mass spectrometer. The remaining photo-resist was removed in ultra-sonic acetone and IPA bath and subsequent gentle O₂-plasma for 1 min.

The characteristic dimensions of the individual microstripe devices determined by the details of the photolithographic process are measured in a scanning electron microscope (SEM) (Raith e-line).

For the generation of circular magnetic objects in the scheme of Jiang et al. [3] the films were patterned into stripes of 60 μm width with a constriction to 3 μm . Wire connections to the contact pads were established with silver paste. Circular magnetic objects are expelled from the constriction area upon simultaneous application of current pulses with an adjustable magnitude of up to 2 mA and external easy axis magnetic field. The object diameter measured from the Kerr microscopy images can then be related to the exchange parameter A (sec. 4.3).

In preparation of the magnetotransport measurements silver paste was applied to the contact pads to provide good electric contact of the thin-films to the nonmagnetic short travel Au-probes (Feinmetal) of the sample holder. The measurements were performed in a Resistance Tensormeter setup developed by T. Kosub. For the electrical characterization the samples are excited with a harmonic alternating voltage of up to 10 V at $f = 392.673$ Hz. A subsequent FFT analysis of the signal immediately yields the real and imaginary part of the signal harmonics of arbitrary order. Magnetoresistance effects and spin-orbit torques (chapter. 5) are measured in a water-cooled electromagnet with active feedback control providing external magnetic fields with maximum magnitudes of 2 T.

Usually several curves are averaged to minimize thermal drift and enhance the signal-to-noise ratio. When working with thermally oxidized silicon substrates, the measurements are performed in a light protected setup to avoid photoelectric contributions [158]. A part of the magnetotransport measurements were performed by L. Heinze during her summer student internship at the HZDR.

3.2 Structural characterization

Structural characterization is carried out to address the details of the interfaces. Given the different sample processing strategies or growth conditions including post-annealing of the sample, the Co/Pt interface quality might vary and has to be investigated. The growth conditions are altered by depositing thin platinum either directly on the substrate or on a CrOx layer coated with cobalt of varying thickness. The effects of annealing are also analyzed as it is a common processing step [20, 53, 106, 140].

To gain information on the interface quality, depth profiles from Auger electron spectroscopy (AES) and the analysis of X-ray reflectometry (XRR) are measured for four representative samples. Fig. 3.1a shows the results of the modeled X-ray reflectograms. The modeling is only possible by the assumption of a large electron density variation in the region

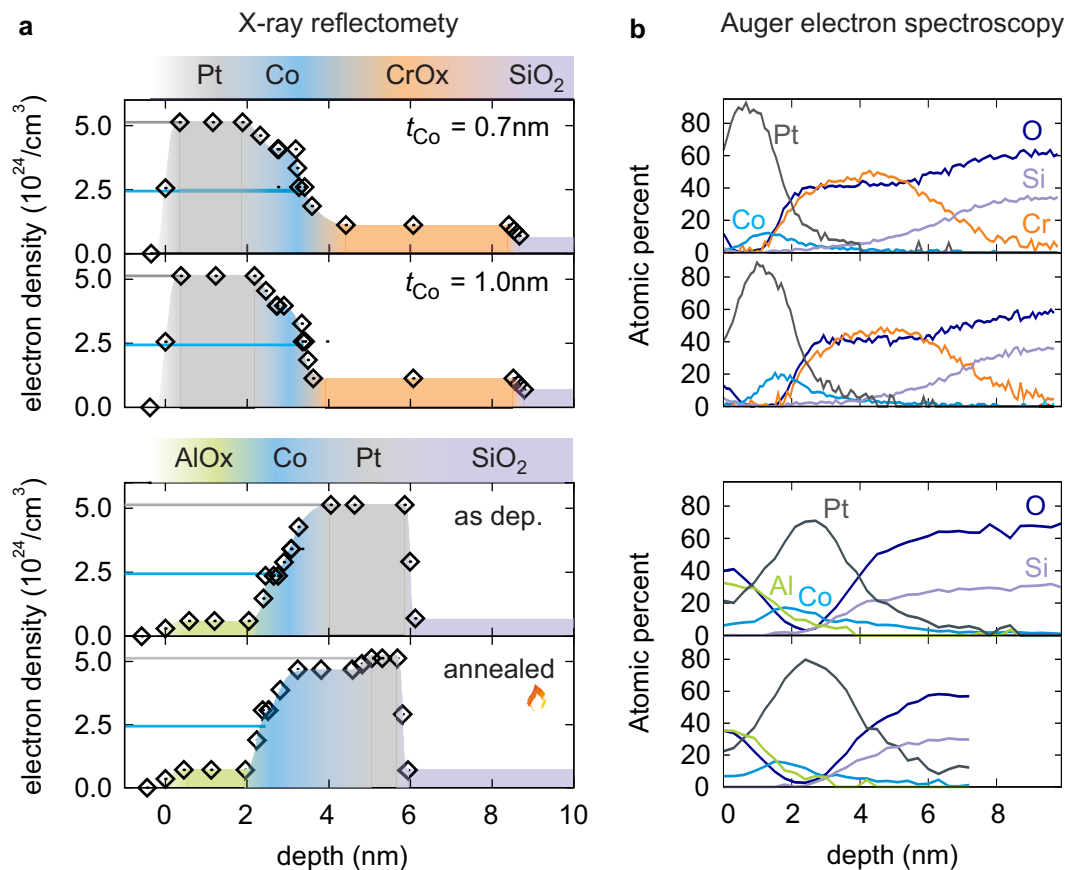


FIGURE 3.1: Depth profiles from X-Ray reflectometry (XRR) analysis (a) and Auger electron spectroscopy (AES) (b) for //CrOx/Co(t_{Co})/Pt and the as deposited and post-annealed //Pt/Co/AlOx reference stacks respectively. A missing plateau at the bulk electron density of Co (blue line) in the XRR depth profile and almost identical peak positions of Pt and Co in AES depth profiles suggest a Co/Pt interface roughness of the order of cobalt layer thickness in all cases, i.e. a comparable Co/Pt interface quality independent of the stack order, cobalt thickness or post annealing.

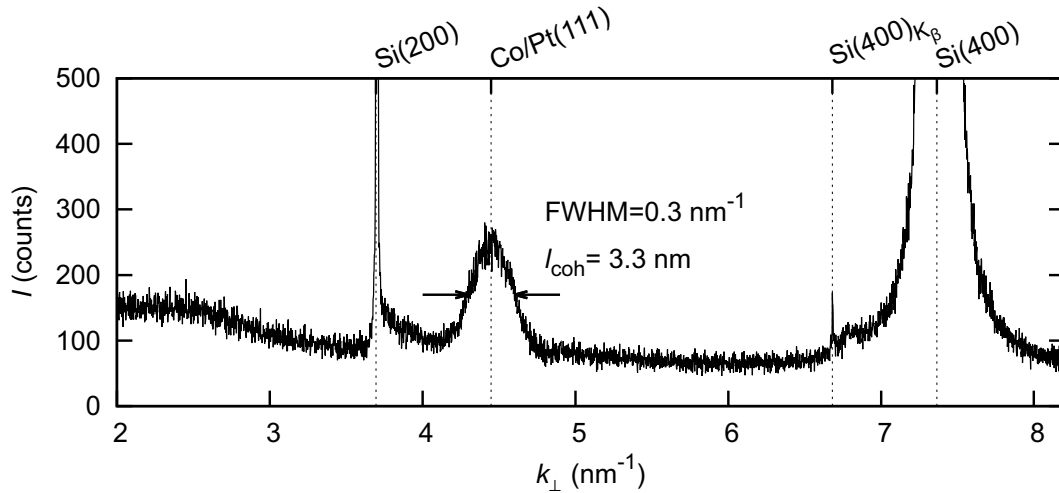


FIGURE 3.2: X-Ray diffractogram of an amorphous a-Cr₂O₃(5 nm)/Co(1 nm)/Pt(2 nm) trilayer. According to the half-width of the Co/Pt(111) peak the value of the coherence length l_{coh} of the Co/Pt bilayer is determined to be 3.3 nm, which roughly validates the nominal film thickness of 3 nm of the bilayer.

between the MO and Pt. There is no apparent plateau at the electron density bulk value of cobalt suggesting that the interface roughness and the layer thickness are of the same order. The depth profiles measured by AES support this finding. Here the peaks of Co and Pt are at almost identical positions and of equal width as seen in Fig. 3.1b. Furthermore, the AES results indicate, that the stoichiometry of the Cr₂O₃ target is not fully transferred to the sample, where the fraction of the Cr is favored.

From the structural characterization it is concluded that the Co/Pt interface roughness is significant in the investigated samples. Moreover, within the resolution limits of the measurements, the interface roughness appears to be almost independent of the cobalt thickness, annealing, or stacking order. Although confirming the order of magnitude of the layer thicknesses, both techniques cannot provide a desired (sub-Å) accuracy. Therefore, the nominal cobalt layer thicknesses were used in the data analysis.

The X-Ray diffractogram of a Co/Pt bilayer grown on a 5 nm thick amorphous Cr₂O₃ seed layer shown in Fig. 3.2 only contains peaks originating from the silicon substrate and one peak that is related to the Co/Pt bilayer. Its coherence length l_{coh} of 3.3 nm agrees well with the bilayer thickness.

Chapter 4

Complete micromagnetic characterization

Here, an approach is put forth to determine the full set of the micromagnetic parameters of asymmetrically sandwiched ferromagnets (FM) including the DMI strength and the exchange parameter by relying on quasi-static measurements [159] as alternative to typically used dynamic approaches [151, 160]. A measurement routine is developed which, in conjunction with the proper theoretical framework, allows to obtain the value of the DMI strength D_S from a sequence of Kerr microscopy measurements without ambiguous assumption on the exchange constant. When the DMI strength is determined, the exchange parameter A can be readily deduced via the evaluation of characteristic diameters of circular magnetic objects. In order to employ the correct theoretical framework for the analysis, the observed localized homochiral objects should be classified into either skyrmions or chiral magnetic bubbles, which can be achieved by following the scaling behavior of the object size with respect to the ferromagnetic layer thickness.

In the following the full sequence of measurement and analysis steps for the determination of the complete set of micro-magnetic constants from quasi-static methods is described, starting with the determination of the saturation magnetization M_S and the anisotropy energy constant K_{eff} by standard magnetometry (sec. 4.1) and followed by the quantification of D_S and A in sec. 4.2 and 4.3 respectively. The results are summarized in sec. 4.4.

4.1 Magnetometry

4.1.1 Static investigation

The full hysteresis loops (Fig. 4.1a,c) are obtained from anomalous Hall effect (AHE) measurements. As the hysteresis loops measured by vibrating sample magnetometry (VSM) are susceptible to magnetic contaminations adding an unknown paramagnetic offset to the hysteresis loops, only the remanent magnetization values are taken into account. Apart from a small linear contribution of 10 mΩ/T attributed to the ordinary Hall effect of the platinum

layer, all studied samples show full remanence and the determined magnetization value is a direct measure of the saturation magnetization M_S for these samples under this condition. Therefore it is justified to use the remanent magnetization in easy axis direction as the saturation magnetization value of the samples.

To calculate the hard axis loops from Hall-loops measured in tilted geometry (see Fig. 4.1b), the following geometrical relations are employed. In the tilted geometry the field component, that is effectively applied in the direction of the hard axis direction of magnetization, is equal to the projection of the external field vector onto the film plane, $H_x = H_{\text{ext}} \cdot \cos \alpha$. The angle $\alpha = \arccos(H_c/H_c^t)$ is calculated from the ratio of the respective switching fields of easy axis and tilted hysteresis loop. Given that the samples exhibit full remanence the inplane magnetization component at any field point can be deduced from the following geometrical relation

$$M_x(H_x) = \sin \left[\arccos \left(\frac{R^H(H_x)}{R^H(H_x = 0)} \right) \right], \quad (4.1)$$

with the ratio of the field-dependent Hall resistance $R^H(H_x)$ to its value obtained at zero field in the fully magnetized remanent state.

The anisotropy field $\mu_0 H_K$ is deduced from the hard axis loop since it is equal to the integral of $1 - |M(\mu_0 H_{\text{ext}})/M_S|$ according to the definition of the effective anisotropy energy constant K_{eff} , Eq. (2.12a).

The following temperature dependent properties were obtained by vibrating sample magnetometry. By fitting the temperature dependent magnetization curves (see Fig. 4.2a) to the

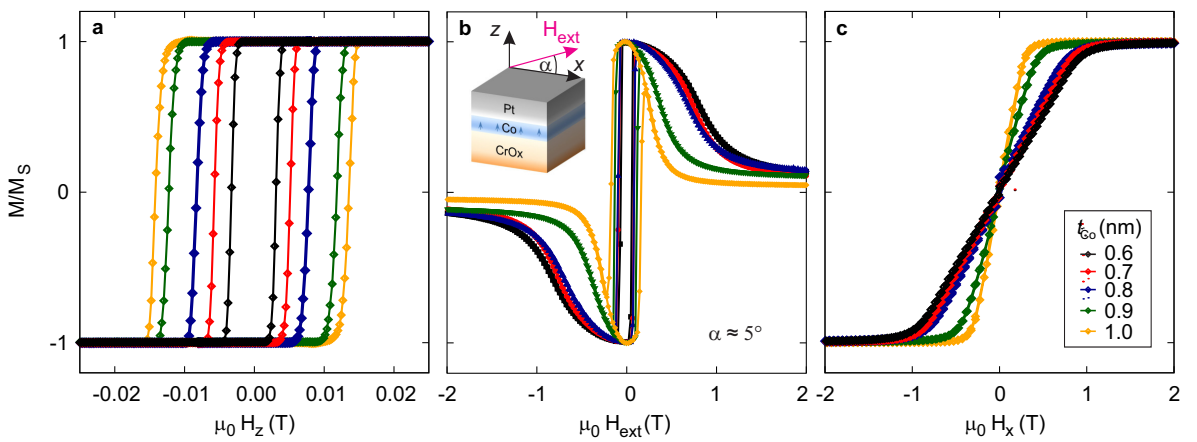


FIGURE 4.1: Normalized AHE measurements with the field applied (a) parallel to the surface normal (\hat{z} , $\alpha = 90^\circ$) and (b) under an angle α of about 5° with respect to the \hat{x} axis (see sketch). The hysteresis loops of the //CrOx/Co(t_{Co})/Pt trilayers in (a) easy and (c) hard axis direction of the magnetization are obtained, after a rescaling of the curves in panel (b) according to Eq. (4.1)

following expression

$$M(T) = M_S [(T_C - T)/T_C]^\beta, \quad (4.2)$$

the Curie temperatures T_C are extrapolated. A value of 0.75 for the critical exponent β is determined from the fit for all samples. The analysis suggests a strong reduction of T_C from the bulk value of $T_C^b=1394$ K in the thin films.

During cool-down from 400 K to 100 K the coercive fields H_c of three samples with different Cr_2O_3 seed layers were tracked in VSM by constantly sweeping the field. Fig. 4.2b shows that left and right switching field branches are symmetric in the whole temperature range not only for the sample with 5 nm thick amorphous a- Cr_2O_3 but also in the case of the much larger thickness of 100 nm. This clearly proves the absence of anti-ferromagnetic properties in the a- Cr_2O_3 layers that otherwise would induce an exchange bias (EB) effect. As confirmed by XRD (Fig. 3.2), crystalline growth is not achieved in the employed deposition regime. As suggested by the AES depth profiles, the stoichiometry Cr_2O_3 is not achieved in the amorphous samples, which could be the reason for the absence of magnetoelectric properties.

In contrast, the EB effect is very obvious in the reference sample with crystalline α - Cr_2O_3 . The hysteresis loop is shifted up to 400 mT below the blocking temperature of about 305 K. The absence of magnetoelectric properties in a- Cr_2O_3 layers down to temperatures of 100 K

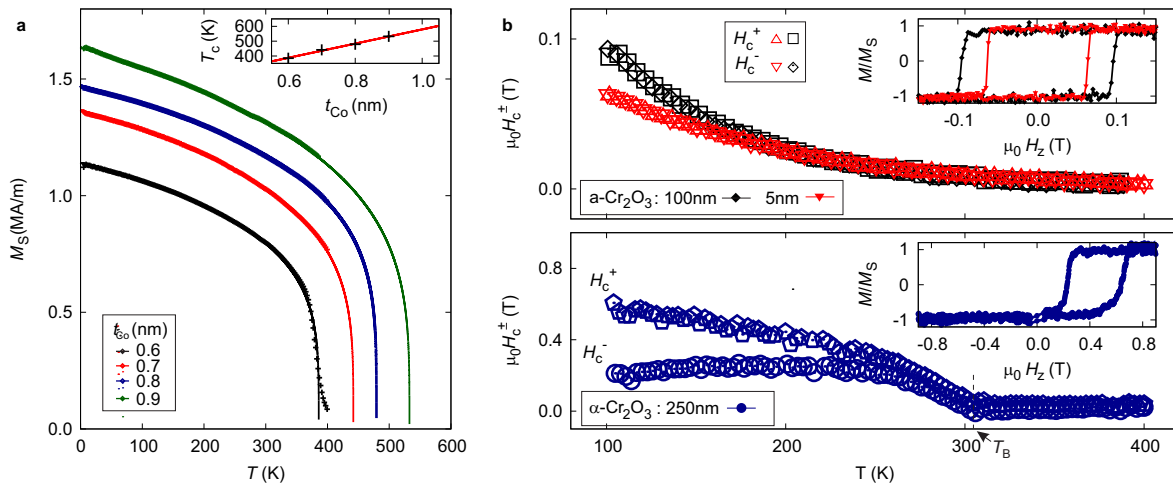


FIGURE 4.2: (a) Temperature dependence of the magnetization M_S allows for the extrapolation of the Curie temperatures. (b) The study of the temperature depend coercive fields H_c^\pm of different Cr_2O_3 seed layers reveals possible anti-ferromagnetic properties. Amorphous a- Cr_2O_3 seed layer with thicknesses of 5 nm and 100 nm show symmetric switching behavior, i.e. the left H_c^- and right H_c^+ coercive fields are equal. For crystalline α - Cr_2O_3 seed layers sizable loop shifts of the easy axis hysteresis loop by an exchange bias field H_{EB} up to the blocking temperature T_B of 305 K clearly indicated anti-ferromagnetic properties.

confirms the former finding that a strong perpendicular magnetic anisotropy (PMA) induced by Cr_2O_3 does not originate from the perpendicular exchange coupling effect at crystalline $\alpha\text{-Cr}_2\text{O}_3/\text{FM}$ interface [161].

The usage of amorphous chromium oxide ($\text{a-Cr}_2\text{O}_3$) for spin-orbit effect studies has hitherto been neglected, due to its possible magneto-electric properties and related effects. The strong PMA induced by Cr_2O_3 allows the variation of the FM thickness in a reasonably large range. The aim is to preserve perpendicularly magnetized films from the same sandwiched system over a significant large range. Thus, the possibility to adjust the magnetic properties is provided and the influence of the interfaces can be studied.

4.1.2 Ferromagnetic resonance

The anisotropy field H_K obtained from the hard axis loops determines the ferromagnetic resonance condition, that can be calculated with the Kittel formula [162]

$$f_{\text{res}} = \frac{\gamma}{2\pi} \sqrt{B(B - \mu_0 H_K)}. \quad (4.3)$$

The positions of resonant lines in frequency and angle space are calculated for the sample series of $\text{//CrOx/Co}(t_{\text{Co}})\text{/Pt}$ trilayers. Fig. 4.3a shows the simulated resonant lines for the $\text{//CrOx/Co}(1)\text{/Pt}$ sample for different angle θ between easy axis of magnetization and external field up to the maximum field magnitude provided by the device. The colored areas mark the X-, Q- and K-band frequency ranges of typical FMR cavities. Using a X-band FMR cavity with a excitation frequency of 9.4 GHz the resonance condition is fulfilled only in a small angle interval of about $\pm 15^\circ$ around the hard axis direction. Fig. 4.3a shows the simulated resonance lines for all $\text{//CrOx/Co}(t_{\text{Co}})\text{/Pt}$ in easy and hard axis configuration. The non-aligned modes were than obtained in angular-dependent FMR measurements. The expected low signal is of the order of the O_2 -resonance line, that is also detected in the X-Band cavity. Fig. 4.3c maps the FMR absorption on the external field $\mu_0 H_{\text{ext}}$ and angle θ . The red line indicates the simulation results and show agreement with the measurements. Hence, the anisotropy field H_K obtained in the static investigations is verified.

The very broad resonances lines are of a non-Lorentzian shape, exemplarily shown in the inset of Fig. 4.3c for $t_{\text{Co}} = 0.9$ nm. Hence, a fit of the resonance line using standard Lorentzian shape for a single or simple resonance could not be performed. The line broadening suggests an angular distribution of the anisotropy axes of the polycrystals of the film. In addition, the inhomogeneities of the film affects e.g. the damping behavior and also contributes to the broadening. Due to scarcity of data the different contributions can not be assess here, since this would require measurements of the frequency-dependent evolution of the line shapes.

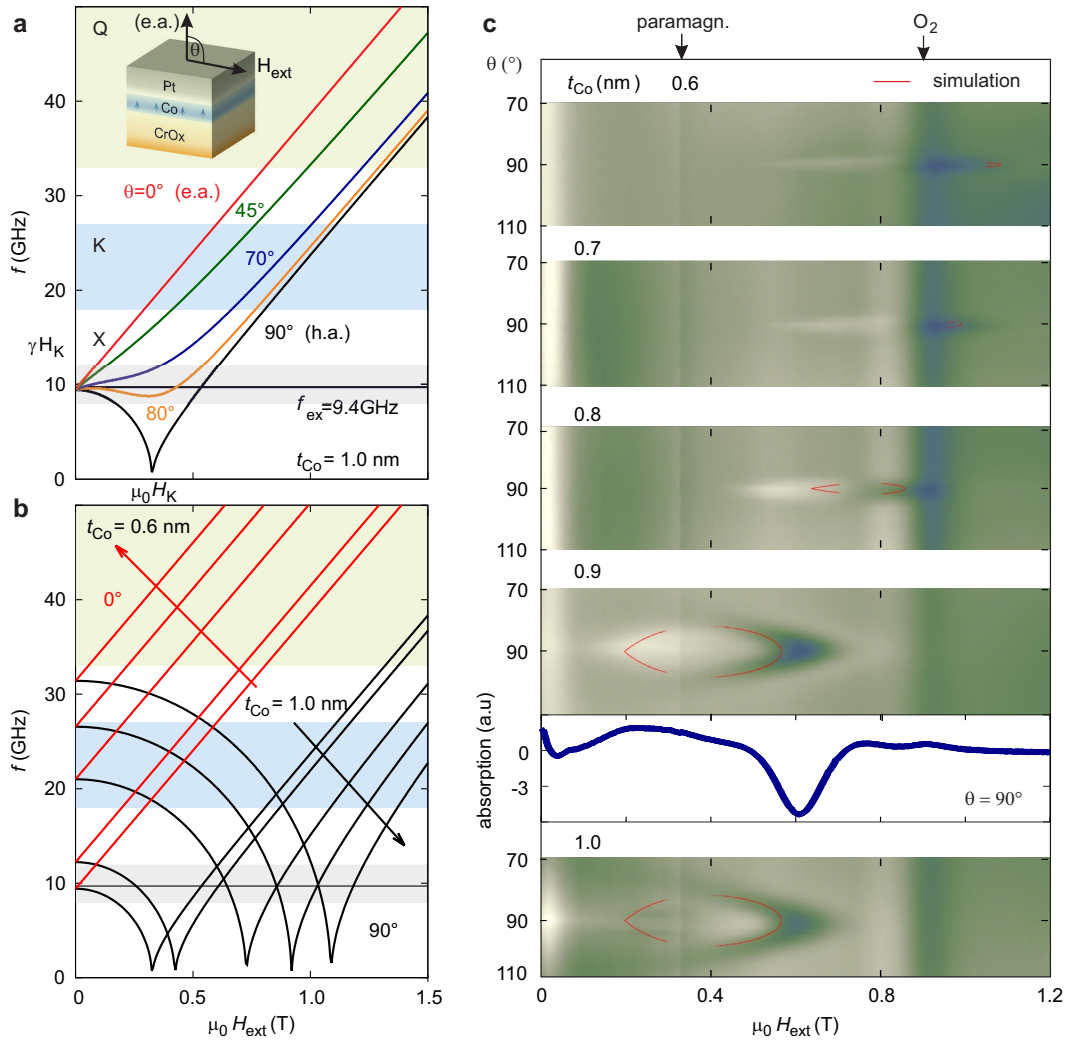


FIGURE 4.3: Ferromagnetic resonance in //CrOx/Co(t_{Co})/Pt trilayers simulated with a software provided by J. Lindner for (a) different angles θ with respect to the easy axis of magnetization and (b) different t_{Co} . In X-Band FMR cavity measurements performed by S. Stienen with an excitation frequency of $f_{\text{ex}} = 9.4$ GHz only the non-aligned mode can be obtained in a small angle range around $\theta = 90^\circ$. (c) The position of the nonaligned modes obtained in the FMR absorption maps in $(\theta, \mu_0 H_{\text{ext}})$ space agree well with the simulations, verifying the statically determined anisotropy field H_K . A fit of the broad and distorted resonance line (see inset) could not be performed.

4.2 DMI quantification

The DMI quantification method used here relies on the analysis of the field-driven evolution of domain patterns. The remagnetization process in the studied samples is generally governed by the nucleation of domains and subsequent propagation of DWs through the entire film.

The nucleation field distribution is very sharp at small t_{Co} and broadens for larger thicknesses accompanied by an increase of nucleation sites. For similar Pt/Co/Pt systems an asymmetric nucleation for opposite initial magnetization saturation states at defects has been reported

[163], which might stem from the recently discussed step-edge-induced DMI [121].

In a certain field range, that is different for each sample, DW motion is observed such that it does not develop overhanging wall sections. For larger t_{C_0} this field range starts to overlap with the nucleation field distribution, so that in at higher fields it can not be discerned, whether a sample area remagnetized due to nucleation or wall propagation.

The field-driven DW propagation is classified into different propagation regimes [164, 165]. With successively increasing external magnetic field the creep, thermally assisted flux flow and depinning regimes are observed until the flow motion regime is asymptotically reached. While the highly non-linear response at low fields is well understood in terms of the creep law (see sec. 4.2.1), the regimes close to the depinning are both experimentally and theoretically less clear according to Ref. [165]. Also the typical field ranges of the flow regime are hard to realize in experiment as they have to be applied as well-defined short-time large-amplitude field pulses. For these two reasons the following investigations are performed in the creep regime.

4.2.1 Field-driven domain wall creep motion

Under small magnetic fields H_z applied along the easy axis of magnetization, the DW velocities obey the creep law [164, 166]

$$v(H_z) = v_0 \exp[-\zeta (\mu_0 H_z)^{-\mu}], \quad \mu = 1/4 \quad (4.4)$$

with the value of the critical exponent μ exactly 1/4. The two creep law parameters $\ln v_0$ and ζ can be deduced from the linear fit in the $\ln(v) \left((\mu_0 H_z)^{-1/4} \right)$ representation of the data (Fig. 4.4b).

The parameters v_0 and ζ are functions of the pinning properties of the sample [166] determined by the correlation length ξ and the pinning strength δ of the disorder

$$v_0 = \xi f_0, \quad \zeta = \frac{U_c}{k_B T} (\mu_0 H_{\text{crit}})^\mu \quad (4.5)$$

with the attempt frequency f_0 , pinning barrier $U_c(\xi, \delta)$ and critical field $H_{\text{crit}}(\xi, \delta)$.

A systematic behavior of the scaling parameters as function of the cobalt thickness t_{C_0} is obtained that is similar to other intrinsic magnetic parameters. The thicker t_{C_0} and the lower the creep velocity, the more disrupted is the circular shape of the domains. The origin of this DW morphology differences lies in the increasing amount of pinning sites [164].

Both the nucleation field of the investigated pinning site and the creep motion behavior are symmetric under magnetization reversal. The observation of macroscopic DW creep inherently measures an average DW dynamics that neglects local lateral contributions due to

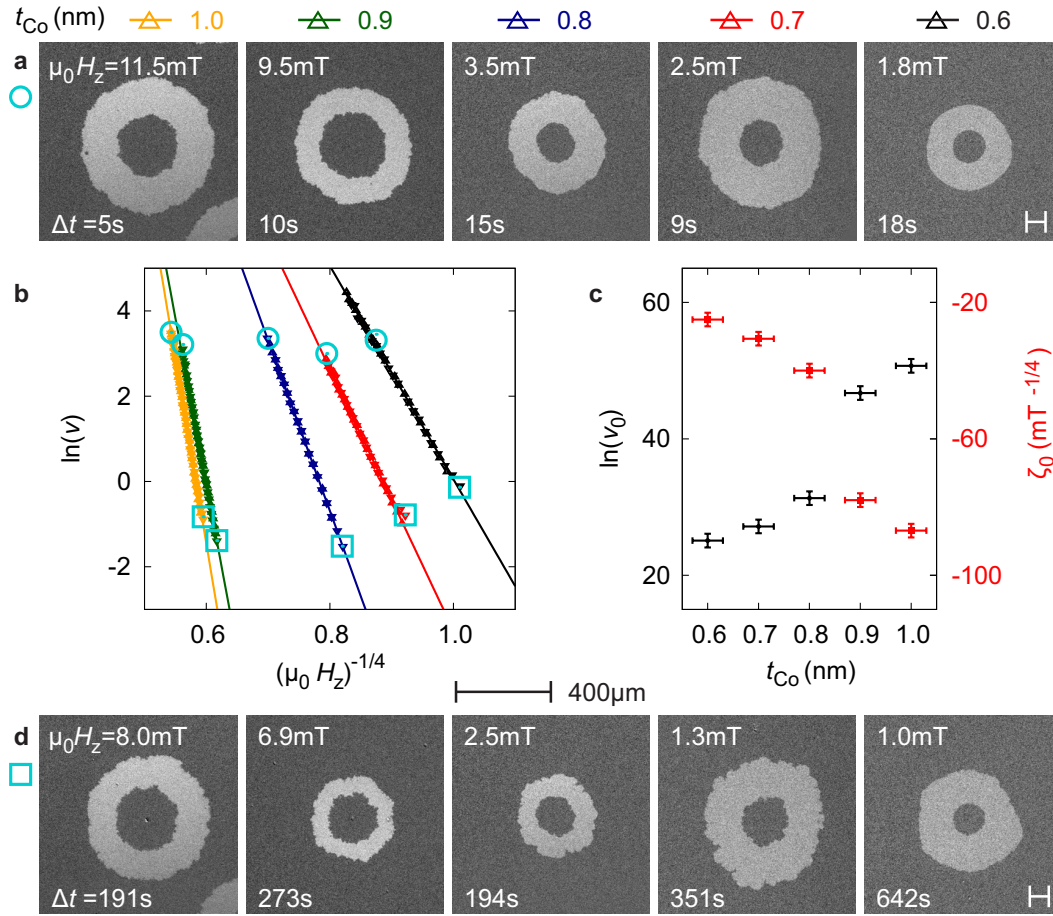


FIGURE 4.4: Panel (a) and (d) show differential Kerr images of the circular field-driven domain expansion in $\text{CrO}_x(5)/\text{Co}(t_{\text{Co}})/\text{Pt}(2)$ trilayers at high and low external magnetic fields respectively for different cobalt thicknesses t_{Co} . (b) The DW velocities in the applied field regime obey the creep law. The blue square or circle allocates the respective Kerr images to the point in the graph. (c) the parameters $\ln v_0$ and ζ_0 obtained from a linear fit.

film roughness or the granular structure. This average effectively describes an asymmetric film, where only the polar \hat{z} -axis is distinguished with an effective C_{∞} -symmetry. Locally the defects naturally break this polar simple structure and contribute to the transient pinning of the wall. Since the domain shape remains circular, there is no evidence for an effective lower symmetry and additional DMI contributions that break the C_{∞} -symmetry, which allows the description in terms of the theoretical assumption of the symmetry breaking from the \hat{z} -interface, Eq. (2.16).

4.2.2 Asymmetric domain growth

With an additional field H_x applied perpendicularly to the easy axis of magnetization, the domain growth exhibits an asymmetric distortion [167] as shown in Fig. 4.5. This is a consequence of the combined modification of the DW energy by H_x and the DMI field H_{DM} acting

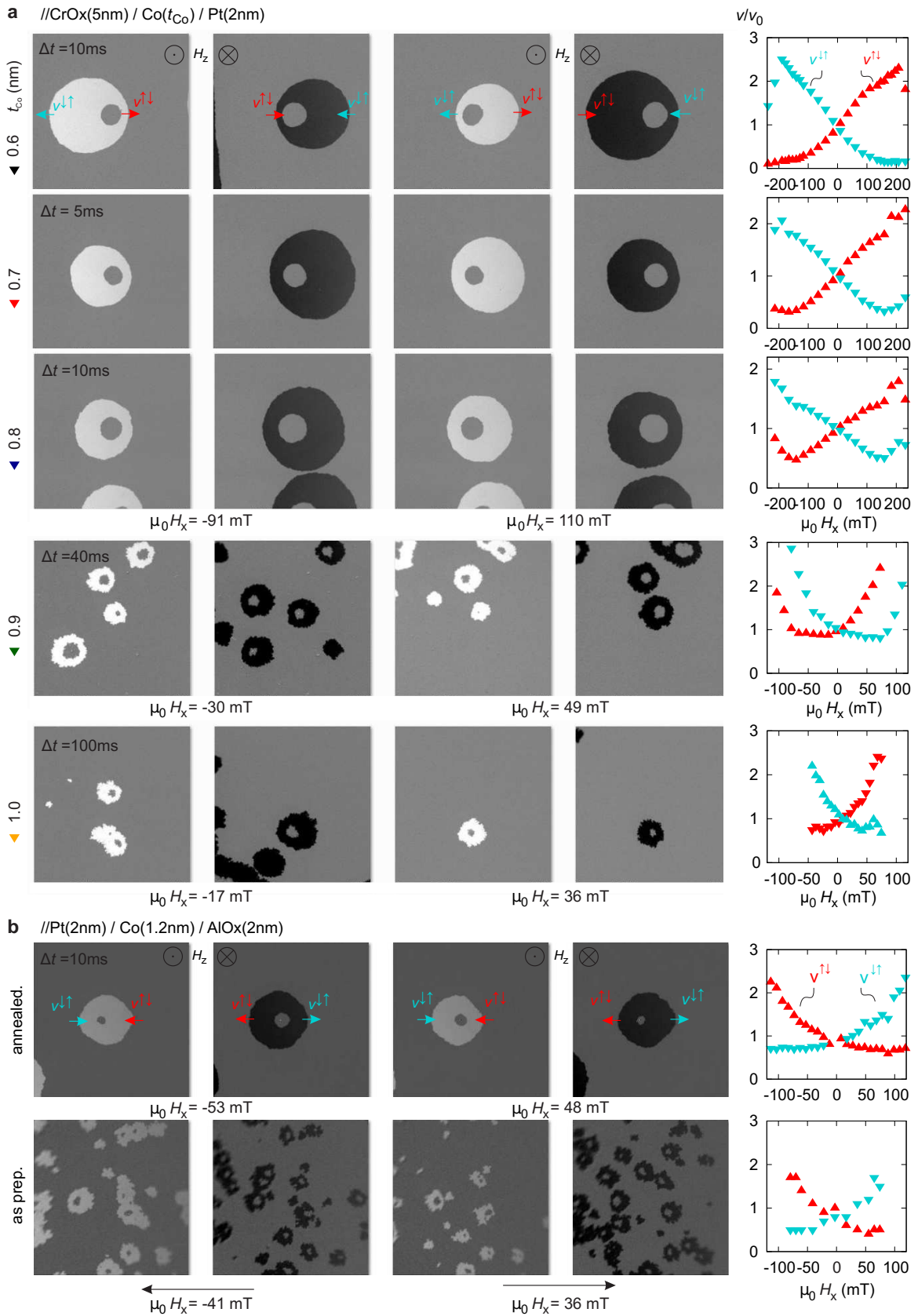


FIGURE 4.5: Caption next page.

FIGURE 4.5: Field-driven asymmetric domain expansion in //CrOx(5)/Co(t_{Co})/Pt(2) and //Pt(2)/Co(1.2)/AlOx(2) trilayers. The differential Kerr microscopy images taken from the initial and final state before and after a H_z -pulse in combination with an applied H_x -field show an asymmetric distortion. The DW creep velocity around the circumference of the domain is altered according to the relative orientation of the external field H_x and the DMI-field H_{DM} in the DW. The DW velocities of $\uparrow\downarrow$ and $\downarrow\uparrow$ DWs moving in the anti-/parallel alignment of H_{DM} and H_x are plotted as function of H_x .

in the DW (Eq. (2.17)). The sign of H_{DM} is given by the DW magnetization component along the DW normal. Assuming all DW segments around the circumference of the domain obtain the same chirality due to a sufficiently large DMI, H_{DM} homogeneously points out-/inwards with respect to the center of the domain. The DW creep velocities around the circumference of the domain are altered according to the relative orientation of H_x and H_{DM} . Hence the largest asymmetry is observed for the anti-/parallel alignment of both fields ($H_x \parallel H_{DM}$). For the perpendicular field configuration ($H_x \perp H_{DM}$), v remains fairly unchanged at low H_x with respect to the creep motion properties observed at $H_x = 0$ mT. The asymmetry is expected to invert for both magnetization and H_x reversal.

By evaluating the DW creep velocities v of $\uparrow\downarrow$ (+) and $\downarrow\uparrow$ (-) DWs moving along the axis of H_x , the $v^\pm(H_x)$ -curves are recorded (Fig. 4.5), that are analyzed in the following.

The quasistatic modification of the DW energy by the H_{DM} and H_x can be accounted for by the introduction of $\zeta = \zeta_0 [\sigma^\pm(H_x, H_{DM})/\sigma_0]^\mu$ in the creep law [134, 135], Eq. (4.4), with $\zeta_0 = \zeta(H_x = 0)$. The DW energy $\sigma(H_x, H_{DM})$ in the presence of both fields is reduced from the Bloch wall energy $\sigma_0 = 4\sqrt{A K_0}$ to the following ratio

$$\frac{\sigma^\pm(H_x, H_z)}{\sigma_0} = 1 - \frac{\pi^2 \Delta M_S^2}{8 N_x K_D \sigma_0} \mu_0^2 (\pm H_x + H_{DM})^2 \quad (4.6)$$

with the shape anisotropy energy scaled by the demagnetization factor $N_x = 4 \ln(2) t_{Co}/\Delta$ of the DW. This expression is valid as long as the field combination of $|H_x + H_{DM}|$ is smaller than the transition field from Bloch to Néel-Wall $H_{B \rightarrow N} = \frac{2}{\pi} N_x M_S$. It is further assumed, that the pinning parameters ξ and δ entering the quantity ζ_0 , Eq. (4.5), are independent of H_x [134].

For DWs segments situated in an (anti-)parallel (H_x, H_{DM})-field configuration one can write the following system of equations

$$\begin{cases} \ln v^+ = \ln v_0 - \zeta_0 \frac{\sigma^+(H_x, H_{DM})}{\sigma_0} \\ \ln v^- = \ln v_0 - \zeta_0 \frac{\sigma^-(H_x, H_{DM})}{\sigma_0} \end{cases} \quad (4.7)$$

In Eq. (4.7) the creep parameter $\ln v_0$, that can be determined less accurately due to extrapolation (sec. 4.2.1), is eliminated, which leads to the following expression

$$\ln\left(\frac{v^+}{v^-}\right) \frac{(\mu_0 H_z)^{1/4}}{\zeta_0} = \left(\frac{\sigma^+(H_x, H_{DM})}{\sigma_0}\right)^{1/4} - \left(\frac{\sigma^-(H_x, H_{DM})}{\sigma_0}\right)^{1/4} \quad (4.8)$$

Eq. (4.8) can be solved numerically for H_{DM} . As shown in Fig. 4.6 the dimensionless values of left and right side of Eq. (4.8) are situated on the diagonal for a correctly adjusted H_{DM} . All points that are deviating from the plot diagonal are not captured by the assumption of the model of sufficiently small H_x (i.e. the factor $\sqrt{1 - (H_x/H_K)^2} \approx 1$ [139]) and have to be omitted for the analysis.

With the following expansion that is valid when DW energies are only slightly changed by the total effective field

$$\left(\frac{\sigma^\pm(H_x, H_z)}{\sigma_0}\right)^{1/4} = 1 - \frac{1}{4} \frac{\pi^2 \Delta M_S^2}{8 N_x K_D \sigma_0} \mu_0^2 (H_x^2 + H_{DM}^2 \pm 2 H_x H_{DM}), \quad (4.9)$$

an analytical relation between H_{DM} and the velocity ratio $(v^+/v^-)(H_x, H_z)$ in applied fields can be derived from Eq. (4.8), that reads

$$\mu_0 H_{DM} = \frac{8 N_x K_D \sigma_0}{\mu_0 H_x \pi^2 \Delta M_S^2} \ln\left(\frac{v^+}{v^-}\right) \frac{(\mu_0 H_z)^{1/4}}{\zeta_0}. \quad (4.10)$$

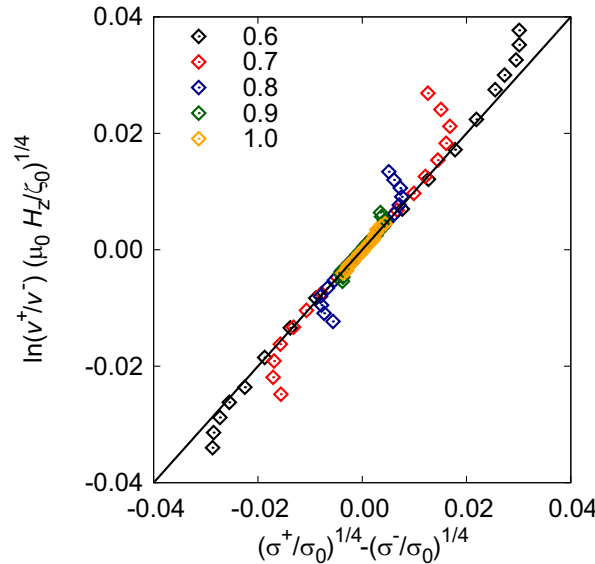


FIGURE 4.6: Dimensionless plot of left and right side of equation (4.8) relating the experimentally determined velocity ratio to the calculated DMI-induced DW energy reduction. With the correctly adjusted free parameter H_{DM} the data points are situated on the plot diagonal. The deviations from the diagonal obtained at larger fields mark the valid data range for the low field analysis.

Note, that the creep parameter ζ_0 depends on the exchange constant A (and all the other micromagnetic and microstructural parameters), as formulated in Eq. (4.5). Here, ζ_0 is directly and independently determined from the experiments in the perpendicular field H_x ($H_x = 0$), as described in sec. 4.2.1. Inserting this parameter now in expressions (4.10) and (4.11) yields the DMI strength from the second set of experiments with $H_x \neq 0$, but small. Eq. (4.10) can then be rescaled to the DMI strength using Eq. (2.17)

$$D_S = \frac{64 \ln(2)}{\pi^2} \ln \left(\frac{v^+(H_x, H_z)}{v^-(H_x, H_z)} \right) \frac{(\mu_0 H_z)^{1/4}}{\zeta_0 H_x} M_S K_{\text{eff}} \quad (4.11)$$

With this relation the interface-induced DMI constant can be directly calculated from the logarithmic asymmetry ratio of the DW-velocities $\ln(v^+/v^-)$ obtained at one field combination of H_x and H_z , the creep parameter ζ_0 and the two elementary magnetic parameters M_S and K_{eff} . It is emphasized that this expression does not explicitly depend on the exchange parameter A and is applicable only for small H_x .

In most of the previous reports [134, 136, 139, 168] it is assumed, that the minimum occurring in $v(H_x)$ -curves marks the position where the external field cancels the DMI field. In an approximative approach and only for a limited number of cases H_{DM} can then be directly read from a usually broad minimum. This serves as a direct and fast, but only crude measure of H_{DM} considering the typically observed data sets, as e.g. shown in Fig. 4.5.

The $v(H_x)$ minimum is usually found in field ranges where the magnetization within the domains is starting to get tilted (i.e. $\sqrt{1 - (H_x/H_K)^2} \ll 1$ [139]). This alters the DW energy

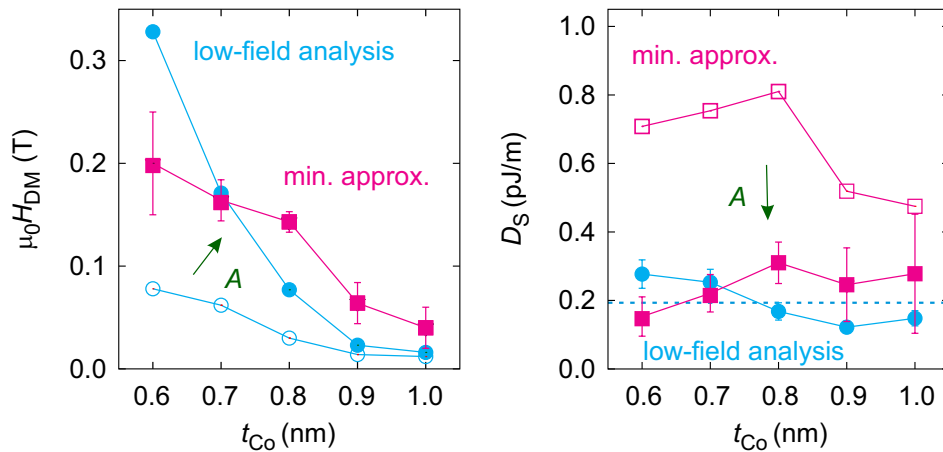


FIGURE 4.7: (a) DMI fields H_{DM} and (b) thickness-normalized DMI strength D_S as function of the cobalt thickness t_{Co} obtained from the minimum approximation and the developed low field analysis. The impact on the results is indicated by the green arrow that shifts the values calculated with the bulk- A (unfilled symbols) to those with the correct A (filled symbols) determined from the size of magnetic bubble domains.

by essentially changing the demagnetization factor of the wall and in turn also its mobility. Hence the minimum position cannot be simply identified with H_{DM} . This becomes increasingly important for thicker films where the anisotropy field is smaller and consequently leads to distortions of the $v(H_x)$ -curves (see Fig. 4.5).

Furthermore, the DMI field, Eq. (2.17), is a function of all micromagnetic parameters including the saturation magnetization M_S , anisotropy energy K_{eff} , exchange parameter A and DMI strength D_S . The rescaling to the DMI constant D_S requires a precise knowledge of all these parameters. As A is difficult to determine, usually the bulk value ($A^b=16$ pJ/m for cobalt) is assumed.

In the following it will be discussed, how the assumption of the bulk exchange parameter A^b can distort the results of the DMI field H_{DM} and the DMI strength D_S for the studied //CrOx/Co(t_{Co})/Pt samples series. As shown later, see sec. 4.3 on the quantification of the exchange constant, the true parameter in these films is markedly reduced. When using the bulk A in the analysis, the curves of the DMI field H_{DM} and the DMI strength D_S obtained from the minimum approximation and the low field analysis derived in this work are not matching, as shown in Fig. 4.7. The experimentally obtained significant reduction of A corrects the deviation between the differently determined D_S values. The DMI constants calculated from the minimum approximation of H_{DM} with the bulk A are clearly overestimated, and are shifted towards the results of the A -independent low-field analysis, when the correct exchange parameters are inserted (Fig. 4.7b). The DMI fields of the low-field analysis are underestimated when considering the bulk A and are shifted towards the results of the minimum approximation (Fig. 4.7a). Despite the A -correction the non-matching trends of H_{DM} of both methods indicates the approximative nature of the minimum approach. Within the errorbars only one matching result is obtained for $t_{Co} = 0.7$ nm.

Recently doubts about the commonly applied quantification methods for the DMI have been raised [139, 141], as the results from the asymmetric magnon dispersion and various quasistatic approaches (sec. 2.3.4) yield widely differing values of D_S . The presented results exemplify one important reason, as the used approaches so far have been unable to determine D_S and the crucial important exchange constant A independently.

The here presented alternative low-field analysis of the field-induced DW velocity asymmetry offers a twofold clarification for the ambiguities of previous results. Firstly one has to be aware of the multi-fold field effects on the DW mobility in different field regions, that can be easily avoided in the low-field approximation. And secondly, the relevance of every single micromagnetic parameter for the calculation and rescaling of quantities has to be strictly considered.

It was further proposed to ascribe the asymmetry of the domain expansion in the picture of

a dissipation effect attributed to chiral damping [154]. According to this idea the DW velocity is inversely proportional to the damping of the system. Depending on the DW chirality the damping is either enhanced or diminished by $\alpha_c l_{\text{ex}} (\mathbf{m}_{\text{ip}} \cdot \nabla m_z)$, with the exchange length l_{ex} and the DW magnetization component \mathbf{m}_{ip} perpendicular to the film normal. In contrast to the previously presented approach the attempt frequency f_0 in the creep parameter v_0 , Eq. (4.5), is modified by the DMI induced chiral damping, while the ζ is only affected by the hard axis field. According to Ref. [154], this results in a entirely different qualitative trend of the $v(H_x)$ -curves. Contrary to the observation in the here studied samples, no shift along the field axis of this curve is predicted in this model. This precludes the interpretation of the data in terms of the chiral damping.

4.2.3 Winding pair stability

In the regime of low creep velocities 360° DWs or so called *winding pairs* [41, 114] appear as shown in Fig. 4.8. After a DW eventually gets strongly pinned at a point-like defect the separated DW segments can wind up provided that both have an identical sense of rotation within the wall, i.e. the DW chirality is set by a sufficiently large DMI. A winding pair can then also be formed where two growing domains meet. This results in Voronoi-like pattern [41] that is formed by winding pairs parallel and perpendicular to the creep motion of domains respectively. The typical length of winding pairs in //CrOx/Co(t_{Co})/Pt trilayers decreases with increasing t_{Co} (Fig. 4.8). It is concluded that with the decreasing effective DMI constants at larger t_{Co} , the chirality selection mechanism becomes less pronounced.

It was recently proposed [41], that the stability of these winding pairs may also be used for the DMI quantification. By mapping the switching field H_{sw} dependence on the maximum saturation field H_{max} , the annihilation field H_{an} of winding pairs can be determined (Fig. 4.9a) above which they can no longer act as nucleation sites for the magnetization reversal process. The total width of winding pairs can be estimated from the chiral modulation length L_D ,

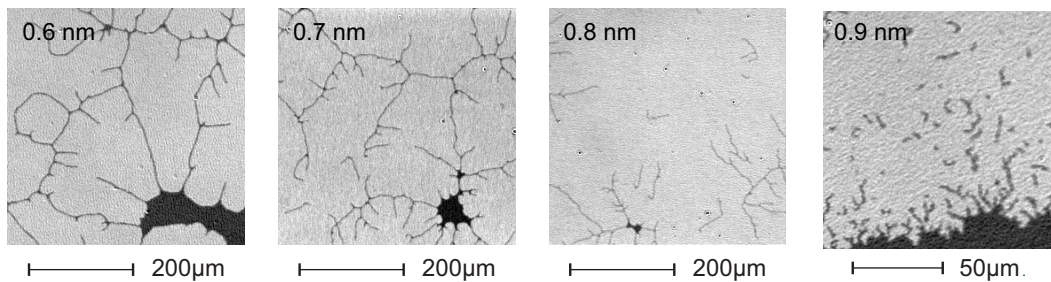


FIGURE 4.8: Winding pairs in //CrOx/Co(t_{Co})/Pt trilayers indicate the presence of homochiral DWs induced by a sufficiently strong interface-induced DMI. With the decreasing effective DMI at larger t_{Co} the chirality selection mechanism might be less pronounced resulting in overall shorter winding pairs.

TABLE 4.1: The effective interface-induced DMI constant $|D_{\text{eff}}^{\text{WPA}}|$ deduced from the winding pair annihilation field H_{an} in //CrOx/Co(t_{Co})/Pt trilayers.

t_{Co}	(nm)	0.6	0.7	0.8	0.8	1.0
$\mu_0 H_{\text{an}}$	(mT)	50	80	60	100	150
$ D_{\text{eff}}^{\text{WPA}} $	(mJ/m ²)	0.55	0.69	0.44	0.61	0.89

Eq. (2.18). With a conservative estimate of $L_{\text{D}} = 16 \text{ pJ m}^{-1} / 0.2 \text{ pJ m}^{-2} = 80 \text{ nm}$, the Kerr-microscopy has to be discarded as measurement technique for the purpose of winding pair detection. In this study the precise zero-offset AHE measurements [169] were used instead, assuming the presence of winding pairs despite visual proof.

The measured $H_{\text{sw}}(H_{\text{max}})$ dependency displays two regimes where H_{sw} linearly increases until a constant level at the value of the coercive field H_{c} is reached. In contrast to Ref. [41] the second critical field H_{an} is attributed to the full annihilation of the winding pairs.

The relation between H_{an} and the DMI constant can be determined from micromagnetic

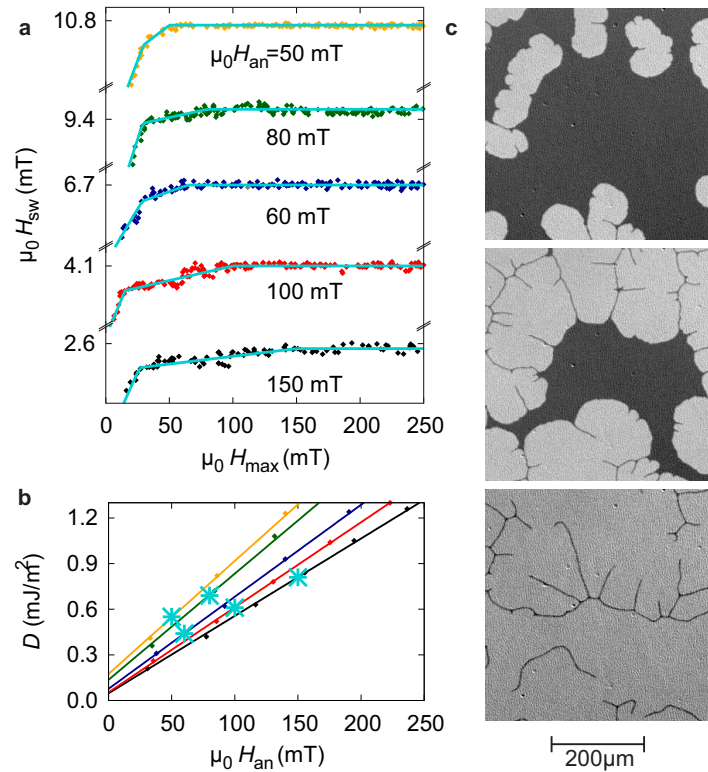


FIGURE 4.9: **(a)** Switching field H_{sw} dependence on the maximum saturation field H_{max} with the winding pair annihilation field H_{an} . **(b)** The relation of the measured H_{an} to the DMI constant is obtained from micromagnetic simulation using the measured M_{S} and K_{eff} parameters and the cobalt bulk exchange parameter $A = 16 \text{ pJ/m}$. **(c)** Winding pair formation in a //CrOx/Co(0.6)/Pt trilayer during the field-driven DW creep motion in a constant field of 1 mT visualized by Kerr microscopy at different times.

simulations (see Appendix A.2). Following Ref. [41], the initial state of a winding pair is prepared by a micromagnetically relaxed up-down-up domain configuration employing periodic boundary conditions along the direction of the winding pair. It is then exposed to a gradually increasing magnetic field until it eventually collapses at a field that marks H_{an} . By the variation of the DMI constants in the simulations a linear dependency of H_{an} on D_{eff} is revealed, from which the DMI constants for the experimentally determined H_{an} are interpolated (Tab. 4.1).

Although verifying the correct order of magnitude of the effective DMI strength, the results of this approach are questionable. The micromagnetic model evaluates the stability of DMI kinks under the assumption of bulk exchange in the systems. As stated in sec. 2.3.2 the relation of DMI kinks and winding pair in terms of their stabilization mechanism and transmutation is undefined. Furthermore, the whole annihilation process lacks visual proof, and hence blindly assigns the observed critical field to the disappearance of DMI kinks. The required refinements of this approach are beyond the scope of this work.

4.3 Determination of the exchange parameter

The typical size of the homochiral magnetic objects allows for the determination of one unknown parameter of the micromagnetic parameter set, here the exchange parameter A . Recently a wide diameter range from around 50 nm [13] up to 2 μm [3] for chiral magnetic objects was reported in these systems with fairly comparable DMI strength of the order of $D_S = 1 \text{ pJ m}^{-1}$. If these objects were to be identified as chiral skyrmions stabilized by the DMI, a wide spread of the exchange parameter A would be required to cover the whole range of object diameters according to the chiral modulation length L_D , Eq. (2.18). This eventually leads to unrealistically large values of the exchange constant as e.g. 27.5 pJ m^{-1} [53], which is above the exchange constant of bulk cobalt. Therefore, it is mandatory to distinguish between chiral magnetic bubbles and skyrmions in order to apply the suitable theoretical framework, when determining the complete set of micromagnetic parameters for the system.

4.3.1 Generation of circular magnetic objects

Circular chiral magnetic objects may be generated in the scheme of Jiang et al. [3] or by applying a demagnetization routine. In the prepared microstripes a coherent current-induced motion of two DWs enclosing a domain is observed upon the application of current pulses to the magnetic stripe (see Fig. 4.10a and b). The DWs move against the direction of the electron flow, and consequently the DW shift changes sign with the reversal of the current direction. The constriction of the microstripe causes inhomogeneities of the current density

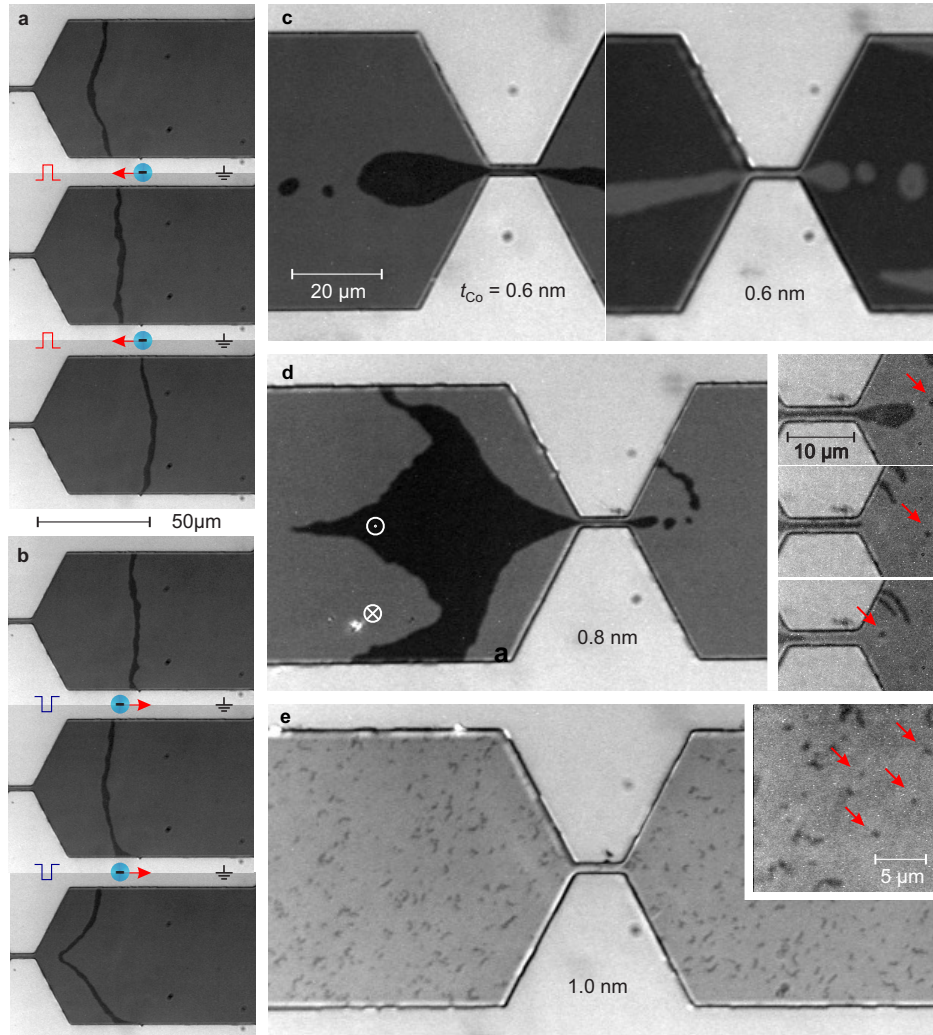


FIGURE 4.10: Current induced DW motion in a $60 \mu\text{m}$ wide $//\text{CrOx}(5\text{nm})/\text{Co}(0.8\text{nm})/\text{Pt}(2\text{nm})$ channel. Both $\uparrow\downarrow$ and $\downarrow\uparrow$ DWs coherently move driven by spin-orbit torques against the electron motion direction with an average velocity of $50 \mu\text{m/s}$ at the chosen current density of $j = 5.62 \times 10^6 \text{ A/cm}^2$. The images are taken after application of positive (a) and negative (b) pulses of 40 ms length. The velocities vary across the width of the stripe due to the current density profile and are largest close to the constriction of the stripe. The creation of magnetic circular objects in the scheme of Jiang et al. [3] or by a demagnetization routine in $//\text{CrOx}/\text{Co}(t_{\text{Co}})/\text{Pt}$ trilayers with different cobalt layer thicknesses (c-e) indicated by red arrows. Different snapshots tracking the creation process of a the object are shown in panel (d).

which reflects in a distinct DW velocity profile across the microstripe width with a velocity maximum at the center of the stripe (see last image in Fig. 4.10b).

The current-induced DW motion is attributed to the action of spin-orbit torques [36, 37] on the DWs. It is required that the DWs are homochiral to enable a coherent motion of the object. Additionally, a DW magnetization component parallel to the current direction (i.e. Néel-like type wall) is needed in order to allow for the spin-orbit torques to efficiently induce DW propagation against the direction of electron motion. In the presence of DMI these DW properties are a natural consequence which also result in the formation of winding pairs (sec. 4.2.3).

Circular homochiral magnetic objects are generated due to the contraction of a domain channel in divergent currents during the expulsion from the constriction area, when additionally applying an easy axis field (H_z) to stabilize the created magnetic object (inset of Fig. 4.10d). The resulting objects sometimes are of arbitrary shape and usually shrink to circular objects of a typical diameter. Small alternating external magnetic fields can assist to reach this equilibrium state. Due to large pinning in the samples the objects are rather immobile when applying either magnetic field or current pulses.

In the samples with $t_{Co} \leq 0.9$ nm the strong pinning prevents an efficient current-induced motion. Instead a typical meander pattern of magnetic domains is observed. In these cases the circular objects were observed during the magnetization reversal as remainder of the continuously shrinking meander structures.

Considering the scaling of the characteristic diameter of the circular objects with the cobalt layer thickness one can identify them as magnetic bubble domains or skyrmions. The

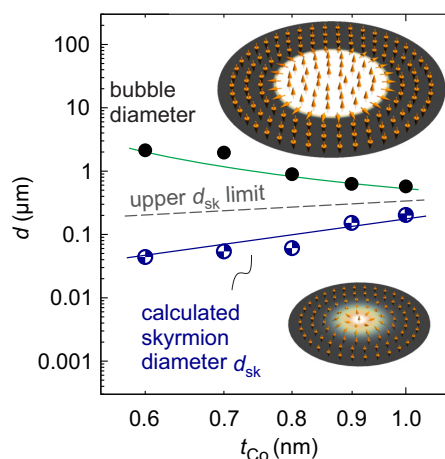


FIGURE 4.11: The diameter scaling the magnetic objects allows to distinguish between skyrmions and homochiral bubbles domains. An upper limit of d_{sy} can be obtained from simulations assuming the bulk exchange value. The calculated skyrmion diameter d_{sy} from the complete set micromagnetic parameters is plotted for comparison.

individual scaling behaviors are discussed in the following assuming a constant exchange parameter for simplicity.

The diameter of bubbles is related to the ratio λ_c of the DW energy and the shape anisotropy (sec. 4.3.2). In the case of the bubble collapse, this ratio λ_c is determined by the stability criterion, which is monotonically increasing with the collapse diameter. The shape anisotropy, Eq. (2.12b), is a quadratic function of the saturation magnetization, which decreases almost linearly with decreasing t_{C0} in the investigated samples. Therefore $\lambda_c \propto t_{C0}^{-2}$ decreases with increasing t_{C0} . Hence, cylindrical bubble domains stabilized by the dipolar stray fields are expected to shrink in size with increasing layer thickness, i.e. their size should be inversely proportional to t_{C0} .

On the other hand the skyrmion diameter is approximately proportional to the chiral modulation length L_D , Eq. (2.18) scaling with the ratio of ferromagnetic A to asymmetric D_{eff} exchange constant. For decreasing D_{eff} with increasing t_{C0} an increase of the skyrmion diameter is expected at constant A . Chiral skyrmions are therefore expected to become larger in thicker films.

The opposing trends allow to identify the character of the observed circular objects. Quantitative estimates then can corroborated the identification, as bubbles are generally much larger than skyrmions under reasonable assumptions about the materials parameters.

The observed magnetic objects have diameters of the order of $1 \mu\text{m}$. As shown in Fig. 4.11 their diameters follow the inversely proportional thickness trend violating the skyrmion diameter scaling $\propto (D_S t_{C0})^{-1}$. Hence, objects are identified as homochiral bubble domains and the bubble domain theory is employed to determine the remaining unknown magnetic material parameter A from the bubble size (sec. 4.3.2). Only if the skyrmion scaling is observed, the exchange parameter can be evaluated in the framework of skyrmion theory. Micromagnetic simulations (Appendix A.1) with known M_S , K_{eff} and D_S can be performed to determine the exchange parameter by only varying A until the resulting diameter matches the experimentally observed skyrmion size.

In principle a homochiral bubble should be convertible to skyrmion by constriction. Vice versa the expansion of a skyrmion could generate a bubble domain. In the experiments the nucleation of a reverse domain from the collapse site of a bubble domain in opposite field was not observed. This infers that at least one of transformations from homochiral bubbles into skyrmions or vice versa is unlikely to appear in the systems in the chosen experimental condition. Standard Kerr microscopy imaging does not provide the magnification for a visual documentation of this processes given the estimated diameter range for the skyrmions. Together with the hitherto unclarified energetics of the transmutation process between the two objects this topic remains unsettled.

4.3.2 Homochiral magnetic bubble domains

According to magnetic bubble domain theory [114, 115] valid for $Q = K_I/K_D > 1.5$ the collapse diameter D_{bc} can be derived from the ratio of the DW energy σ_{DW} to the shape anisotropy K_D , Eq. (2.12b), satisfying the condition

$$\lambda_c = \sigma_{DW}/(2 K_D t_{Co}) = S_{bc}(d) = \frac{2}{\pi} [d^2 (1 - E(u^2)/u) + u K(u^2)] \quad (4.12)$$

with the complete elliptic integrals as function of $u^2 = d^2/(1 + d^2)$

$$E(u) = \int_0^{\pi/2} \sqrt{1 - u \sin^2 \alpha} d\alpha, \quad K(u) = \int_0^{\pi/2} d\alpha / \sqrt{1 - u \sin^2 \alpha}. \quad (4.13)$$

Please note that the reduced diameter $d = D/t_{Co}$ is to be employed.

In contrast to the classical bubble domain theory [114, 115], it is pointed out, that in the presence of DMI the DW energy reads $\sigma_{DW} = 4\sqrt{A K_{eff}} - \pi D_S t_{Co}$. Solving Eq. (4.12) for the exchange constant A as the only unknown remaining parameter yields the following expression

$$A = \frac{t_{Co}^2}{16 K_{eff}} [\mu_0 M_S^2 S_{bc}(d_{bc}) + \pi D_S]^2. \quad (4.14)$$

Furthermore the correct experimental conditions for the bubble collapse regime can be verified by calculating the theoretically expected collapse field $H_{bc} = M_S t_{Co} [F(d_{bc}) - S_{bc}(d_{bc})]/d_{bc}$ from the condition of the force function

$$F(d) = -\frac{2}{\pi} d^2 [1 - E(u^2)/u] = \lambda_c + \frac{H_{bc}}{M_S} d \quad (4.15)$$

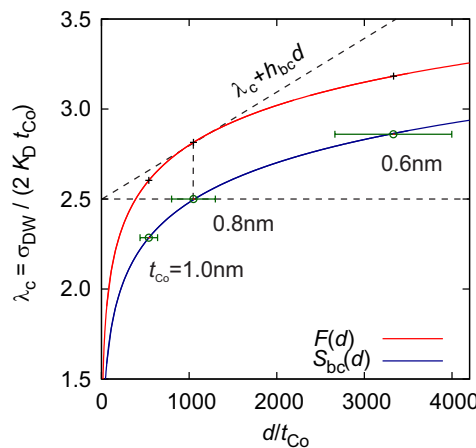


FIGURE 4.12: Diagram for the derivation of the stability of magnetic bubble domains. Plotted are the force function $F(d)$ and stability criterion $S_{bc}(d)$ according to Eq. (4.15) and (4.12). For a known bubble collapse diameter the exchange parameter A can be calculated from λ_c . The collapse field $\mu_0 H_{bc}$ can be read from the slope of the tangent at $F(d_{bc})$.

TABLE 4.2: The measured collapse diameter D_{bc} of magnetic bubble domains in the experimentally applied field $\mu_0 H_{ext}$ and the calculated force function $F(d_{bc})$ and the stability criterion for the bubble collapse $S_{bc}(d_{bc})$ from which the bubble collapse field $\mu_0 H_{bc}$ and the exchange parameter A , Eq. (eq:Aquant), can be calculated.

t_{Co} (nm)	D_{bc} (μm)	$\mu_0 H_{ext}$ (mT)	S_{bc}	F_{bc}	$\mu_0 H_{bc}$ (mT)
0.6	2.0 ± 0.4	0.06	2.864	3.182	0.14
0.7	1.84 ± 0.4	-	2.789		-
0.8	0.84 ± 0.20	0.29	2.496	2.815	0.52
0.9	0.59 ± 0.20	-	2.347		-
1.0	0.54 ± 0.10	5.42	2.285	2.603	1.10

which is equivalent to the slope $h_{bc} = H_{bc}/M_S$ of the tangent at $F(d_{bc})$ as shown in Fig.4.12a. The estimated fields $\mu_0 H_{bc}$ are of the order of the applied fields revealing that the experimental fields were just slightly below the theoretical collapse field. Note that in case of the thickest sample ($Q = 1.25 < 1.5$) the bubble domains are far more stable than theoretically expected. This indicates a rather important role of pinning that was neglected throughout the analysis.

4.4 Results

The micromagnetic parameters of the prepared samples series of //CrOxCo(t_{Co})/Pt as sketched in Fig. 4.13a are quantified as described in the previous sections. The technological advantageous implementation of the stack inversion imposes the auxiliary necessity of a global characterization of the system and its intrinsic magnetic parameters, that are strongly impacted not only in the ultra-thin film limit but also by details of the preparation in terms of the microstructural properties of the samples (see sec. 3.2).

In the cobalt thickness range between 0.6 and 1.0 nm the films have perpendicular magnetic anisotropy (PMA). The field-driven magnetization reversal is induced by domain nucleation followed by DW propagation. For fields along the easy axis of magnetization a square shaped hysteresis loop with full remanence and sharp switching is obtained. For fields perpendicular to the easy axis direction, the magnetization is continuously rotated around the anisotropy axis showing no hysteric behavior (Fig. 4.13b).

Fig. 4.13c shows, that with decreasing t_{Co} the saturation magnetization M_S significantly deviates from the cobalt bulk value of $M_S^b = 1.48$ MA/m. Consequently, the shape anisotropy K_D has a decreasing trend. As the anisotropy field H_K strongly increases towards smaller t_{Co} the effective anisotropy energy constant K_{eff} also increases (Fig. 4.13d). The anisotropy energy constant K_0 of the unidirectional PMA induced by both the Co/Pt and the Co/CrOx interface is fairly constant for all samples.

The two observations of winding pair formation and the coherent current-induced DW motion clearly indicate that the DWs in the sample are of a homochiral Néel-type. It is understood, that this specific DW structure can only be induced by a sufficiently strong interface-induced DMI in the samples. As the dynamic properties are determined by the details of its structure, the asymmetric features observed in DW motion studies can be related to the DMI. Based on the theory of field-driven DW creep motion, in this work a revised analysis method was derived, that allows the unambiguous determination of the interface-induced DMI magnitude D_S . A fairly constant value of the interface-induced DMI constant is found for all t_{Co} around an averaged of $D_S = -0.20 \pm 0.09$ pJ/m (Fig. 4.13g). For the //Pt/Co/AlOx reference samples a DMI constant of $+0.52 \pm 0.32$ pJ/m was determined. When annealing the reference sample at 200 °C for 15 min, the DMI constant insignificantly increases to $+0.69 \pm 0.22$ pJ/m. Considering the error margin a beneficial effect on the DMI strength by the thermal treatment can not be concluded.

However, the effective DMI magnitude is not exceeding the critical DMI value necessary to

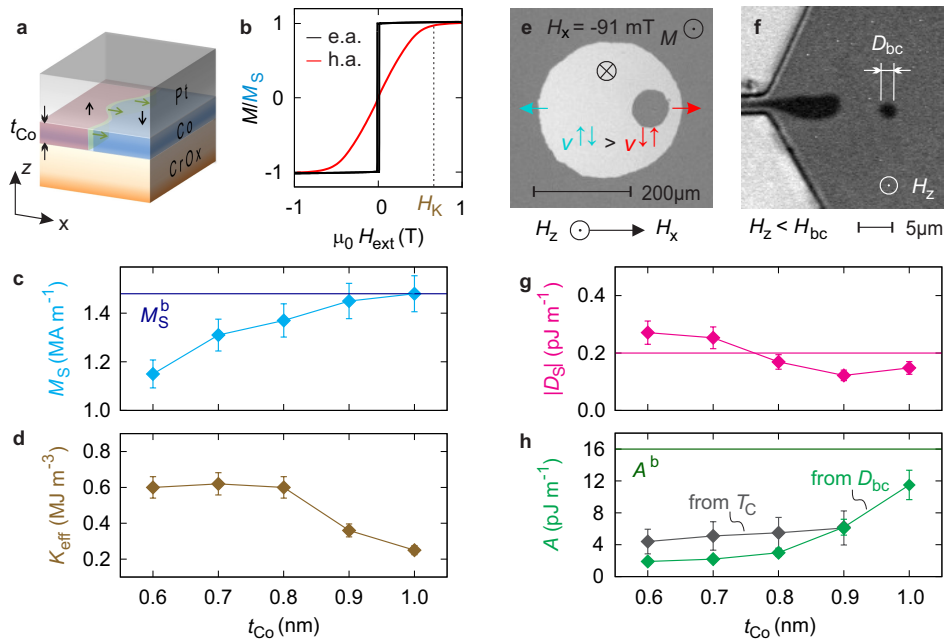


FIGURE 4.13: Full micromagnetic characterization of //CrOx/Co(t_{Co})/Pt trilayers with varying cobalt layer thickness t_{Co} . **(a)** Sketch of the trilayer stack and **(b)** the easy (z) and hard (x) axis hysteresis loops of the magnetization obtained by anomalous Hall magnetometry normalized to the saturation magnetization M_S . A significant dependence of the micromagnetic parameters on t_{Co} is observed, including **(c)** M_S and **(d)** the anisotropy energy constant K_{eff} . **(g)** The interface-induced Dzyaloshinskii-Moriya interaction constant D_S quantified from the asymmetric domain growth **(e)** is fairly equal in all samples as expected from the interface nature of the effect. **(h)** The exchange parameter A calculated from the bubble collapse diameter D_{bc} **(f)** is substantially reduced towards thin cobalt layers. The sizable deviation from the bulk value A^b is supported by the approximate estimation of A from the Curie temperatures T_C .

TABLE 4.3: Dependence of magnetic parameters of //CrOx/Co(t_{Co})/Pt samples on the cobalt layer thickness t_{Co} (saturation magnetization M_{S} , anisotropy field H_{K} , effective anisotropy constant K_{eff} , creep parameter ζ_0 , coercive field H_{c} , Curie temperature T_{C} , exchange parameter A , domain wall width Δ and the cobalt thickness normalized DMI constants D_{S}) and the calculated skyrmion diameter d_{sk} .

t_{Co}	(nm)	0.6	0.7	0.8	0.9	1.0
M_{S}	(MA/m)	1.15	1.31	1.37	1.45	1.48
H_{K}	(MA/m)	0.84	0.76	0.70	0.40	0.27
K_{eff}	(MJ/m ³)	0.60	0.62	0.60	0.36	0.25
K_{D}	(MJ/m ³)	0.83	1.07	1.19	1.32	1.38
K_0	(MJ/m ³)	1.43	1.70	1.79	1.68	1.62
ζ_0	(mT) ^{-1/4}	25	31	40	78	87
$\mu_0 H_{\text{c}}$	(mT)	2.6	4.1	6.7	9.4	10.8
T_{C}	(K)	385	440	479	530	-
D_{S}	(pJ/m)	-0.27	-0.25	-0.17	-0.12	-0.15
D_{eff}	(mJ/m ²)	-0.46	-0.36	-0.21	-0.14	-0.15
A	(pJ/m)	1.9	2.9	3.0	7.3	11.5
Δ	(nm)	1.7	2.2	2.2	4.5	6.8
d_{sk}	(nm)	44	54	61	152	203

support states of helical and skyrmion lattices. Nevertheless, homochiral circular magnetic objects of a characteristic size can be generated in the samples. As the exchange parameter is the only remaining unknown of the micromagnetic parameter set, it can be deduced from the object size. From the characteristic scaling dependence of the object diameter with respect to the cobalt layer thickness, it is inferred that the investigated systems support homochiral bubbles rather than skyrmions (sec. 4.3.1). Hence, the treatment of the objects in the suitable theoretical framework of magnetic bubble domain theory is implied, in which the exchange parameter A was deduced from the collapse diameter of homochiral magnetic bubble domains (sec. 4.3.2). A significant reduction of A from the cobalt bulk value of $A^b = 16$ pJ/m is revealed that strongest for small t_{Co} . The trend of the drastically diminished A in the studied trilayers as shown in Fig. 4.13h is supported by the approximative estimation of A from the extrapolated Curie temperatures T_{C} (sec. 4.1) by the relation $A(T_{\text{C}})/A^b = T_{\text{C}}/T_{\text{C}}^b$ with $T_{\text{C}}^b = 1394$ K.

With the knowledge of the full set of micromagnetic parameters the skyrmion diameters can be calculated (Appendix A.1) and are expected in a range of 40-200 nm.

Chapter 5

Magnetotransport measurements

5.1 Measurement setup

Typically angular-dependent measurements [20, 112] are used to assess angular footprints of the magnetoresistances (MR) and spin-orbit torque (SOT) effects (Sec. 2.2.2 and 2.2.3). The relative orientation of the current \mathbf{j} and magnetization direction $\hat{\mathbf{m}}(\mathbf{H}_{\text{ext}})$ is adjusted via the external magnetic field $\mathbf{H}_{\text{ext}}(\theta, \phi)$. The coordinate system used is defined in the following way (compare with Fig 5.1a). The sample normal, or equivalently the easy axis of magnetization is pointing in $\hat{\mathbf{z}}$ -direction, while the current direction is parallel to the $\hat{\mathbf{x}}$ -direction. The polar angle θ and azimuthal angle ϕ are measured with respect to $\hat{\mathbf{z}}$ and $\hat{\mathbf{x}}$ respectively. The external field $\mathbf{H}_{\text{ext}}(\theta, \phi)$ is only applied along the principal axes H_x , i.e. $\mathbf{H}_{\text{ext}}(\theta = \pi/2, \phi = 0)$, H_y and H_z achieving the sensitivity to the anisotropic, spin-Hall and linear MR effect respectively.

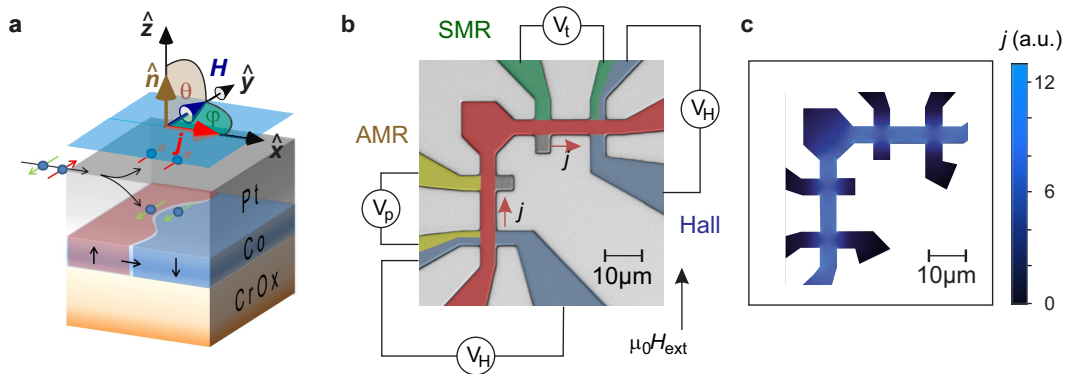


FIGURE 5.1: **(a)** Definition of the coordinate system used in the magnetoresistance measurements of the //CrOx/Co/Pt samples. **(b)** Sample layout for the simultaneous quantification of magnetoresistance effects (Hall, AMR, SMR) and the spin-orbit torques in asymmetrically sandwiched ferromagnetic thin films. The layout considers the minimization of current density inhomogeneities/asymmetries according to simulations **(c)** to avoid cross talk while providing large current densities.

In this work an approach is developed that avoids a goniometric stage by a suitable sample layout (see Fig. 5.1b) containing all relevant orthogonal vector arrangements of \mathbf{j} and $\hat{\mathbf{m}}(\mathbf{H}_{\text{ext}})$ for the quantification of the MR effects and SOT. Therefore the measurement can be performed in a straight-forward scheme using a conventional uni-axial electromagnet [170]. The prepared sample layout contains two orthogonal stripe segments with individual contact leads for a 4-point resistance measurement and two Hall crosses to measure longitudinal and transversal resistances respectively. When the sample is mounted with the field orthogonally applied to the plane normal and parallel to one of the stripe segments (see Fig. 5.1b) measurements of the anisotropic (AMR) and spin-Hall (SMR) magnetoresistance as well as the Hall voltage can simultaneously be performed. The harmonic analysis of the transversal resistance measured at two different Hall crosses is used to quantify the field-like ($\mathbf{j} \parallel \mathbf{H}_{\text{ext}}$) and anti-damping ($\mathbf{j} \perp \mathbf{H}_{\text{ext}}$) SOT as described in section 5.3.

Stripes of the width of about $4\mu\text{m}$ are used to provide large current densities up to the order of 10^7 A/cm^2 where reasonable signals of spin-orbit effects are expected. The layout design considers the minimization of current density inhomogeneities/asymmetries according to simulations performed in collaboration with T. Kosub (Fig. 5.1c), in order to avoid cross talk in between the transversal and longitudinal resistance channels.

5.2 Magnetoresistance effects

The measured differential voltage is normalized to the current as well as the stripe length L and cross section area $W t_{\text{cd}}$ yielding the resistivity ρ of the trilayer system. Scanning electron

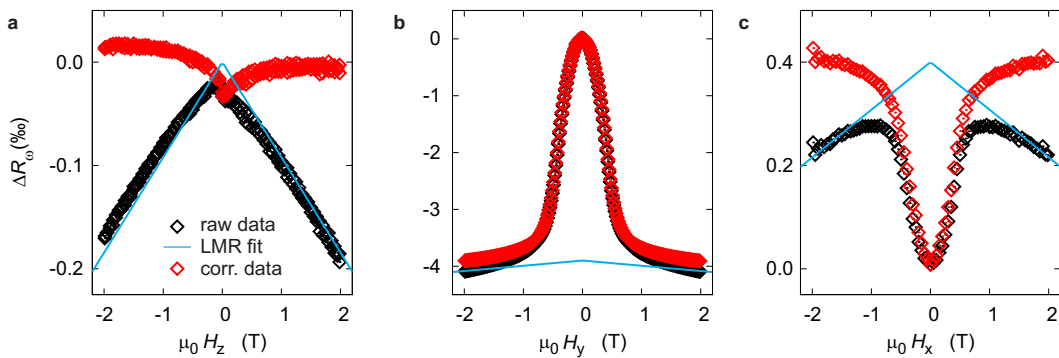


FIGURE 5.2: The longitudinal resistance changes ΔR_{ω} , measured in the three principal field, axes recover the (a) field-dependent negative linear magnetoresistance (LMR) and the magnetization dependent spin-Hall (SMR) and anisotropic (AMR) magnetoresistance (panel (b) and (c) respectively). The LMR is found in every field direction and has to be subtracted in order to evaluate the correct MR ratio. The magnetization-dependent resistances curves resemble a typical bell-shape that is given by the field-dependent in-plane magnetization component according to the hard axis hysteresis loop.

microscopy (SEM) was used to obtain the stripe dimensions W and L while the thickness of the conducting layer t_{cd} is assumed to be the sum of the nominal deposition thicknesses of the cobalt and platinum layers.

Considering the bulk resistivity of cobalt and platinum ($\rho_{Co} = 60 \text{ n}\Omega\text{m}$ and $\rho_{Pt} = 106 \text{ n}\Omega\text{m}$) respectively the expected stack resistivity can be estimated as follows

$$\rho_{tot} = \frac{\rho_{Co} \rho_{Pt} (t_{Co} + t_{Pt})}{\rho_{Co} t_{Pt} + \rho_{Pt} t_{Co}}. \quad (5.1)$$

In rough and/or intermixed bilayer this can only serve as an estimation of the order of magnitude of the resistivity. For better treatment the Fuchs/Sondheimer model [171] considering conductivity modifications occurring in the ultrathin film limit should be employed and modified according to the microstructural details of the interface, which was not in the scope of this work.

According to the hard axis loop (see section 4.1) the magnetization coherently rotates from the remanent saturation state $\theta = 0$ until it is fully aligned with the external field applied perpendicular to the easy axis direction. The quadratic first-order longitudinal MR effects resemble a bell-shaped field dependence, that is given by the field-dependent in-plane magnetization component according to the hard axis hysteresis loop (Fig. 4.1c). When applying the external field along \hat{x} or \hat{y} the a positive and negative resistance change is observed according to AMR and SMR effect respectively. Both curves are superimposed with a linear field-dependent negative magnetoresistance (LMR). The relative LMR magnitude can be measured in the easy axis configuration and is about half as large as the AMR at the maximum applied field of 2 T. To deduce the correct AMR and SMR ratio the LMR has to be subtracted from the signal in advance as shown in Fig. 5.2.

In a reference experiment the Pt layer thickness was increased in order to study the shunting behavior with respect to the AMR and SMR (see Fig. 5.3). The AMR requires the

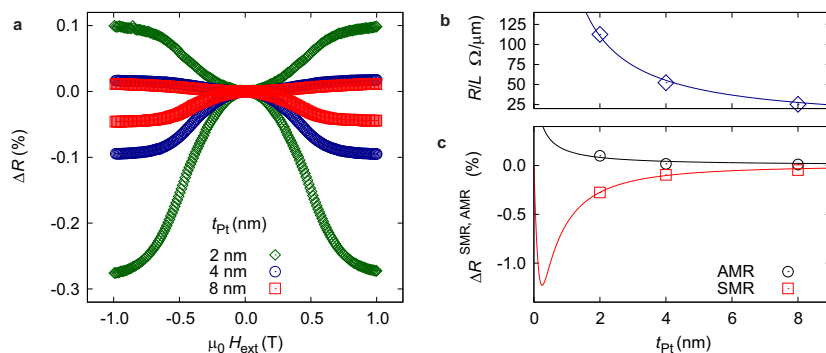


FIGURE 5.3: Shunting of the AMR and SMR by the platinum layer in //CrOx/Co/Pt(t_{Pt}) reference samples. The effect amplitude of AMR and SMR decreases with increasing t_{Pt} (a,c) while the the resistivity is dominated by the Pt layer (b).

direct interaction of valence electrons with localized moments. Any adjacent non-magnetic conducting layer reduces the AMR ratio according to its thickness and resistivity. The SMR ratio depends on the spin-Hall angle and the interaction volume fraction of the interaction zone of spin-polarized electrons with the magnetic localized moments which is very small due to rapid dephasing at interface. The spin-Hall angle is dependent on the Pt layer thickness following a sech-function with the spin diffusion length as the critical parameter, Eq. (2.3). Both effects are localized in the ferromagnet or its direct vicinity and are strongly shunted by thick Pt layers.

A further contribution to the magnetoresistance that is odd with respect to current or magnetization direction reversal is called the unidirectional spin-Hall magnetoresistance (USMR) [112]. The second harmonic signal of the longitudinal resistance with the magnetic field applied along the \hat{y} axis (Fig. 5.4a) almost resembles the hard axis hysteresis loop of the magnetization. Superimposed is a small signal contribution that is found in the second harmonic of the Hall resistance (Fig. 5.5b) hinting that despite the efforts there is some remaining crosstalk in between the different channels. The measure of the USMR $\Delta R_{2\omega}^{\text{USMR}}$ is defined as half the step height of the two saturation values. Due to the tiny cross talk only a negligible additional contribution is expected. The effect magnitude depends after a non-linear onset linearly on the current density (Fig. 5.4b). This supports the suggested interpretation [112] of the USMR effect as a GMR-like effect that comes about the interplay of the ferromagnetic layer with the spin accumulation layer formed at the interface due to the spin-Hall effect in platinum. As indicated by the sketches in Fig. 5.4a the spin accumulation layer forms for a given current direction what is known for the GMR effect as the fixed

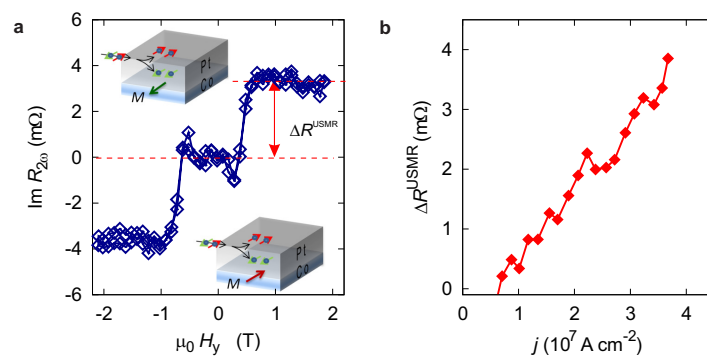


FIGURE 5.4: **(a)** The unidirectional SMR [112] in //CrOx(5nm)/Co(0.8nm)/Pt(2nm) is revealed in the imaginary part of second harmonic signal measured in SMR configuration. The interplay of the spin-polarized electrons accumulating at the interface to the ferromagnetic layer with the localized moments suggests a physical origin similar to the GMR-effect (indicated by the sketches). **(b)** The effect increases with the amount of spin-polarized electrons provided by the spin-Hall effect, i.e. with increasing current density .

layer. The ferromagnetic layer then acts as the free layer that is adjusted by external magnetic field. In states where the external field aligns the magnetization (anti-)parallel with respect to the polarization direction of the spin accumulation layer the maximum resistance change is achieved.

5.3 Spin-orbit torque quantification

The strength of a spin-orbit torque (SOT) is expressed by an effective magnetic field B_{eff} , that alters the nonlinear transversal Hall resistance i.e. its second harmonic signal. In external fields applied along \hat{x} or \hat{y} the corresponding effective fields of the anti-damping (AD) and field-like (FL) SOT are picked up respectively. As described in section 2.2.4 the expression for the fields simplifies in the absence of the PHE and can be directly calculated from the derivatives of the first and second harmonic signals of the transversal Hall resistance (Fig. 5.5a and b respectively)

$$B_{\text{eff}}^{\text{AD(FL)}} = -2 \left(\frac{\partial R_{2\omega}^H}{\partial B} \right) \bigg/ \left(\frac{\partial^2 R_{\omega}^H}{\partial B^2} \right) \bigg|_{B_{\text{ext}}=B_{x,(y)}}. \quad (5.2)$$

As the equation is valid for small θ -deviations the respective data parts were taken from the low field region for the analysis of the derivatives as indicated in the curves Fig. 5.5b. The slope of the second harmonic signal has a similar dependence on the current density as shown for the USMR in Fig. 5.4b. As the slope especially of the second harmonic signal is strongly susceptible to signal drifts the values of back and forth branch of the hysteresis are averaged. The effective field values directly translate to the respective torques per unit moment.

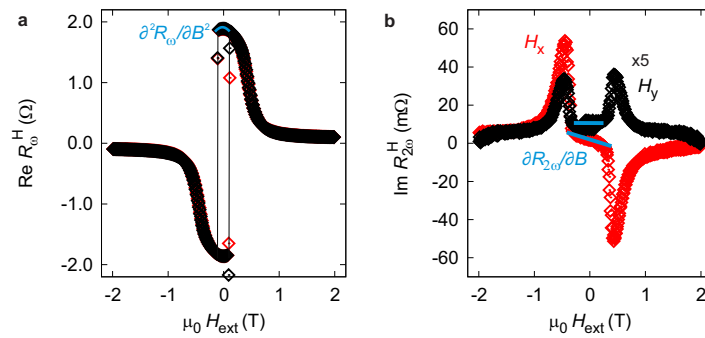


FIGURE 5.5: The (a) 1st and (b) 2nd harmonic signal of the transversal resistances for the external magnetic field applied along the \hat{x} (red) and \hat{y} (black) direction for a //CrOx(5nm)/Co(0.8nm)/Pt(2nm) trilayer. The effective fields induced by field-like and anti-damping-like spin-orbit torques are evaluated from the derivatives of the signals in the indicated field region according to Eq. (5.2).

5.4 Results

The results of the magnetotransport investigations of the //CrOx/Co(t_{Co})/Pt sample series described in the previous sections using a sample layout (Fig. 5.6a) for the simultaneous quantification of important spin-orbit effects are summarized in Tab. 5.1 and Fig. 5.6e-h as a function of the cobalt layer thickness t_{Co} .

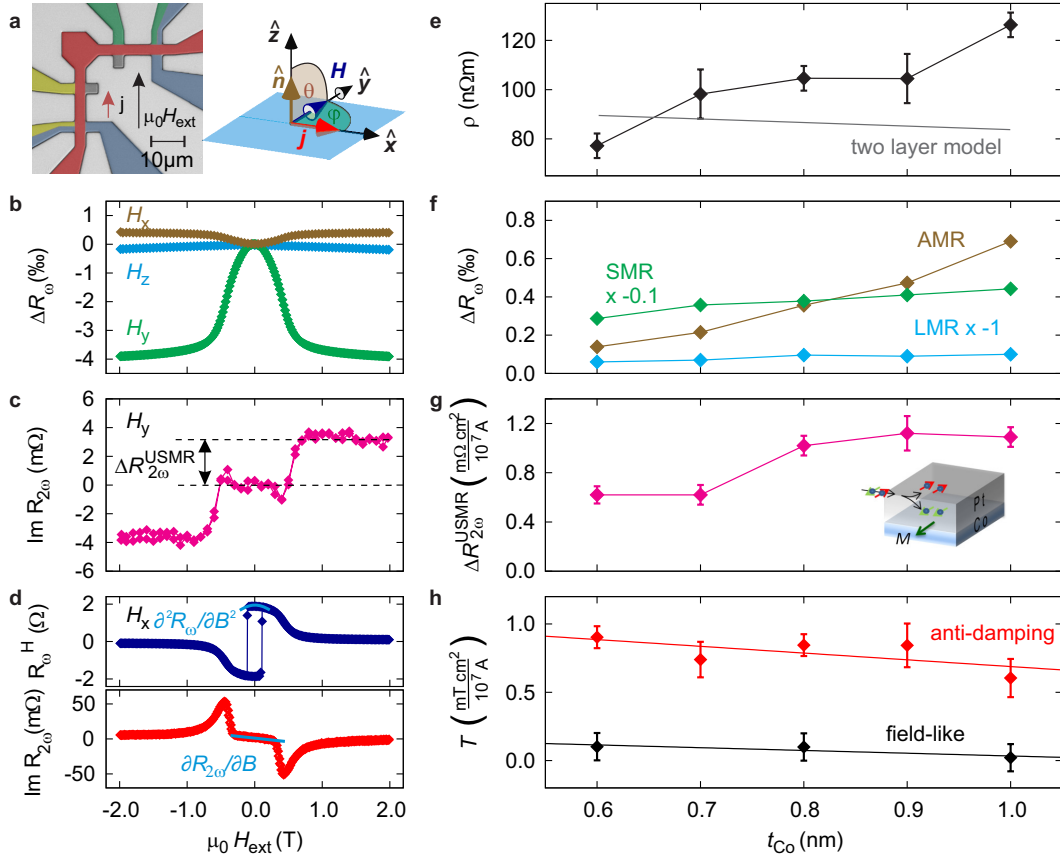


FIGURE 5.6: **(a)** Sample layout for the straight forward quantification of magnetoresistance effects and spin-orbit torques in //CrOx/Co(t_{Co})/Pt samples with the definition of the coordinate system. Signals of the **(b)** linear (LMR), anisotropic (AMR), spin-Hall (SMR) magnetoresistance effects, **(c)** the unidirectional SMR and **(d)** the transversal Hall resistance for $t_{\text{Co}} = 0.8$ nm. The cobalt layer thickness t_{Co} dependence of **(e)** the resistivity ρ , **(f)** the LMR, AMR and SMR ratios ΔR_{ω} as well as **(g)** the current density normalized USMR $\Delta R_{2\omega}^{\text{USMR}}$ are shown. The strong deviations of the resistivity **(e)** from the ideal two layer model assuming bulk resistivities, Eq. (5.1) depicted by the gray line, suggests microstructural differences of the samples. The generally increasing trend **(f)**, **(g)** of the MR effects follows the magnetization increase (Fig. 4.13c). The inset of panel **(g)** sketches the relative orientation of the spin-polarization direction of the SHE-deflected electrons and the magnetization direction of the ferromagnet. **(h)** The effective fields B_{eff} induced by the field-like and anti-damping-like spin-orbit torque are evaluated from the derivatives of the 1st and 2nd harmonic signal of the transversal Hall resistances **(d)** according to Eq. (5.2).

TABLE 5.1: Cobalt layer thickness t_{Co} scaling of the longitudinal resistivity ρ , the Hall resistance R^{H} and the magnitudes ΔR_{ω} of the linear (LMR), anisotropic (AMR), spin-Hall (SMR) magnetoresistance effects in //CrOx/Co(t_{Co})/Pt samples. The current induced unidirectional SMR $\Delta R_{2\omega}^{\text{USMR}}$ and effective field B_{eff} induced by the field-like (FL) and anti-damping-like (AD) spin-orbit torques are normalized to the current density. The corresponding spin-Hall angle α_{SH} calculated by Eq. (2.6) is given.

t_{Co}	(nm)	0.6	0.7	0.8	0.9	1.0
ρ_0	(n Ω m)	77.2	98.2	104.6	104.5	126.3
ΔR^{H}	(Ω)	1.27	1.63	1.96	2.13	2.05
$\Delta R_{\omega}^{\text{LMR}}$	($\%$ / T)	-0.05	-0.06	-0.09	-0.08	-0.10
$\Delta R_{\omega}^{\text{AMR}}$	($\%$)	0.14	0.22	0.36	0.47	0.69
$\Delta R_{\omega}^{\text{SMR}}$	($\%$)	-2.87	-3.58	-3.78	-4.10	-4.42
$\Delta R_{2\omega}^{\text{USMR}}$	$\left(\frac{\text{m}\Omega \text{cm}^2}{10^7 \text{A}}\right)$	0.62	0.62	1.02	01.12	1.09
T_{AD}	$\left(\frac{\text{mT cm}^2}{10^7 \text{A}}\right)$	0.90	0.74	0.85	0.84	0.60
T_{FL}	$\left(\frac{\text{mT cm}^2}{10^7 \text{A}}\right)$	0.10	-	0.10	-	0.02
α_{SH}	($\%$)	1.9	2.1	2.8	3.3	2.7

The resistivity ρ of the conducting Co/Pt bilayer counter-intuitively increases with t_{Co} , which can not be described in a simple two layer model assuming the respective bulk resistivities. The relevance of the structural details will be discussed elsewhere.

All magnetoresistance effects 5.6f,g show a generally increasing trend with t_{Co} as also the saturation magnetization shows a similar trend (compare Fig. 4.13c). The resistance change ΔR_{ω} of the respective MRs was obtained as shown in Fig. 5.6b by the measurement in all principal field axes. The weakest effect is the field-dependent negative linear MR that is of the order of -0.1 $\%$ / T . It is present in any field direction and therefore has to be accounted for in the analysis of the other effects. The anisotropic MR shows the steepest increase with t_{Co} and is about one order of magnitude smaller than the negative spin-Hall MR with 4 $\%$. In both AMR and SMR shunting by platinum layer has to be considered as a function of the Pt layer thickness and resistivity.

The unidirectional SMR $\Delta R_{2\omega}^{\text{USMR}}$ defined as the halve of the step height of the second harmonic SMR signal (Fig. 5.6c) is a current dependent effect and is therefore normalized to the current density. It is of the order of 1 $\text{m}\Omega/(10^7 \text{A cm}^{-2})$ and significantly increases with t_{Co} .

In the //CrOx/Co(t_{Co})/Pt samples the FL torque is found to be negligible whereas the AD torque provides effective fields B_{eff} between 0.5 and 1 $\text{mT}/(10^7 \text{A cm}^{-2})$. As shown in Fig. 5.6h

the AD torque slightly decreases with increasing cobalt layer thickness. The effective fields were quantified by the harmonic analysis of the transversal Hall resistance (Fig. 5.6d). From the AD torque component the spin Hall angle of the Pt layers can be estimated to about 2 % using Eq. (2.6).

Chapter 6

Discussion

In the following the results of the structural, micromagnetic and magnetotransport investigations on //CrOx/Co/Pt trilayer presented in sections 3.2, 4.4 and 5.4, respectively, will be discussed in context. It is concluded that the DMI strength in general is predominated by the quality of the Co/Pt interface (sec. 6.1) and the exchange parameter is strongly diminished in the ultra-thin film limit (sec. 6.2). The influences of microstructural details and magnetic material properties on the magnetotransport properties of the system are discussed in sec. 6.3. The consequences for magnetic structures in the investigated samples are outlined in sec. 6.4.

6.1 Structural predomination of the DMI strength

The DMI strength is quantified from the asymmetry ratio of DW creep velocities (sec. 4.2) independently from the exchange parameter A . The developed low-field analysis of the creep velocities provides a complementary quantification methods to the most commonly employed evaluation of the DMI-induced asymmetric magnon dispersion. The microstructure-induced large damping (sec 4.1) in the investigated samples precluded the verification of the obtained results by measuring the symmetric magnon dispersion.

The DMI strength of $D_S = -(0.20 \pm 0.09)$ pJ/m in //CrOx/Co/Pt trilayers is almost independent of the cobalt thickness. This indicates the interface-induced character of the DMI mechanism as previously reported in comparable systems [125, 126]. Hence the variation of the cobalt layer thickness is a common approach to tailor the effective DMI constant $D_{\text{eff}} = D_S/t_{\text{Co}}$.

The //Pt(2nm)/Co(1.2nm)/AlOx(2nm) tilayers have larger DMI values of (0.52 ± 0.32) pJ/m and (0.69 ± 0.22) pJ/m in the as-deposited and annealed state respectively. The opposite sign of the asymmetric DW expansion in //CrOx/Co/Pt and //Pt/Co/AlOx trilayers corresponds to a sign change of the Dzyaloshinskii-vector of the system. In case only the Co/Pt interface contributes to the DMI, the sign change is expected due to the inversion of the stacking order. The possible influence of the Co/MO interface is discussed later. The sign inversion of the DMI in //CrOx/Co/Pt trilayers as consequence of the stack order inversion is concluded

from the comparison to //Pt/Co/AlO_x reference samples measured in identical experimental conditions.

In the following the significant difference of DMI values of the investigated samples to those reported in literature is addressed from a structural point of view. The determined DMI values in the here studied samples are considerably smaller than in other reported //Pt/Co/MO systems [53, 125, 126, 138–140], see also Tab. 2.3.

A similar approach to that of Sagasta et al. [14] relating spin-Hall angles to the Pt resistivity to obtain correlations of microstructural properties to the spin-orbit effect strength is applied for the DMI strength. As an indirect indicator of the interface roughness/quality the combined thickness t_{HM} of the Ta and Pt in the bottom layer is evaluated. A strongly diverging Pt resistivity in the ultra-thin limit of Pt films suggest an increase of Pt/Co interface roughness below 5 nm [172–174]. It has been established from structural characterization methods that heavy metals are showing an increasingly rough growth for increasing layer thicknesses above 10 nm [175]. Furthermore, investigations of the DMI strength in systems with ultra-thin Pt cover layers revealed inhomogeneous coverage below 2 nm [143]. The result of these studies suggests the following scenario for the heavy metal film growth. Below the percolation threshold, estimated to be about 2 nm, heavy metals form porous, non-closed layers. This is indicated by almost non-conducting properties [172], the coverage effect in the DMI study of Ref. [143] as well as the finding of this work, that samples with Pt cover layers thinner than 2 nm are susceptible to oxidation. The continuing improvement of the Pt

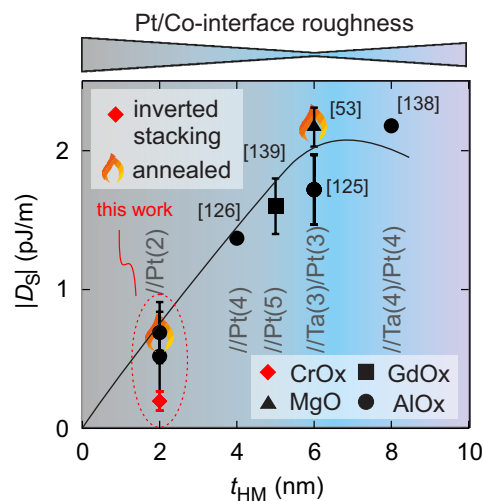


FIGURE 6.1: Comparison of DMI constants in Pt/Co/metal-oxide trilayers from the literature [53, 125, 126, 138, 139] with the results obtained in //CrO_x/Co/Pt trilayers and //Pt/Co/AlO_x reference samples. The combined layer thickness t_{HM} of Ta-buffer and Pt bottom layer serves as qualitative indicator of the Pt/Co interface roughness [172] reaching a minimum at about 6–8 nm. Plotting D_S over t_{HM} reveals a striking dependence that suggest a predomination of the DMI strength by the Pt/Co interface quality.

conductivity up to 6 nm as found in Ref. [172] suggests a smoothening of the layers before the roughness increases again [175]. Hence, the smoothest interfaces for these systems is expected in a thickness range between 6 and 8 nm dependent on the growth conditions of the layer. As the behavior in the ultra-thin limit is related to the wetting of metals on the substrate, it is inferred that the heavy metal kind is of subordinate role for the process. This statement regarding the layer properties is not to be confused with the large dependence of the DMI on the heavy metal kind. As long as the Pt layer is closed (i.e. $t_{\text{Pt}} > 2$ nm) a Ta buffer layer contributes to the smoothening of the layer. Therefore the interface roughness is related to the combined layer thickness of Pt and Ta in this discussion.

Fig. 6.1 shows that D_S and t_{HM} are also correlated in a striking, almost linear dependence. For this comparison the reference samples with only a 2 nm thick platinum bottom layers were prepared. The inverted stacking order in the //CrOx/Co/Pt samples accounts for an additional reduction of the DMI strength, as also found for Pt/Co/MgO trilayers, by a factor of 0.63 [102] due to a modified growth mode of Co/Pt bilayers on metal oxides, resulting in an even rougher interface. The clear impact of the interface quality on the DMI helps to explain the reduced DMI in the //CrOx/Co/Pt samples as a result of unfavorable growth conditions for Pt on the CrOx/Co buffer layers. The reference samples with Co grown on only 2 nm thick Pt yield are similarly rough but have slightly better interfaces. It is therefore concluded, that the DMI strength is predominated by the Pt/Co interface quality.

A cartoon picture of how the roughness may influence the effective DMI constant is presented in sec. 2.3.5.

Recent ab initio calculations, Fig. 2 of Ref. [53] show a complex distribution of DMI contributions in every atomic layer of Pt/Co and Pt/Co/MgO stacks. Considering the calculation results for Pt/Co interfaces, two limits for the DMI are predicted. A maximum DMI of $D^{\text{max}}=2.3$ pJ/m is given by taking into account the contribution of the single Co layer adjacent to the Pt layer. The lower limit or averaged DMI of $\langle D \rangle=1.5$ pJ/m is calculated as the sum over all atomic layer contributions for typical Co layer thicknesses (3 ML). It is further concluded [53] that the presence of the MgO interface results in an average DMI value exceeding $\langle D \rangle$ of the Pt/Co interface. This is attributed to a contribution of same sign and similar strength arising at the Co/MgO interface promising the ability to enhance the DMI by precise engineering of the FM/MO interface.

Figure 6.2 contains a summary of data reported so far on HM/FM/MO systems. The DMI constant D_S and M_S are plotted as a phase diagram [54] to gauge an empirical correlation of the DMI and the details of the sample. A first cluster of comparable Pt/Co/MO samples is formed around an average value of (1.77 ± 0.27) pJ/m. Systems with intrinsically different aluminum- [125, 126, 138], magnesium- [53, 140] or gadolinium [139] oxides yield fairly comparable DMI values considering the error bars. Therefore, it is concluded, that the

Co/Pt-interface is the dominating factor and no clear evidence for an impact of the type of MO on the DMI strength can be found. This result matches with the expectation of weak hybridization of electronic states between Co and MO. In this light the upper cluster lies perfectly within the DFT predicted limits (blue area in Fig. 6.2) suggesting a crucial impact of the Co/Pt interface only. Although a FM/MO contribution might be present, it is not strictly needed to explain the results in the upper cluster. Moreover, it would be required that the DMI contribution arising from the Co/MO interface has the same sign and a similar magnitude independent of the MO (such as Al, Mg or Gd oxides) or its oxidation level.

A second cluster is formed at lower DMI values by our results joined by systems comprised of structurally more complex ferromagnets like CoFeB [126, 140] or different heavy metals (HM) such as Ta, TaN, W and Hf [15, 141, 147] in the bottom layer. It has been suggested that the difference in DMI strength for different HMs originate from their respective electro-negativity [15]. This interpretation might be compromised by the microstructural details of the interfaces, that are expected to vary with the different heavy metals and were disregarded in Ref. [15]. In the clarification of this aspect account should be taken of both for the growth conditions of different HMs and the additional complexity of the employed CoFeB ferromagnetic layer. The latter causes undefined changes of the interface properties due to composition variation and/or boron migration to the interfaces [148]. At the current state, these systems can not be consulted for the evaluation of the possible DMI mechanism.

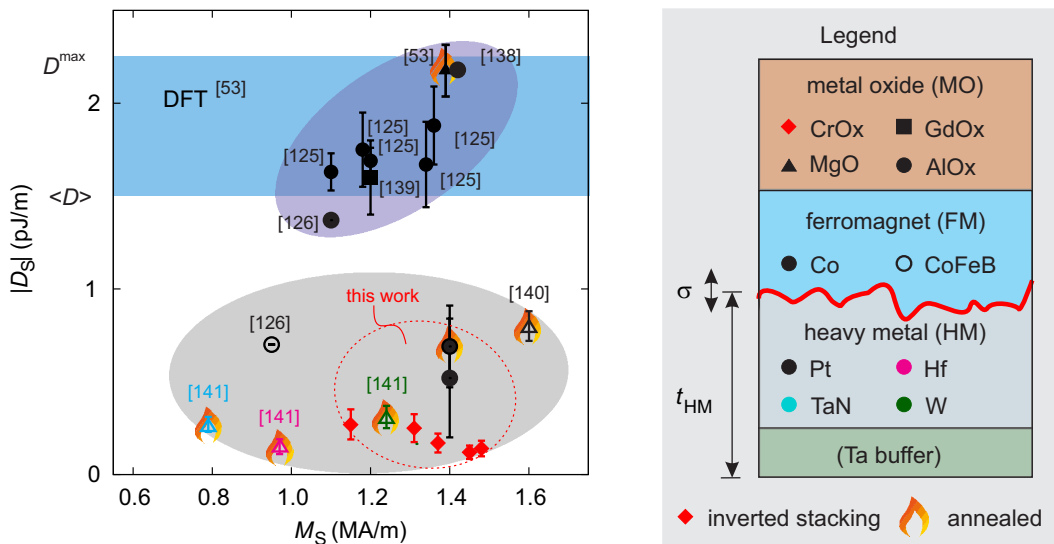


FIGURE 6.2: Comparison of DMI constants in Pt/Co/metal-oxide trilayers from the literature [53, 125, 126, 138–141] with the results from the studied //CrOx/Co/Pt trilayer and //Pt/Co/AlOx reference samples. Two clusters are forming that gather samples of different microstructural qualities. A first cluster consisting of //Pt/Co/MO trilayers with fairly smooth Co/Pt interfaces at larger DMI values that situates in between the limits of D^{\max} and $\langle D \rangle$ given by DFT calculations [53]. Due to various reasons (see text) structural more complex systems form a second cluster at lower DMI values.

Nevertheless, assuming a significant contribution of the Co/MO interface the grouping samples with chromium oxide in the lower cluster could then only be explained by an anti-parallel contribution of the CrOx/Co interface partly canceling that of the Co/Pt interface. The obtained experimental results strongly suggest that the DMI in Pt/Co/MO systems dominantly arises from the Pt/Co interfaces, since no empirical evidence for a contribution of the metal-oxide/Co interface to the DMI strength is obtained. The differences of DMI strength between the samples are likely consequences of different interface qualities. As already discussed in sec. 2.3.3 a number of studies of Pt/Co/Pt trilayers, revealing a partial compensation of the DMIs arising from top and bottom interface, support this interpretation.

6.2 Ultra-thin limit exchange parameter reduction

The cobalt layer thickness in //CrOx/Co(t_{Co})/Pt trilayers has a strong impact not only on the saturation magnetization and the effective anisotropy but also on the exchange parameter A . After employing the developed approach to determine the DMI constant independently of the exchange parameter, A can be quantified from the size of circular magnetic objects. Judging from the t_{Co} -scaling of the diameter, the objects are identified as magnetic bubble domains. In the framework of bubble domain theory the exchange parameter can be deduced from the collapse diameter of magnetic bubble domains (sec. 4.3). For samples satisfying the condition $Q = K_{\text{eff}}/K_0 > 1.5$ the study of bubble domain stability offers a quasistatic alternative to methods relying on magnetization dynamics [152, 160].

As the investigations revealed the exchange parameter in the ultra thin Co layer can be diminished up to an order of magnitude compared to the cobalt bulk exchange value $A^b = 16$ pJ/m. This trend is supported by the approximative estimation of A from the extrapolated Curie temperature. A similar reduction of A was reported in a comparable system [152]. The reduction is attributed to a microstructural origin, e.g. an increasing number of grain boundaries with decreasing cobalt layer thickness in the ultrafinely polycrystalline samples.

With the significantly diminished A the expected domain wall width Δ as well as the exchange length l_{ex} can be smaller than 2 nm responsible for the strong susceptibility of DWs to small pinning sites as e.g. grain boundaries.

6.3 Magnetotransport properties

The increase of the resistivity (Fig. 5.6) of the conductive Co/Pt bilayer towards larger cobalt layer thicknesses suggests a microstructural impact on the transport properties. A description in the simple ideal two layer picture assuming the bulk resistivities of the individual layers, Eq. (5.1), is not possible. Contrarily to the obtained result, a decreasing trend is predicted,

when the total amount of metal increases. The modified growth conditions of Pt layers on differently thick Co seed layers possibly lead to intermixing, roughening and percolation that are factors for the resistance increase. The large sensitivity of transport measurements serves as an indicator for microstructural property changes that can hardly be resolved in standard structural characterization methods. The measured depth profiles (sec. 3.2) can not reveal significant differences between the thinnest and thickest CrOx/Co/Pt sample. In consideration of these microstructural property changes indicated by the resistivity trend, the slight decrease of the interface-induced DMI constant (Fig. 4.13c) is likely to originate from a degrading Co/Pt interface quality towards larger Co layer thicknesses.

The microstructural details of the intermixed, rough and percolated Co/Pt bilayer will also impact the magnetotransport properties. The interpretation of all effects has to consider a large deviation from the idealistic two layer picture. Consequently, an inhomogeneous current density across the stack cross section are expected, which in turn alters e.g. the spin-Hall effect, the shunting effect of the Pt layer etc. In the investigated MO/Co/Pt stacks the two conducting layers with ferro- and paramagnetic properties influence each other. The condition at the interface imply a magnetic proximity effect (MPE) in Pt and Co, which alters their transport properties. The induction of magnetic moments in Pt layers that are in proximity to a ferromagnet can be revealed by element-specific magnetometry using the X-ray magnetic circular dichroism (XMCD) [176] or spin-polarized scanning tunneling spectroscopy [177]. Early studies revealed a significant contaminating influence of the MPE on the spin-orbit and spin-caloric effects [178]. Recently the spin-Hall effect (SHE) induced anomalous Hall effect (AHE) [91] in Pt was debated, that could be mutually explanatory for the MPE.

In the light of the unclear moment density, current distribution and shunting the following interpretation of the magnetoresistance effects remains therefore to some extent speculative. The transversal Hall resistance shows an increasing trend with increasing t_{Co} . A direct correlation to the Hall coefficient is not given. The footprint of the increasing saturation magnetization measured by the VSM (Fig. 4.13c) towards larger t_{Co} naturally appears in all MR effects (Fig. 5.6f) as they couple to the localized moments. This holds also for the field-dependent LMR, possibly due to the increasing disorder in the system.

However, a difference in the slopes in the MR ratios is apparent, where the AMR increases faster with t_{Co} than the SMR. These trends are roughly related to the shunting in the system. At constant Pt thicknesses the AMR has to increase with the increasing fraction of cobalt. The SMR on the other hand relies on the interaction of spin-polarized electrons with the ferromagnetic layer only at the interface. The short spin diffusion length in ferromagnets prevents a contribution of electrons to the SMR that penetrate to far into the Co, hence effectively only the proximate interface is relevant for the SMR. Adding further ferromagnetic material will then only result in the shunting of the effect.

The effective fields cause by the SOTs are quantified from the harmonic analysis of the transversal resistances (sec. 5.3). In their evaluation contributions from the spincaloric anomalous Nernst effect (ANE) and the Oersted field have to be considered.

The full magnitude of the parallel effective field is attributed to the anti-damping spin-orbit torque (AD-SOT). In Co/Pt bilayers the ANE contribution was found to be negligible small [106]. Changes of the thermal properties, e.g. by an inverted stack order, technically requires the reevaluation of the different contributions to the second harmonic signal (sec. 2.2.4). Due to the comparable disorder of the Co/Pt layer these changes are inferred to be insignificant. Hence, the AD-SOT is directly measured and is of the order of $1 \text{ mT}/10^7 \text{ A cm}^{-2}$ per unit moment with a slightly decreasing Co thickness trend. The spin-Hall angle of the 2 nm thick Pt layer can be estimated with Eq. (2.6) to $\alpha_{\text{SH}} \approx 2 \%$. The value fits to the empirical relation given in Fig. 4 of Ref. [14] for a Pt resistivity of about $100 \text{ n}\Omega\text{m}$. Assuming a spin-diffusion length of about $\lambda_{\text{sf}}=2 \text{ nm}$ for Pt the bulk SH angle calculated from Eq. (2.3) is about 7.4% . However, this larger value would no longer agree with the empirical relation. The consistency of the two models each based on an idealistic layer architecture are compromised by the microstructural details of the rough and uneven Pt layer. Despite this fact the nominal Pt thickness is used to calculate the resistivity and the bulk SH angle from Eq. (2.3) and naturally causes deviations.

The transversal effective field obtained in the SOT quantification measurements is small, which equally suggests a negligible magnitude of field-like (FL) SOT. It was pointed out [179], that in Co/Pt bilayers the FL-SOT is partially compensated by the Oersted field, which is estimated to be approximately 0.4 mT in the investigated devices. The SHE with inverted sign as e.g. found in Ta entails the constructive superposition of the two field components [15, 20, 95, 106]. A further enhancing mechanism for SOT magnitudes due to thermal stabilization was found in a study, that systematically changed the repetition number N of $[\text{Pt}/\text{Co}/\text{Ta}]_N$ and $[\text{Co}/\text{Pt}]_N$ multilayers [104].

As in the case of the DMI constant also the SOT magnitudes are significantly smaller in comparison to the so far reported results in comparable systems containing a Pt/Co bilayer [20, 99, 104, 105]. The SOT data situation for the structurally modest systems containing Co/Pt bilayers is less extensive than that of the DMI. The obtained results support the conclusion of a large susceptibility of the SOT strength on the microstructural details of the samples [20, 98], i.e. the layer and interface quality controls the transport and interaction properties of the spin-polarized electrons. With a value of $1 \text{ mT}/10^7 \text{ A cm}^{-2}$ per unit moment the AD-SOT component is significantly lower than the values reported for similar Pt/Co bilayer systems [20, 105]. It was shown that annealing can cause a reduction of 23% . In concordance with the significant reduction of the DMI constants in the //CrOx/Co/pt systems, it is inferred that also the SOT strength is dominated by the microstructural sample quality.

In the measurements of the unidirectional spin-Hall magnetoresistance (USMR) the SOT and ANE contributions are neglected. The obtained amplitude of the order of $1 \text{ m}\Omega/10^7 \text{ A cm}^{-2}$ with an increasing Co thickness trend is therefore fully attributed to the USMR. This value verifies the results obtained in the study of Pt/Co/AlOx systems [112], which also stated that this effect is most pronounced for a Pt thickness around 2 nm. The GMR interpretation appears to be a valid description. With increasing Co thickness trend the total moment of the fixed layer increases while the moment of the spin accumulation also slightly increases, given the increasing trend of the spin-Hall angle. This could explain the increase of the USMR magnitude towards larger t_{Co} . The complex transport details of electrons passing this artificial GMR bilayer are yet to be understood. Since a ballistic propagation perpendicular to the interface normal can not explain the effect a permanent scattering trough the artificial GMR-bilayer is required. This situation is provided in case of the here studied systems with largely disordered interface regions.

6.4 Magnetic structures in //CrOx/Co/Pt trilayers

With the determined DMI strength all samples safely remain in the limit of a collinear ferromagnetic ground-state. Due to the large anisotropy the effective DMI constants are at most 33 % of the theoretical limit or the critical DMI constant D_c , Eq. (2.19), for the formation of modulated spiral and skyrmion phases.

The DW energy is reduced by 1-6 % in the CrOx/Co/Pt samples due to the DMI. However, it is sufficient to induce modifications to the DW providing homochiral and Néel-type properties. Consequently, the formation of winding pairs (sec. 4.2.3) and a coherent current-induced DW motion (sec. 4.3) is observed in the samples. It is therefore concluded that the magnetic bubble domains are also confined by a homochiral DW.

With the complete set of micromagnetic parameters the theoretically expected diameters d_{Sy} of isolated skyrmions were calculated. For the studied sample series d_{Sy} lies in a range between 40 and 200 nm. By tuning the DMI strenght to small values, the skyrmions are expected to increase in size according to the chiral modulation length L_D , Eq. (2.18). The simultaneous decrease of the exchange parameter in the presented system compensates for this effect leaving the skyrmions in an diameter range inaccessible to Kerr microscopy. It is stressed, that in case the micromagnetic parameters or the object type are not explicitly known, conclusions from the object size on the material parameters or vice versa can be ambiguous.

Despite unobvious differences in the structural characterization the pinning of DWs increases towards larger cobalt thicknesses. Signatures of this trend are an increasing number of nucleation sites, the evolution of disrupted DW morphology and lower current- or field-driven mobility of DWs causing a low mobility of magnetic bubble domains in the films.

Chapter 7

Conclusion and Outlook

The complex interplay of effects originating from the spin-orbit coupling and their dependencies on the microstructural details of the material system mandates a holistic characterization of its properties. At the current state of the field, this work attempts to investigate the asymmetrically sandwiched ferromagnetic thin film system //CrOx/Co/Pt in such a way. Thereby, a comprehensive set of materials parameters is provided that enables further examinations, some of which are outlined in the following in the context of the recent advances in this area of research.

This work emphasizes the aspect of the microstructural impact on the strength of spin-orbit effects. Its further experimental investigations [98, 144] as well as its implementation in first-principle calculations is required to reveal the detailed relation between the structural characteristics and the spin-orbit effect mechanisms. Thereby, tuning possibilities for spin-orbit effects could be revealed to adjust the individual effect magnitudes by a proper synthesis of the materials. The system disorder could for instance be deterministically tuned by ion implantation [180].

To reach large mobilities of magnetic information entities like domain walls (DW), bubbles or skyrmions a further clarification of the role of pinning is crucial. As it appeared in this study the disorder naturally causes increased pinning, that was not observed as severely e.g. in the bubble blowing experiment of Ref. [3]. In the framework of the classical DW creep theory (sec. 4.2.1) the parameters for the description of the pinning process and its characteristic length scale can be quantitatively assessed. In granular polycrystalline films these parameters are determined by e.g. the grain size or details of the grain boundaries, that cause lateral variations in the landscape of the micromagnetic parameters, which has to be properly implemented in micromagnetic simulations.

The functionality of asymmetric systems can be further extended to material systems obtaining antiferromagnetic and magnetoelectric properties such as Cr₂O₃. The usage of chromium oxide in this work, although it does not obtain antiferromagnetic properties in the amorphous form (see sec. 4.1), holds out the prospect of the introduction of the exchange

bias (EB) effect as a useful tool for spin-orbit devices. It was successfully demonstrated that the requirement of external in-plane field for the spin-orbit torque (SOT) switching can be overcome with the help of the in-plane EB effect of IrMn [181]. Cr₂O₃ in its crystalline form obtains the properties of a collinear antiferromagnet with a surface-terminated uncompensated top layer of magnetic moments. In conjunction with its magnetoelectric properties a purely antiferromagnetic magnetoelectric random access memory element was created [182]. It is anticipated that a local destruction of the antiferromagnetic and magnetoelectric properties of Cr₂O₃ for example by ion-implantation, could be an interesting concept for the local favoring of certain skyrmions polarities by the out-of-plane EB effect of Cr₂O₃. In skyrmion logic and memory devices, where the skyrmion polarity represents the logic state, this could for instance be used as a filter.

In this work the necessity for a strict distinction of magnetic objects stabilized by magneto-static or Dzyaloshinskii-Moriya interaction (DMI), i.e. homochiral magnetic bubble domains and skyrmions, is pointed out. This poses questions of the details of a possible transmutation process between these magnetic structures, that have not been addressed so far. Nevertheless, the determined well-defined materials parameter set allows for the micromagnetic simulation of static properties of DWs, bubble domains, skyrmions etc.

The understanding of the DW structure in ferromagnetic films is of great importance to design efficient DW based memory and logic devices. Magnetoresistances (MR) effects like the anisotropic MR and the spin-Hall MR could provide sensitive tools to measure the in-plane magnetization components of these magnetic structures. The DW resistance is determined by the DW type depending on the orientation of its in-plane magnetization component. The orientation either transversal (Bloch wall) or longitudinal (Neél wall) with respect to the stripe axis/current direction causes spin-Hall MR and anisotropic MR respectively. The unidirectional spin-Hall MR can additionally be employed to determine the sign of the transversal magnetization component.

The small DW width of only a few nanometer poses experimental challenges due to the expected low signal of an individual DW. The low MR signals in the %₀₀-range will be further reduced by the fraction of the DW of the investigated stripe, roughly the ratio of DW width Δ and the distance of the contact separation. Technically, this requires a contact separation distance of the order of the DW. Therefore alternative approaches seek a signal increase by trapping many DWs between the contacts by the introduction of artificial pinners [10, 183]. It is understood, that during the fabrication process of pinners the material properties can be altered which causes changes in the DW type.

In the regime of small DMI, DWs might only be partially transformed from a Bloch into a Neel wall yielding a DW configuration with the magnetization rotating about a skewed axis. In the geometrical confinement of nanostripes the magneto-static interactions possibly result

in a tilted equilibrium DW position. The DW morphology is further influenced by pinning and microstructural aspects like roughness. Consequently the measured DW resistance consists of MR components that need to be carefully attributed to the details of the DW structure. This might lead to ambiguities in the discrimination of ideal Bloch and Néel walls. In a careful measurement scheme the resistance measurements could allow conclusions on the influence of the DMI on the DW structure, e.g. resulting in a chiral MR [17].

The sophisticated interpretation in systems with conducting ferromagnetic layers, where the magnetotransport properties are dominated by the ferromagnetic layer, relies on the progress of the investigation in YIG/Pt systems. The ferrimagnetic insulator yttrium iron garnet (YIG) in conjunction with Pt thin films represents a model system for these studies, since the observation of transport phenomena like the anisotropic MR, anomalous Hall effect can be directly attributed to the Pt layer itself. In reference systems Cu spacers are introduced, that allow a dissipation-less exchange of polarized electrons between Pt and YIG, but sufficiently separate both layers to suppress the magnetic proximity effect. In this context, the persistence of the SMR independent of the Cu spacer has been demonstrated [90]. Due to its large spin diffusion length the Cu spacer is transparent for spin polarized electrons. Hence the spin accumulation generated by the SHE can freely interact with the individual sublattice moments of the ferrimagnet [184] and pass spin information back to the Pt layer which can cause a magnetic polarization responsible for a AHE there [185]. In bilayer systems with Pt in direct proximity to a conducting ferromagnet both MPE and SHE-AHE are expected. In a scaling study of $Pt t_{Pt}/Cu(t_{Cu})/YIG$ the MPE or SHE-induced AHE could be possibly distinguished, since the MPE scales with the reduction of the magnetic field ($1/t_{Cu}$) while the SHE-induced AHE should reflect the sech-function behavior of the SHE.

Furthermore, dynamic simulations of current-induced DW and skyrmion motion could be performed using the here determined transport properties and SOTs. Appropriate models need to account for details such as the granular structure of the films, by introducing realistic assumptions about the lateral micromagnetic parameter landscape. In this way, simulations employing the lateral variations of the DMI strength are used to explain the enhancement of the critical currents for skyrmion motion in case of coinciding skyrmion diameter and grain size [13]. If the grain and skyrmion sizes match, skyrmions are effectively pinned in grains with larger DMI values.

Appendix A

Appendix

A.1 Calculation of the skyrmion diameter

This section, provided by O. Volkov, describes the model used for the calculation of the skyrmion diameters from the experimentally determined magnetic materials parameters. For the analysis of skyrmion diameters the micro-magnetic framework with the continuous description of Dzyaloshinskii-Moriya interaction [7, 186] is used. As a model, a thin ferromagnetic infinite plate of thickness h along the $\hat{\mathbf{z}}$ -axis is considered. Taking into account that thickness of ferromagnetic layer is smaller than characteristic magnetic length, we consider a uniform average values of magnetic parameters along the $\hat{\mathbf{z}}$ -axis. It is also assumed, that the magneto-static interaction, which is always present in the system, can be reduced to the easy-surface anisotropy, which results to the appearance of effective anisotropy coefficient K_{eff} . Due to this, the total micro-magnetic energy density of our system will have a following form

$$\mathcal{E} = A [(\nabla m_x)^2 + (\nabla m_y)^2 + (\nabla m_z)^2] - K_{\text{eff}} (\mathbf{m} \cdot \mathbf{n})^2 - \mathbf{M} \cdot \mathbf{B} - D_S [m_n \nabla \cdot \mathbf{m} - (\mathbf{m} \cdot \nabla) m_n], \quad (\text{A.1})$$

where the exact form of interface-induced DMI term is taken into account, with \mathbf{n} as the unity vector directed perpendicular to the interface surface along the $\hat{\mathbf{z}}$ -axis. For the case of simplicity, the cylindrical coordinate system with $\mathbf{r} = (r \cos \chi, r \sin \chi, z)$ is introduced and the angular parametrization for the reduced magnetization vector $\mathbf{m} = \mathbf{M}/M_S = (\cos \phi \sin \theta, \sin \phi \sin \theta, \cos \theta)$ used. In this case, the total energy density (A.1) will have the following form

$$\begin{aligned} \mathcal{E} = A \left\{ \left(\frac{\partial \theta}{\partial r} \right)^2 + \frac{1}{r^2} \left(\frac{\partial \theta}{\partial \chi} \right)^2 + \sin^2 \theta \left[\left(\frac{\partial \phi}{\partial r} \right)^2 + \frac{1}{r^2} \left(\frac{\partial \phi}{\partial \chi} \right)^2 \right] \right\} - K_{\text{eff}} \cos^2 \theta - M_S B \cos \theta \\ - D_S \left\{ \sin(\phi - \chi) \left[\frac{1}{r} \frac{\partial \theta}{\partial \chi} - \sin \theta \cos \theta \frac{\partial \phi}{\partial r} \right] + \cos(\phi - \chi) \left[\frac{\partial \theta}{\partial r} + \frac{\sin \theta \cos \theta}{r} \frac{\partial \phi}{\partial \chi} \right] \right\}. \end{aligned} \quad (\text{A.2})$$

Looking for azimuthally symmetric solutions, which represent either skyrmion or skyrmion-bubble textures [12, 127]

$$\theta = \theta(r), \quad \phi = \phi(\chi), \quad (\text{A.3})$$

where $\phi(\chi)$ is a linear function with respect to χ . This allows to simplify the expression (A.2) and derive the total energy of a chiral axisymmetric magnetic texture:

$$E = 2\pi \int_0^\infty dr \left\{ A \left(\theta_r^2 + \frac{1}{r^2} \sin^2 \theta \right) - D_S \left(\theta_r + \frac{1}{2r} \sin(2\theta) \right) - K_{\text{eff}} \cos^2 \theta - B M_S \cos \theta \right\}. \quad (\text{A.4})$$

The Euler-Lagrange equation for the total energy functional (A.4) has the following form,

$$A \left[\theta_{rr} + \frac{\theta_r}{r} - \frac{\sin(2\theta)}{2r^2} \right] - D_S \frac{\sin^2 \theta}{r} - \frac{1}{2} K \sin(2\theta) - \frac{1}{2} B M_S \sin \theta = 0, \quad (\text{A.5})$$

with boundary conditions for isolated axisymmetric skyrmion:

$$\theta(0) = 0, \quad \theta(\pi) = \pi. \quad (\text{A.6})$$

The boundary value problem (A.5) and (A.6) can be solved numerically by using the finite-difference method. Usually the function $\theta(r)$ has spike-like shape in the vicinity of point $r = 0$ and decays exponentially at high distances from the skyrmion center. The characteristic size of a localized magnetization profile $\theta(r)$ is usually defined as [12, 127, 130]

$$r_{\text{sk}} = r_0 - \theta_0 \left(\frac{d\theta}{dr} \right)_{r=r_0}^{-1}, \quad (\text{A.7})$$

where (r_0, θ_0) is the inflection point of the profile $\theta(r)$.

A.2 Micromagnetic simulation of the winding pair stability

Example of the used mumax3.3.8.1 code provided by T. Schneider.

```
// Material Parameters Msat = 1480e3 // saturation magnetization in
A/m
Aex = 16e-12 // exchange constant in J/m
Dind = 0.21e-3 // interfacial DMI in J/m^2
thickness := 1.0e-9 // film thickness in nm
Ku1 = 1.62e6 // first order anisotropy constant Ku in J/m^3
Ku2 = 0 // second order anisotropy constant in J/m^3
AnisU = vector(0, 0, 1) // direction of the uniaxial Anisotropy
```

```
Bstart := 0 // starting field in mT
Bend := 250 // ending field in mT
Bstep := 0.5 // field step in mT

Bcount := floor((Bend - Bstart)/Bstep) // number of field step as
int

// Geometry
Nx := 1024 // number of cells in x-direction
Ny:= 256 // number of cells in y-direction
Nz:= 1 // number of cells in z-direction

lex := sqrt(Aex.GetRegion(1) / (0.5 * mu0 * pow(Msat.GetRegion(1),
2))) // exchange length
domainL := sqrt(Aex.GetRegion(1)/Kul.getRegion(1)) // domain wall width

alpha = 0.5 // gilbert damping
g_fct := 2.13 // gyromagnetic ratio

setgridsize(nx, ny, nz) // Internal mumax function to set grid
setcellsize(1e-9, 1e-9, thickness/Nz) // Internal mumax function to set
cell size
SetPBC(128,128,0) // number of repetitions for PBC

//save (B_demag)

//m = TwoDomain(0,0,1, 0,0,-1, 0,0,1)
m.loadfile("relaxed.ovf")
tableadd(B_ext)
minimize()
for i:=0; i<Bcount; i =i+1{
B_ext = vector(0,0,(Bstart+(i+1)*Bstep)/1000)
minimize()
tablesave()
save(m)
if (m.comp(2).average() > 0.9999){
exit()
} }
}
```


Bibliography

1. Bogdanov A. N., A. N. & Yablonsky, D. A. Thermodynamically Stable Vortexes in Magnetically Ordered Crystals - Mixed State of Magnetics. *Zhurnal Eksperimentalnoi I Teoreticheskoi Fiziki* **95**, 178–182 (Jan. 1989).
2. Bogdanov, A. N. & Rößler, U. K. Chiral symmetry breaking in magnetic thin films and multilayers. *Physical Review Letters* **87**, 037203 (July 2001).
3. Jiang, W. J. *et al.* Blowing magnetic skyrmion bubbles. *Science* **349**, 283–286 (July 2015).
4. Thiaville, A., Rohart, S., Jue, E., Cros, V. & Fert, A. Dynamics of Dzyaloshinskii domain walls in ultrathin magnetic films. *EPL* **100**, 57002 (Dec. 2012).
5. Kiselev, N. S., Bogdanov, A. N., Schäfer, R. & Rößler, U. K. Chiral skyrmions in thin magnetic films: new objects for magnetic storage technologies? *Journal of Physics D-applied Physics* **44**, 392001 (Oct. 2011).
6. Parkin, S. S. P., Hayashi, M. & Thomas, L. Magnetic domain-wall racetrack memory. *Science* **320**, 190–194 (Apr. 2008).
7. Fert, A., Cros, V. & Sampaio, J. Skyrmions on the track. *Nature Nanotechnology* **8**, 152–156 (Mar. 2013).
8. Soumyanarayanan, A., Reyren, N., Fert, A. & Panagopoulos, C. Emergent phenomena induced by spin-orbit coupling at surfaces and interfaces. *Nature* **539**, 509–517 (Nov. 2016).
9. Wiesendanger, R. Nanoscale magnetic skyrmions in metallic films and multilayers: a new twist for spintronics. *Nature Reviews Materials* **1**, 16044 (June 2016).
10. Franken, J. H., Herps, M., Swagten, H. J. M. & Koopmans, B. Tunable chiral spin texture in magnetic domain-walls. *Scientific Reports* **4**, 5248 (June 2014).
11. Monchesky, T. L. SKYRMIONS Detection with unpolarized currents. *Nature Nanotechnology* **10**, 1008–1009 (Dec. 2015).
12. Butenko, A. B., Leonov, A. A., Rossler, U. K. & Bogdanov, A. N. Stabilization of skyrmion textures by uniaxial distortions in noncentrosymmetric cubic helimagnets. *Physical Review B* **82**, 052403 (Aug. 2010).

13. Legrand, W. *et al.* Room-Temperature Current-Induced Generation and Motion of sub-100 nm Skyrmions. *Nano Letters* **17**, 2703–2712 (Apr. 2017).
14. Sagasta, E. *et al.* Tuning the spin Hall effect of Pt from the moderately dirty to the superclean regime. *Phys. Rev. B* **94**, 060412 (6 Aug. 2016).
15. Torrejon, J. *et al.* Interface control of the magnetic chirality in CoFeB/MgO heterostructures with heavy-metal underlayers. *Nature Communications* **5**, 4655 (Aug. 2014).
16. Yu, J. W. *et al.* Spin orbit torques and Dzyaloshinskii-Moriya interaction in dual-interfaced Co-Ni multilayers. *Scientific Reports* **6**, 32629 (Sept. 2016).
17. Yin, Y. *et al.* Chiral magnetoresistance in Pt/Co/Pt zigzag wires. *Applied Physics Letters* **110**, 122401 (2017).
18. Khvalkovskiy, A. V. *et al.* Matching domain-wall configuration and spin-orbit torques for efficient domain-wall motion. *Physical Review B* **87**, 020402 (Jan. 2013).
19. Zutic, I., Fabian, J. & Das Sarma, S. Spintronics: Fundamentals and applications. *Reviews of Modern Physics* **76**, 323–410 (Apr. 2004).
20. Garello, K. *et al.* Symmetry and magnitude of spin-orbit torques in ferromagnetic heterostructures. *Nature Nanotechnology* **8**, 587–593 (Aug. 2013).
21. Nagaosa, N. & Tokura, Y. Topological properties and dynamics of magnetic skyrmions. *Nature Nanotechnology* **8**, 899–911 (Dec. 2013).
22. Baibich, M. N. *et al.* Giant Magnetoresistance of (001)Fe/(001)Cr Magnetic Superlattices. *Phys. Rev. Lett.* **61**, 2472–2475 (21 Nov. 1988).
23. Binasch, G., Grünberg, P., Saurenbach, F. & Zinn, W. Enhanced magnetoresistance in layered magnetic structures with antiferromagnetic interlayer exchange. *Phys. Rev. B* **39**, 4828–4830 (7 Mar. 1989).
24. Allwood, D. A. *et al.* Magnetic domain-wall logic. *Science* **309**, 1688–1692 (Sept. 2005).
25. Hayashi, M., Thomas, L., Moriya, R., Rettner, C. & Parkin, S. S. P. Current-controlled magnetic domain-wall nanowire shift register. *Science* **320**, 209–211 (Apr. 2008).
26. Simonite, T. IBM Makes Revolutionary Racetrack Memory Using Existing Tools. *MIT Technology Review* (2011).
27. Hrabec, A. *et al.* Current-induced skyrmion generation and dynamics in symmetric bilayers. **8**. Article, 15765 (June 2017).
28. Ralph, D. C. & Stiles, M. D. Spin transfer torques. *Journal of Magnetism and Magnetic Materials* **320**, 1190–1216 (Apr. 2008).

29. Mihai Miron, I. *et al.* Current-driven spin torque induced by the Rashba effect in a ferromagnetic metal layer. *Nature Materials* **9**, 230–234 (Mar. 2010).
30. Emori, S., Bono, D. C. & Beach, G. S. D. Interfacial current-induced torques in Pt/Co/GdOx. *Applied Physics Letters* **101**, 042405 (2012).
31. Lee, J. C. *et al.* Universality Classes of Magnetic Domain Wall Motion. *Physical Review Letters* **107**, 067201 (Aug. 2011).
32. Ryu, K.-S., Thomas, L., Yang, S.-H. & Parkin, S. S. Current Induced Tilting of Domain Walls in High Velocity Motion along Perpendicularly Magnetized Micron-Sized Co/Ni/Co Racetracks. *Applied Physics Express* **5**, 093006 (2012).
33. Hirsch, J. E. Spin Hall effect. *Physical Review Letters* **83**, 1834–1837 (Aug. 1999).
34. Rojas Sanchez, J. C. *et al.* Spin-to-charge conversion using Rashba coupling at the interface between non-magnetic materials. *Nature Communications* **4**, 2944 (Dec. 2013).
35. Sangiao, S. *et al.* Control of the spin to charge conversion using the inverse Rashba-Edelstein effect. *Applied Physics Letters* **106**, 172403 (2015).
36. Emori, S., Bauer, U., Ahn, S.-M., Martinez, E. & Beach, G. S. D. Current-driven dynamics of chiral ferromagnetic domain walls. *Nature Materials* **12**, 611–616 (July 2013).
37. Ryu, K.-S., Yang, S.-H., Thomas, L. & Parkin, S. S. P. Chiral spin torque arising from proximity-induced magnetization. *Nature Communications* **5**, 3910 (May 2014).
38. Miron, I. M. *et al.* Perpendicular switching of a single ferromagnetic layer induced by in-plane current injection. *Nature* **476**, 189 (Aug. 2011).
39. Liu, L. Q. *et al.* Spin-Torque Switching with the Giant Spin Hall Effect of Tantalum. *Science* **336**, 555–558 (May 2012).
40. Chen, G. *et al.* Novel Chiral Magnetic Domain Wall Structure in Fe/Ni/Cu(001) Films. *Physical Review Letters* **110**, 177204 (Apr. 2013).
41. Benitez, M. J. *et al.* Magnetic microscopy and topological stability of homochiral Neel domain walls in a Pt/Co/AlOx trilayer. *Nature Communications* **6**, 8957 (Dec. 2015).
42. Tetienne, J. P. *et al.* The nature of domain walls in ultrathin ferromagnets revealed by scanning nanomagnetometry. *Nature Communications* **6**, 6733 (Apr. 2015).
43. Hassel, C., Brands, M., Lo, F. Y., Wieck, A. D. & Dumpich, G. Resistance of a single domain wall in (Co/Pt)(7) multilayer nanowires. *Physical Review Letters* **97**, 226805 (Dec. 2006).

44. Haazen, P. P. J. *et al.* Domain wall depinning governed by the spin Hall effect. *Nature Materials* **12**, 299–303 (Apr. 2013).
45. Chen, G. *et al.* Tailoring the chirality of magnetic domain walls by interface engineering. *Nature Communications* **4**, 2671 (Oct. 2013).
46. Bogdanov, A. N. & Hubert, A. Thermodynamically Stable Magnetic Vortex States in Magnetic Crystals. *Journal of Magnetism and Magnetic Materials* **138**, 255–269 (Dec. 1994).
47. Crepieux, A. & Lacroix, C. Dzyaloshinsky-Moriya interactions induced by symmetry breaking at a surface. *Journal of Magnetism and Magnetic Materials* **182**, 341–349 (Feb. 1998).
48. Bode, M. *et al.* Chiral magnetic order at surfaces driven by inversion asymmetry. *Nature* **447**, 190–193 (May 2007).
49. Yu, X. Z. *et al.* Real-space observation of a two-dimensional skyrmion crystal. *Nature* **465**, 901–904 (June 2010).
50. Sampaio, J., Cros, V., Rohart, S., Thiaville, A. & Fert, A. Nucleation, stability and current-induced motion of isolated magnetic skyrmions in nanostructures. *Nature Nanotechnology* **8**, 839–844 (Nov. 2013).
51. Romming, N. *et al.* Writing and Deleting Single Magnetic Skyrmions. *Science* **341**, 636–639 (Aug. 2013).
52. Jiang, W. J. *et al.* Direct observation of the skyrmion Hall effect. *Nature Physics* **13**, 162–169 (Feb. 2017).
53. Boulle, O. *et al.* Room-temperature chiral magnetic skyrmions in ultrathin magnetic nanostructures. *Nature Nanotechnology* **11**, 449 (May 2016).
54. Woo, S. *et al.* Observation of room-temperature magnetic skyrmions and their current-driven dynamics in ultrathin metallic ferromagnets. *Nature Materials* **15**, 501 (May 2016).
55. Baker, K. F. A Review of Magnetic-bubble Memories and Their Applications. *Radio and Electronic Engineer* **51**, 105–116 (1981).
56. Gambardella, P. & Mihai Miron, I. Current-induced spin-orbit torques. *Philosophical Transactions of the Royal Society A-mathematical Physical and Engineering Sciences* **369**, 3175–3197 (Aug. 2011).
57. Hoffmann, A. Spin Hall Effects in Metals. *Ieee Transactions on Magnetics* **49**, 5172–5193 (Oct. 2013).
58. Jungwirth, T., Wunderlich, J. & Olejnik, K. Spin Hall effect devices. *Nature Materials* **11**, 382–390 (May 2012).

59. Sinova, J., Valenzuela, S. O., Wunderlich, J., Back, C. H. & Jungwirth, T. Spin Hall effects. *Reviews of Modern Physics* **87**, 1213–1259 (Oct. 2015).
60. Popovic, Z. S., Kurdestany, J. M. & Satpathy, S. Electronic structure and anisotropic Rashba spin-orbit coupling in monolayer black phosphorus. *Physical Review B* **92**, 035135 (July 2015).
61. Weiler, M. *et al.* Experimental Test of the Spin Mixing Interface Conductivity Concept. *Physical Review Letters* **111**, 176601 (Oct. 2013).
62. Mott, N. F. The Scattering of Fast Electrons by Atomic Nuclei. *Proceedings of the Royal Society of London A: Mathematical, Physical and Engineering Sciences* **124**, 425–442. ISSN: 0950-1207 (1929).
63. Dyakonov, M. I. & Perel, V. I. Possibility of Orienting Electron Spins with Current. *Jetp Letters-ussr* **13**, 467 (1971).
64. Kato, Y. K., Myers, R. C., Gossard, A. C. & Awschalom, D. D. Observation of the spin hall effect in semiconductors. *Science* **306**, 1910–1913 (Dec. 2004).
65. Niimi, Y. *et al.* Extrinsic spin Hall effects measured with lateral spin valve structures. *Phys. Rev. B* **89**, 054401 (5 Feb. 2014).
66. Sinitsyn, N. A., MacDonald, A. H., Jungwirth, T., Dugaev, V. K. & Sinova, J. Anomalous Hall effect in a two-dimensional Dirac band: The link between the Kubo-Streda formula and the semiclassical Boltzmann equation approach. *Phys. Rev. B* **75**, 045315 (4 Jan. 2007).
67. Nagaosa, N., Sinova, J., Onoda, S., MacDonald, A. H. & Ong, N. P. Anomalous Hall effect. *Reviews of Modern Physics* **82**, 1539–1592 (May 2010).
68. Wunderlich, J., Kaestner, B., Sinova, J. & Jungwirth, T. Experimental Observation of the Spin-Hall Effect in a Two-Dimensional Spin-Orbit Coupled Semiconductor System. *Phys. Rev. Lett.* **94**, 047204 (4 Feb. 2005).
69. Konig, M. *et al.* Quantum spin hall insulator state in HgTe quantum wells. *Science* **318**, 766–770 (Nov. 2007).
70. Tanaka, T. *et al.* Intrinsic spin Hall effect and orbital Hall effect in 4d and 5d transition metals. *Phys. Rev. B* **77**, 165117 (16 Apr. 2008).
71. Vila, L., Kimura, T. & Otani, Y. Evolution of the Spin Hall Effect in Pt Nanowires: Size and Temperature Effects. *Phys. Rev. Lett.* **99**, 226604 (22 Nov. 2007).
72. Nakayama, H. *et al.* Geometry dependence on inverse spin Hall effect induced by spin pumping in Ni₈₁Fe₁₉/Pt films. *Phys. Rev. B* **85**, 144408 (14 Apr. 2012).

73. Rojas-Sánchez, J.-C. *et al.* Spin Pumping and Inverse Spin Hall Effect in Platinum: The Essential Role of Spin-Memory Loss at Metallic Interfaces. *Phys. Rev. Lett.* **112**, 106602 (10 Mar. 2014).
74. Kondou, K., Sukegawa, H., Mitani, S., Tsukagoshi, K. & Kasai, S. Evaluation of Spin Hall Angle and Spin Diffusion Length by Using Spin Current-Induced Ferromagnetic Resonance. *Applied Physics Express* **5**, 073002 (2012).
75. Ganguly, A. *et al.* Thickness dependence of spin torque ferromagnetic resonance in Co₇₅Fe₂₅/Pt bilayer films. *Applied Physics Letters* **104**, 072405 (Feb. 2014).
76. Althammer, M. *et al.* Quantitative study of the spin Hall magnetoresistance in ferromagnetic insulator/normal metal hybrids. *Phys. Rev. B* **87**, 224401 (22 June 2013).
77. Liu, L., Moriyama, T., Ralph, D. C. & Buhrman, R. A. Spin-Torque Ferromagnetic Resonance Induced by the Spin Hall Effect. *Phys. Rev. Lett.* **106**, 036601 (3 Jan. 2011).
78. Ganichev, S. D. *et al.* Spin-galvanic effect. *Nature* **417**, 153–156 (May 2002).
79. Manchon, A. *et al.* Analysis of oxygen induced anisotropy crossover in Pt/Co/MOx trilayers. *Journal of Applied Physics* **104**, 043914 (Aug. 2008).
80. Saitoh, E., Ueda, M., Miyajima, H. & Tatara, G. Conversion of spin current into charge current at room temperature: Inverse spin-Hall effect. *Applied Physics Letters* **88**, 182509 (2006).
81. Bauer, G. E. W., Saitoh, E. & van Wees, B. J. Spin caloritronics. *Nature Materials* **11**, 391–399 (May 2012).
82. Mizukami, S., Ando, Y. & Miyazaki, T. Ferromagnetic resonance linewidth for NM/NiFe/NM films (NM = Cu, Ta, Pd and Pt). *Journal of Magnetism and Magnetic Materials* **226**, 1640–1642 (May 2001).
83. Tserkovnyak, Y., Brataas, A. & Bauer, G. E. W. Enhanced Gilbert Damping in Thin Ferromagnetic Films. *Phys. Rev. Lett.* **88**, 117601 (11 Feb. 2002).
84. Locatelli, N., Cros, V. & Grollier, J. Spin-torque building blocks. *Nature Materials* **13**, 11–20 (Jan. 2014).
85. Chumak, A. V., Vasyuchka, V. I., Serga, A. A. & Hillebrands, B. Magnon spintronics. *Nat Phys* **11**. Review, 453–461 (June 2015).
86. Chen, T. S. *et al.* Spin-Torque and Spin-Hall Nano-Oscillators. *Proceedings of the IEEE* **104**, 1919–1945 (Oct. 2016).
87. Thomson, W. On the Electro-Dynamic Qualities of Metals:—Effects of Magnetization on the Electric Conductivity of Nickel and of Iron. *Proceedings of the Royal Society of London* **8**, 546–550 (1856).

88. McGuire, T. R. & Potter, R. I. Anisotropic Magnetoresistance in Ferromagnetic 3d Alloys. *IEEE Transactions on Magnetics* **11**, 1018–1038 (1975).
89. Gil, W., Gorlitz, D., Horisberger, M. & Kotzler, J. Magnetoresistance anisotropy of polycrystalline cobalt films: Geometrical-size and domain effects. *Physical Review B* **72**, 134401 (Oct. 2005).
90. Nakayama, H. *et al.* Spin Hall Magnetoresistance Induced by a Nonequilibrium Proximity Effect. *Physical Review Letters* **110**, 206601 (May 2013).
91. Chen, Y.-T. *et al.* Theory of spin Hall magnetoresistance. *Physical Review B* **87**, 144411 (Apr. 2013).
92. Kim, J., Sheng, P., Takahashi, S., Mitani, S. & Hayashi, M. Spin Hall Magnetoresistance in Metallic Bilayers. *Phys. Rev. Lett.* **116**, 097201 (9 Feb. 2016).
93. Seemann, K. M. *et al.* Origin of the Planar Hall Effect in Nanocrystalline Co₆₀Fe₂₀B₂₀. *Physical Review Letters* **107**, 086603 (Aug. 2011).
94. Landau & Lifschitz. *Theory of the dispersion of magnetic permeability in ferromagnetic bodies* (Phys. Z. Sowj, 1935).
95. Kim, J. *et al.* Layer thickness dependence of the current-induced effective field vector in Ta vertical bar CoFeB vertical bar MgO. *Nature Materials* **12**, 240–245 (Mar. 2013).
96. Hayashi, M., Kim, J., Yamanouchi, M. & Ohno, H. Quantitative characterization of the spin-orbit torque using harmonic Hall voltage measurements. *Physical Review B* **89**, 144425 (Apr. 2014).
97. Yang, M. *et al.* Spin-orbit torque in Pt/CoNiCo/Pt symmetric devices. *Scientific Reports* **6**, 20778 (Feb. 2016).
98. Cecot, M. *et al.* Influence of intermixing at the Ta/CoFeB interface on spin Hall angle in Ta/CoFeB/MgO heterostructures. *Scientific Reports* **7**, 968 (2017).
99. Liu, L. Q., Lee, O. J., Gudmundsen, T. J., Ralph, D. C. & Buhrman, R. A. Current-Induced Switching of Perpendicularly Magnetized Magnetic Layers Using Spin Torque from the Spin Hall Effect. *Physical Review Letters* **109**, 096602 (Aug. 2012).
100. Yang, S. H., Ryu, K. S. & Parkin, S. Domain-wall velocities of up to 750 m s⁻¹ driven by exchange-coupling torque in synthetic antiferromagnets. *Nature Nanotechnology* **10**, 221–226 (Mar. 2015).
101. Gabor, M. S. *et al.* Spin-orbit torques and magnetization switching in W/Co₂FeAl/MgO structures. *Journal of Physics D-applied Physics* **49**, 365003 (Sept. 2016).
102. Lee, J. M. *et al.* All-Electrical Measurement of Interfacial Dzyaloshinskii-Moriya Interaction Using Collective Spin-Wave Dynamics. *Nano Letters* **16**, 62–67 (Jan. 2016).

103. Woo, S., Mann, M., Tan, A. J., Caretta, L. & Beach, G. S. D. Enhanced spin-orbit torques in Pt/Co/Ta heterostructures. *Applied Physics Letters* **105**, 212404 (2014).
104. Huang, K.-F., Wang, D.-S., Lin, H.-H. & Lai, C.-H. Engineering spin-orbit torque in Co/Pt multilayers with perpendicular magnetic anisotropy. *Applied Physics Letters* **107**, 232407 (2015).
105. Yang, T. *et al.* Layer thickness dependence of spin orbit torques and fields in Pt/Co/AIO trilayer structures. *Japanese Journal of Applied Physics* **54**, 04DM05 (Apr. 2015).
106. Avci, C. O. *et al.* Fieldlike and antidamping spin-orbit torques in as-grown and annealed Ta/CoFeB/MgO layers. *Physical Review B* **89**, 214419 (June 2014).
107. An, H. *et al.* Spin-orbit torques in asymmetric Pt/Co/Pt structures. *Phys. Rev. B* **94**, 214417 (21 Dec. 2016).
108. Allen, G., Manipatruni, S., Nikonov, D. E., Doczy, M. & Young, I. A. Experimental demonstration of the coexistence of spin Hall and Rashba effects in beta-tantalum/ferromagnet bilayers. *Physical Review B* **91**, 144412 (Apr. 2015).
109. Haney, P. M., Lee, H.-W., Lee, K.-J., Manchon, A. & Stiles, M. D. Current induced torques and interfacial spin-orbit coupling: Semiclassical modeling. *Phys. Rev. B* **87**, 174411 (17 May 2013).
110. Nguyen, M.-H., Ralph, D. C. & Buhrman, R. A. Spin Torque Study of the Spin Hall Conductivity and Spin Diffusion Length in Platinum Thin Films with Varying Resistivity. *Phys. Rev. Lett.* **116**, 126601 (12 Mar. 2016).
111. Pi, U. H. *et al.* Tilting of the spin orientation induced by Rashba effect in ferromagnetic metal layer. *Applied Physics Letters* **97**, 162507 (Oct. 2010).
112. Avci, C. O. *et al.* Unidirectional spin Hall magnetoresistance in ferromagnet/normal metal bilayers. *Nature Physics* **11**, 570–575 (July 2015).
113. Málek, Z. & Kamberský, V. On the theory of the domain structure of thin films of magnetically uni-axial materials. *Czechoslovakij fiziceskij zurnal* **8**, 416–421 (1958).
114. Hubert, A. & Schäfer, R. *Magnetic Domains: The Analysis of Magnetic Microstructures*. (Berlin: Springer, 1998).
115. Bobeck, A. & Della Torre, E. *Magnetic Bubbles* (North Holland, Amsterdam, 1975).
116. Dzyaloshinskii, I. E. Theory of Helicoidal Structures in Antiferromagnets .1. Non-metals. *Soviet Physics JETP-USSR* **19**, 960–971 (1964).
117. Dzyaloshinskii, I. E. A Thermodynamic Theory of Weak Ferromagnetism of Antiferromagnetics. *Journal of Physics and Chemistry of Solids* **4**, 241–255 (1958).

118. Moriya, T. Anisotropic Superexchange Interaction and Weak Ferromagnetism. *Phys. Rev.* **120**, 91–98 (1 Oct. 1960).
119. Moriya, T. Theory of Magnetism of NiF₂. *Phys. Rev.* **117**, 635–647 (3 Feb. 1960).
120. Kikuchi, T., Koretsune, T., Arita, R. & Tatara, G. Dzyaloshinskii-Moriya Interaction as a Consequence of a Doppler Shift due to Spin-Orbit-Induced Intrinsic Spin Current. *Physical Review Letters* **116**, 247201 (June 2016).
121. Pizzini, S. *et al.* Chirality-Induced Asymmetric Magnetic Nucleation in Pt/Co/AlO_x Ultrathin Microstructures. *Physical Review Letters* **113**, 047203 (July 2014).
122. Safeer, C. K. *et al.* Spin-orbit torque magnetization switching controlled by geometry. *Nature Nanotechnology* **11**, 143–146 (Feb. 2016).
123. Schwefflinghaus, B., Zimmermann, B., Heide, M., Bihlmayer, G. & Blügel, S. Role of Dzyaloshinskii-Moriya interaction for magnetism in transition-metal chains at Pt step edges. *Phys. Rev. B* **94**, 024403 (2 July 2016).
124. Han, D. S. *et al.* Asymmetric Hysteresis for Probing Dzyaloshinskii-Moriya Interaction. *Nano Letters* **16**, 4438–4446 (July 2016).
125. Belmeguenai, M. *et al.* Interfacial Dzyaloshinskii-Moriya interaction in perpendicularly magnetized Pt/Co/AlO_x ultrathin films measured by Brillouin light spectroscopy. *Physical Review B* **91**, 180405 (May 2015).
126. Cho, J. *et al.* Thickness dependence of the interfacial Dzyaloshinskii-Moriya interaction in inversion symmetry broken systems. *Nature Communications* **6**, 7635 (July 2015).
127. Leonov, A. O. *et al.* The properties of isolated chiral skyrmions in thin magnetic films. *New Journal of Physics* **18**, 065003 (May 2016).
128. Moreau-Luchaire, C. *et al.* Additive interfacial chiral interaction in multilayers for stabilization of small individual skyrmions at room temperature. *Nature Nanotechnology* **11**, 444 (May 2016).
129. Romming, N., Kubetzka, A., Hanneken, C., von Bergmann, K. & Wiesendanger, R. Field-Dependent Size and Shape of Single Magnetic Skyrmions. *Phys. Rev. Lett.* **114**, 177203 (17 May 2015).
130. Röbller, U. K., Bogdanov, A. N. & Pfleiderer, C. Spontaneous skyrmion ground states in magnetic metals. *Nature* **442**, 797–801 (Aug. 2006).
131. Bobeck, A. H., Bonyhard, P. I. & Geusic, J. E. Magnetic bubbles: An emerging new memory technology. *Proceedings of the IEEE* **63**, 1176–1195 (Aug. 1975).

132. Iunin, Y. L. *et al.* Magnetic field dependence of asymmetry in the magnetization reversal of ultrathin Co films and Co/Pt multilayers with perpendicular anisotropy. *Journal of Magnetism and Magnetic Materials* **320**, 2044–2048 (Aug. 2008).
133. Heinze, S. *et al.* Spontaneous atomic-scale magnetic skyrmion lattice in two dimensions. *Nature Physics* **7**, 713–718 (Sept. 2011).
134. Je, S.-G. *et al.* Asymmetric magnetic domain-wall motion by the Dzyaloshinskii-Moriya interaction. *Physical Review B* **88**, 214401 (Dec. 2013).
135. Hrabec, A. *et al.* Measuring and tailoring the Dzyaloshinskii-Moriya interaction in perpendicularly magnetized thin films. *Physical Review B* **90**, 020402 (July 2014).
136. Lavrijsen, R. *et al.* Asymmetric magnetic bubble expansion under in-plane field in Pt/Co/Pt: Effect of interface engineering. *Physical Review B* **91**, 104414 (Mar. 2015).
137. Di, K. *et al.* Direct Observation of the Dzyaloshinskii-Moriya Interaction in a Pt/Co/Ni Film. *Physical Review Letters* **114**, 047201 (Jan. 2015).
138. Kim, N. H. *et al.* Improvement of the interfacial Dzyaloshinskii-Moriya interaction by introducing a Ta buffer layer. *Applied Physics Letters* **107**, 142408 (Oct. 2015).
139. Vanatka, M. *et al.* Velocity asymmetry of Dzyaloshinskii domain walls in the creep and flow regimes. *Journal of Physics-condensed Matter* **27**, 326002 (Aug. 2015).
140. Di, K. *et al.* Asymmetric spin-wave dispersion due to Dzyaloshinskii-Moriya interaction in an ultrathin Pt/CoFeB film. *Applied Physics Letters* **106**, 052403 (Feb. 2015).
141. Soucaille, R. *et al.* Probing the Dzyaloshinskii-Moriya interaction in CoFeB ultrathin films using domain wall creep and Brillouin light spectroscopy. *Phys. Rev. B* **94**, 104431 (10 Sept. 2016).
142. Koerner, H. S. *et al.* Interfacial Dzyaloshinskii-Moriya interaction studied by time-resolved scanning Kerr microscopy. *Physical Review B* **92**, 220413 (Dec. 2015).
143. Tacchi, S. *et al.* Interfacial Dzyaloshinskii-Moriya Interaction in Pt/CoFeB Films: Effect of the Heavy-Metal Thickness. *Phys. Rev. Lett.* **118**, 147201 (14 Apr. 2017).
144. Wells, A. W. J., Shepley, P. M., Marrows, C. H. & Moore, T. A. Effect of interfacial intermixing on the Dzyaloshinskii-Moriya interaction in Pt/Co/Pt. *Phys. Rev. B* **95**, 054428 (5 Feb. 2017).
145. Wang, J., Sannomiya, T., Shi, J. & Nakamura, Y. Interface roughness induced asymmetric magnetic property in sputter-deposited Co/CoO/Co exchange coupled trilayers. *Journal of Applied Physics* **111**, 07D725 (Apr. 2012).
146. Belabbes, A., Bihlmayer, G., Bluegel, S. & Manchon, A. Oxygen-enabled control of Dzyaloshinskii-Moriya Interaction in ultra-thin magnetic films. *Scientific Reports* **6**, 24634 (Apr. 2016).

147. Gross, I. *et al.* Direct measurement of interfacial Dzyaloshinskii-Moriya interaction in $X|\text{CoFeB}|\text{MgO}$ heterostructures with a scanning NV magnetometer ($X = \text{Ta}, \text{TaN},$ and W). *Phys. Rev. B* **94**, 064413 (6 Aug. 2016).
148. Lo Conte, R. *et al.* Role of B diffusion in the interfacial Dzyaloshinskii-Moriya interaction in $\text{Ta}/\text{Co}_{20}\text{Fe}_{60}\text{B}_{20}/\text{MgO}$ nanowires. *Physical Review B* **91**, 014433 (Jan. 2015).
149. Yang, H., Thiaville, A., Rohart, S., Fert, A. & Chshiev, M. Anatomy of Dzyaloshinskii-Moriya Interaction at Co/Pt Interfaces. *Physical Review Letters* **115**, 267210 (Dec. 2015).
150. Kundu, A. & Zhang, S. Dzyaloshinskii-Moriya interaction mediated by spin-polarized band with Rashba spin-orbit coupling. *Phys. Rev. B* **92**, 094434 (9 Sept. 2015).
151. Cortes-Ortuno, D. & Landeros, P. Influence of the Dzyaloshinskii-Moriya interaction on the spin-wave spectra of thin films. *Journal of Physics-condensed Matter* **25**, 156001 (Apr. 2013).
152. Nembach, H. T., Shaw, J. M., Weiler, M., Jue, E. & Silva, T. J. Linear relation between Heisenberg exchange and interfacial Dzyaloshinskii-Moriya interaction in metal films. *Nature Physics* **11**, 825 (Oct. 2015).
153. Hrabec, A. *et al.* Making the Dzyaloshinskii-Moriya interaction visible. *Applied Physics Letters* **110**, 242402 (2017).
154. Jue, E. *et al.* Chiral damping of magnetic domain walls. *Nature Materials* **15**, 272 (Mar. 2016).
155. Boulle, O. *et al.* Domain Wall Tilting in the Presence of the Dzyaloshinskii-Moriya Interaction in Out-of-Plane Magnetized Magnetic Nanotracks. *Physical Review Letters* **111**, 217203 (Nov. 2013).
156. Levy, P. M. & Fert, A. Anisotropy Induced by Nonmagnetic Impurities in Cumm Spin-glass Alloys. *Physical Review B* **23**, 4667–4690 (1981).
157. Kotzler, J., Gornitz, D., Kurfiss, M., von Sawilski, L. & Vedmedenko, E. Y. Vortex fluctuations and freezing of dipolar-coupled granular moments in thin ferromagnetic films. *Physical Review B* **73**, 224425 (June 2006).
158. Ellsworth, D. *et al.* Photo-spin-voltaic effect. *Nature Physics* **12**, 861–866 (2016).
159. Kopte, M. *et al.* The complete micromagnetic characterization of asymmetrically sandwiched ferromagnetic films. *arXiv:1706.09322v1* (June 2017).
160. Langer, M. *et al.* Parameter-free determination of the exchange constant in thin films using magnonic patterning. *Applied Physics Letters* **108**, 102402 (Mar. 2016).

161. Nozaki, T., Oida, M., Ashida, T., Shimomura, N. & Sahashi, M. Temperature-dependent perpendicular magnetic anisotropy of Co-Pt on Cr₂O₃ antiferromagnetic oxide. *Applied Physics Letters* **103**, 242418 (Dec. 2013).
162. Kittel, C. *Introduction to Solid State Physics* 8th ed. (Wiley, 2004).
163. Iunin, Y. L. *et al.* Asymmetric domain nucleation and unusual magnetization reversal in ultrathin Co films with perpendicular anisotropy. *Physical Review Letters* **98**, 117204 (Mar. 2007).
164. Metaxas, P. J. *et al.* Creep and flow regimes of magnetic domain-wall motion in ultrathin Pt/Co/Pt films with perpendicular anisotropy. *Physical Review Letters* **99**, 217208 (Nov. 2007).
165. Gorchon, J. *et al.* Pinning-Dependent Field-Driven Domain Wall Dynamics and Thermal Scaling in an Ultrathin Pt/Co/Pt Magnetic Film. *Physical Review Letters* **113**, 027205 (July 2014).
166. Lemerle, S. *et al.* Domain Wall Creep in an Ising Ultrathin Magnetic Film. *Phys. Rev. Lett.* **80**, 849–852 (4 Jan. 1998).
167. Kabanov, Y. P. *et al.* In-Plane Field Effects on the Dynamics of Domain Walls in Ultrathin Co Films With Perpendicular Anisotropy. *Ieee Transactions on Magnetics* **46**, 2220–2223 (June 2010).
168. Kim, D.-Y., Kim, D.-H., Moon, J. & Choe, S.-B. Determination of magnetic domain-wall types using Dzyaloshinskii-Moriya-interaction-induced domain patterns. *Applied Physics Letters* **106**, 262403 (June 2015).
169. Kosub, T., Kopte, M., Radu, F., Schmidt, O. G. & Makarov, D. All-Electric Access to the Magnetic-Field-Invariant Magnetization of Antiferromagnets. *Physical Review Letters* **115**, 097201 (Aug. 2015).
170. Kopte, M., Kosub, T., Heinze, L., Faßbender, J. & Makarov, D. Straight-forward simultaneous quantification of magnetoresistance effects and spin-orbit torques in CrO_x/Co/Pt trilayers. (in preparation) (2017).
171. Gottlieb, D & Halpern, V. The electrical conductivity of very thin metal films. *Journal of Physics F: Metal Physics* **6**, 2333 (1976).
172. Slepicka, P., Svorcik, V., Slouf, M., Rybka, V. & Spirkova, M. Characterization of metal nanolayers sputtered on poly(ethyleneterephthalate). *Optoelectronics and Advanced Materials-rapid Communications* **2**, 153–160 (Mar. 2008).
173. Timalsina, Y. P. *et al.* Effects of nanoscale surface roughness on the resistivity of ultrathin epitaxial copper films. *Nanotechnology* **26**, 075704 (2015).

174. Akyol, M. *et al.* Effect of heavy metal layer thickness on spin-orbit torque and current-induced switching in Hf[CoFeB|MgO] structures. *Applied Physics Letters* **109**, 022403 (2016).
175. Melo, L. L., Vaz, A. R., Salvadori, M. C. & Cattani, M. Grain sizes and surface roughness in platinum and gold thin films. *Ismanam 2003: Metastable, Mechanically Alloyed and Nanocrystalline Materials* **20-21**, 623–628 (2004).
176. Wilhelm, F. *et al.* Layer-Resolved Magnetic Moments in Ni/Pt Multilayers. *Phys. Rev. Lett.* **85**, 413–416 (2 July 2000).
177. Meier, F. *et al.* Spin polarization of platinum (111) induced by the proximity to cobalt nanostripes. *Phys. Rev. B* **83**, 075407 (7 Feb. 2011).
178. Huang, S. Y. *et al.* Transport Magnetic Proximity Effects in Platinum. *Phys. Rev. Lett.* **109**, 107204 (10 Sept. 2012).
179. Skinner, T. D. *et al.* Spin-orbit torque opposing the Oersted torque in ultrathin Co/Pt bilayers. *Applied Physics Letters* **104**, 062401 (2014).
180. Fowley, C *et al.* Local modification of magnetic anisotropy and ion milling of Co/Pt multilayers using a He⁺ ion beam microscope. *Journal of Physics D: Applied Physics* **46**, 195501 (2013).
181. Van den Brink, A. *et al.* Field-free magnetization reversal by spin-Hall effect and exchange bias. *Nature Communications* **7**, 10854 (Mar. 2016).
182. Kosub, T. *et al.* Purely antiferromagnetic magnetoelectric random access memory. *Nature Communications* **8**, 13985 (Jan. 2017).
183. Franken, J. H., Hoeijmakers, M., Swagten, H. J. M. & Koopmans, B. Tunable Resistivity of Individual Magnetic Domain Walls. *Physical Review Letters* **108**, 037205 (Jan. 2012).
184. Ganzhorn, K. *et al.* Spin Hall magnetoresistance in a canted ferrimagnet. *Phys. Rev. B* **94**, 094401 (9 Sept. 2016).
185. Meyer, S. *et al.* Anomalous Hall effect in YIG|Pt bilayers. *Applied Physics Letters* **106**, 132402 (2015).
186. Rohart, S. & Thiaville, A. Skyrmion confinement in ultrathin film nanostructures in the presence of Dzyaloshinskii-Moriya interaction. *Physical Review B* **88**, 184422 (Nov. 2013).

Acknowledgements

I gratefully thank Dr. T. Kosub not only for the development of the magnetotransport measurement setup, countless fruitful discussions, useful hints, his support in performing experiments or writing mathematica scripts, but also for a great companionship during the whole time of my PhD, Dr. U. K. R. Röbner for sharing his theoretical background with me and his great help proofreading the manuscript, Prof. Dr. R. Schäfer, Dr. I. Soldatov and S. Pofahl for the provision of Kerr microscopy equipment and the experienced advise for its operation, C. Krien, R. Kaltofen for many sputter deposited samples, D. Stein and L. Heinze for Kerr microscopy and magnetotransport measurements respectively during their internships, H. Fuchs for his support in writing python scripts, Dr. S. Facsko for the Auger electron spectroscopy measurements, G. Rane, A. Scholz and Dr. J. Grenzer for X-ray reflectometry measurements, C. Xu for SQUID measurements, K. Wagner, T. Hula, Dr. T. Sebastian and Dr. H. Schultheiß for trying to measure asymmetric magnon dispersion with their BLS, Dr. S. Stienen, Dr. A. Semisalova, Dr. J. Lindner and Dr. K. Lenz for ferromagnetic resonance measurements and analysis, the clean room stuff of the IFW Dresden and HDZR for their assistance with sample processing and the maintenance of the equipment, including Dr. S. Harazim, B. Eichler, S. Nestler, M. Bauer and T. Schönherr, Dr. J. Geogiev, C. Neisser, B. Schnabel respectively, Dr. I. Mönch for useful advice for thin film microstructuring, Dr. C. Fowley for his support with Ion beam etching, Dr. A. Kákay, Dr. J. Otalora, Dr. O. Volkov and T. Schneider for their help with micromagnetic simulations, Dr. E. Y. Vedmedenko for contributing with the modified Levy-Fert three site model, Dr. D. Makarov, Prof. Dr. O. G. Schmidt, Dr. J. Lindner and Prof. Dr. J. Faßbender for the opportunity to use the scientific infrastructure and their supervision and my wife and family for their moral support.